Bio-inspired white porous polymers fabricated via supercritical CO_2 foaming

Zur Erlangung des akademischen Grades einer

Doktorin der Ingenieurwissenschaften (Dr.-Ing.)

von der KIT-Fakultät für Maschinenbau des
Karlsruher Instituts für Technologie (KIT)

genehmigte

Dissertation

von

M. Sc. Luisa Maren Borgmann

Zusammenfassung

Das heutzutage kommerziell bedeutsamste Weißpigment Titandioxid (TiO_2) wird für eine Vielzahl von industriellen Produkten genutzt, insbesondere in Farben, Beschichtungen und Kunststoffen. Aufgrund seiner energieintensiven Gewinnung, der kostspieligen Entsorgung schädlicher Nebenprodukte und zunehmender Zweifel an seiner gesundheitlichen Unbedenklichkeit steht dieses Pigment jedoch seit Jahren in der Kritik, weshalb nach alternativen Lösungen gesucht wird. Inspirationsquellen für neue, umweltfreundliche Strategien einen weißen Farbeindruck ohne TiO_2 zu erzeugen, lassen sich in der Natur finden. Hier entsteht Weiß oft durch luftgefüllte, poröse Strukturen, an denen Licht aller Wellenlängen sehr effektiv gestreut wird. Die dabei genutzten Biomaterialien Chitin, Keratin oder Cellulose haben einen höheren Brechungsindex als Luft, wodurch der für die Lichtstreuung notwendige Kontrast im Brechungsindex erreicht wird.

Dieses Prinzip lässt sich technisch durch die Erzeugung von lichtstreuenden Nanoporen in einer transparenten Polymermatrix umsetzen. In der vorliegenden Arbeit wird dazu physikalisches Schäumen mit überkritischem Kohlenstoffdioxid angewandt. Im überkritischen Zustand hat Kohlenstoffdioxid bemerkenswert gute Diffusionseigenschaften und wirkt als inerter, ungiftiger Weichmacher für viele Polymere. Zusätzlicher Vorteil gegenüber chemischen Treibmitteln ist, dass keine schädlichen Rückstände im Material zurückgelassen werden. Über die Prozessparameter können die Charakteristika der Poren beeinflusst werden, um diese für den Einsatz als alternative Weißpigmente zu optimieren.

In dieser Arbeit wird zunächst das Schäumen von monodispersen Polymethylmethacrylat (PMMA) Mikrokugeln untersucht. Im Gegensatz zu bisherigen Arbeiten zu geschäumten, rotationsbeschichteten Oberflächen ist die Pulverform einfacher in bestehende Prozessketten zu implementieren. Es werden geeignete Prozessparameter identifizert und ein Prototyp einer weißen Farbe auf Basis geschäumter, weißer Polymerpartikel präsentiert. Des Weiteren werden Prozessmodifikationen entwickelt, die das Schäumen deutlich kleinerer Mikrokugel erlauben und damit den möglichen Anwendungsbereich erweitern.

Zusätzlich zu ästhetischen Gründen kann eine weiße Farbgebung auch funktionale Vorteile haben. Eine helle Oberfläche kann bei Gebäuden oder Autos für

eine geringere Aufheizung unter Sonneneinstrahlung sorgen, da ein Großteil der einfallenden Strahlung reflektiert und somit nicht in Wärme umgewandelt wird. In Anbetracht des zukünftig stark ansteigenden Bedarfs an Klimaanlagen und deren Stromverbrauchs rücken zunehmend auch passive Strategien zur Kühlung in den Fokus. Vielversprechend ist hierbei die passive Strahlungskühlung. Bei dieser Strategie wird die Transparenz der Erdatmosphäre für bestimmte Wellenlängen genutzt, um Wärmestrahlung in den Weltraum abzugeben. Dafür eignen sich bestimmte Materialien, die in diesem Teil des Spektrums gut absorbieren und daher in diesem Spektralbereich ebenfalls Strahlung emittieren. Kombiniert man diese Materialien nun mit einer weißen Farbgebung, die zusätzliches Aufheizen minimiert, kann auch tagsüber eine Kühlung unterhalb der Umgebungstemperatur erreicht werden. Daher wird in dieser Arbeit die mögliche Eignung weiß geschäumter Polymere für die passive Strahlungskühlung untersucht.

Weiße Oberflächen insbesondere im Außenbereich können von schmutzabweisenden, selbstreinigenden Oberflächeneigenschaften stark profitieren. Hierbei kann beispielsweise eine superhydrophobe Oberflächenstruktur Verschmutzungen limitieren. Solche Oberflächen sind in der Natur weit verbreitet und bieten Konzepte für die Strukturierung technischer Oberflächen. Während der Behandlung mit überkritischem Kohlenstoffdioxid ist das Polymer verformbar, was für die Übertragung von Strukturen genutzt werden kann. In dieser Arbeit wird eine Kombination des Schäumprozesses mit simultaner Replikation von bio-inspirierten Strukturen untersucht. Die dazu entwickelte Prozessvariation ermöglicht eine gleichzeitige Oberflächenstrukturierung zusätzlich zu dem weißen Farbeindruck, der durch die lichtstreuenden Poren entsteht.

Abstract

Today's most commercially significant white pigment, titanium dioxide (TiO_2), is used in a wide range of industrial products, especially paints, coatings and plastics. However, due to its energy-intensive extraction, the harmful by-products produced, their costly disposal and increasing doubts about its innocuousness to health, this pigment has been subject of criticism for years. Sources of inspiration for new, environmentally friendly strategies to create a white color impression without titanium dioxide can be found in nature. Here, white is often created by air-filled, porous structures on which light of all wavelengths is effectively scattered. The biomaterials used thereby, such as chitin, keratin or cellulose, have a higher refractive index than air, thus achieving the contrast in refractive index necessary for light scattering.

This principle can be technically implemented by creating light-scattering nanopores in a transparent polymer matrix. In this work, physical foaming with supercritical carbon dioxide is used for this purpose. In its supercritical state, carbon dioxide has remarkably good diffusion properties and acts as an inert, non-toxic plasticizer for many polymers. Additional advantage over chemical blowing agents is that no harmful residues are left in the material. The characteristics of the pores can be influenced via the process parameters in order to optimize them for use as alternative white pigments.

In this work at first the foaming of monodisperse polymethyl methacrylate (PMMA) microspheres was established. In contrast to previous work on foamed spincoated surfaces the powder form is easier to implement in existing process chains. Suitable process parameters are identified and a prototype of a white paint based on foamed white polymer particles is presented. Furthermore, process modifications are developed that allow the foaming of significantly smaller microspheres and thus extend the possible range of applications.

In addition to aesthetic reasons, a white color can also have functional benefits. A light-colored surface can reduce the heat buildup in buildings or cars when exposed to sunlight, since a large proportion of the incident radiation is reflected back and thus not converted into heat. In view of the strong increase in demand for air conditioning systems and their power consumption in the future,

passive strategies for cooling are increasingly coming into focus. Passive radiative cooling is a promising approach in this context. Here, one takes advantage of the transparency of the Earth's atmosphere for certain wavelengths to emit thermal radiation into space. Certain materials that absorb well in this part of the spectrum and therefore also emit radiation in this spectral range are suitable for this purpose. If these materials are additionally white in color to minimize additional heat uptake, cooling below ambient temperature can be achieved even during the day. Therefore, in this work the potential suitability of white foamed polymers for passive radiative cooling is investigated.

White surfaces, especially outdoors, can benefit greatly from dirt-repellent, self-cleaning surface properties. Here, for example, a superhydrophobic surface structure can limit soiling. Such surface structures are widespread in nature and provide concepts for the structuring of technical surfaces. During foaming with supercritical carbon dioxide, the polymer is deformable, which can be exploited for molding. In this work, a combination of the foaming process with simultaneous replication of bio-inspired structures is investigated. The process variation developed for this purpose allows simultaneous surface texturing in addition to the white color impression created by the light-scattering pores.

Contents

List of Figures

List of Tables

Abbreviations

AFM	Atomic force microscopy
ANSES	Agence nationale de sécurité sanitaire de l'alimentation, de l'environnement et du travail - French Agency for Food, Environmental and Occupational Health and Safety
CAB	Cellulose acetate butyrate
$CaCO_3$	calcium carbonate
CFCs	Chlorofluorocarbons
CO_2	Carbon dioxide
CPL	Classification, Labelling and Packaging Regulation
ECHA	European Chemicals Agency
EFSA	The European Food Safety Authority
FTIR	Fourier-transform infrared spectroscopy
GHS	Globally Harmonized System of Classification and Labelling of Chemicals
H_2SO_4	Sulfuric acid
HCFCs	Hydrochlorofluorocarbons
HCl	Hydrochloric acid
HFCs	Hydrofluorocarbons
HfO_2	Hafnium dioxide
HRES	high-resolution
IARC	International Agency for Research on Cancer
IEA	International Energy Agency
INRAE	Institut national de recherche pour l'agriculture, l'alimentation et l'environnement - National Research Institute for Agriculture, Food and the Environment
LFOV	large field-of-view
MgF_2	Magnesium fluoride
MSB	Magnetic suspension balance
NH_4Cl	Ammonium chloride
NIR	Near-infra-red
P(VdF-HFP)	Poly(vinylidene fluoride-co-hexafluoropropene)
PBS	Polybutylene succinate

PCL	Polycaprolactone
PDMS	Polydimethylsiloxane
PE	Polyethylen
PEG	Polyethylene glycol
PEO	Polyethylene oxide
PHB	Polyhydroxy butyrate
PMMA	Polymethyl methacrylat
PTFE	Polytetrafluoroethylene
PVA	Polyvinyl alcohol
PVDF	Polyvinylidene difluoride
PVP	Polyvinylpyrrolidone
RAC	The Committee for Risk Assessment
SEM	Scanning electron microscope
SiC	Silicon carbide
SiO_2	Silicon dioxide
SO_3	Sulfur trioxide
$TiCl_4$	Titanium-tetrachloride
TiO_2	Titanium dioxide
$TiO(OH)_2$	Metatitanic acid
$TiOSO_4$	Titanyl sulfate
UV	Ultraviolet
Vis	Visible
ZnO	Zinc oxide

Chapter 1

Introduction

For a variety of consumer products a bright white surface is desired, which is typically achieved by adding white pigments. These provide a high refractive index compared to the surrounding transparent material, e.g. a paint formulation or a polymer matrix. A white color impression occurs if all wavelengths of visible light are scattered equally, whereby the intensity depends on the differences in refractive index, the particle size and on the wavelength of light being scattered [1, 2]. For conventional white pigments -such as titanium dioxide (TiO_2)- the scattering is most effective for particle sizes in the nanometer range, which is crucial when considering health aspects [3]. The safety assessment of these pigments is under continuous controversial debate and investigation [4, 5, 6, 7, 8, 9] and recently the first bans in the food sector have been initiated [10, 11]. In addition, the energy intensive production from the ore to the final pigment, the disposal of harmful by-products and the lack of recycling of this limited resource have to be considered [12, 13]. Due to these problems, further regulatory restrictions are expected in the future, and alternatives to conventional TiO_2 pigments will be needed.

Solutions can be found in living nature, where a bright white color impression is created without inorganic pigments. In nature, white often originates from sophisticated nanostructures in conjunction with the surrounding air, a strategy that ensures the refractive index contrast required for efficient scattering. Various species of plants, insects, and birds thereby utilize cellulose [14], chitin [15], or keratin [16], respectively. Thereby, opacity is achieved in a very material efficient way, based on only one matrix material and air. A selection of species and their respective strategies for efficient scattering are discussed in Chapter 2.

An implementation of this strategy, using air as a low refractive index component and the material forming the structure as a high refractive index material, can be achieved by introducing nanopores into a polymeric material. The environmentally friendly physical foaming technique based on supercritical carbon

Chapter 4: Porous polymeric microparticles as scattering white pigments
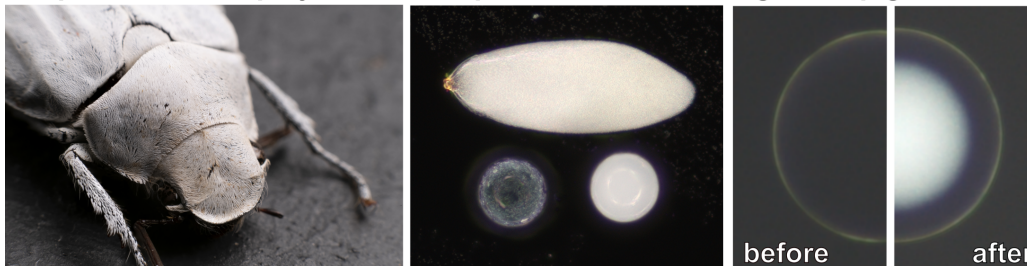
Chapter 5: Porous Polymers for passive radiative daytime cooling
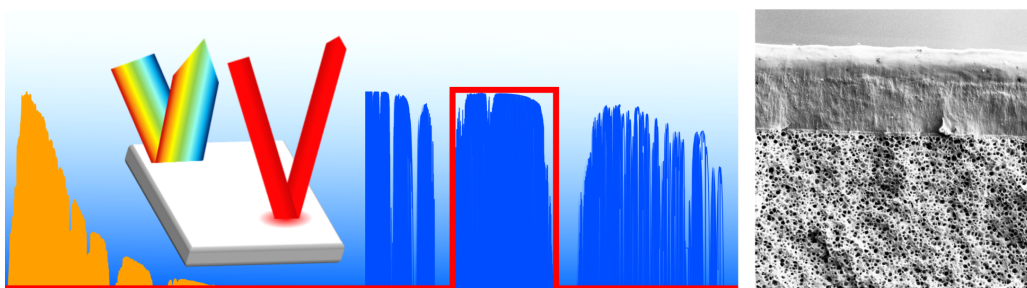
Chapter 6: Combined foaming and surface structuring with supercritical CO₂
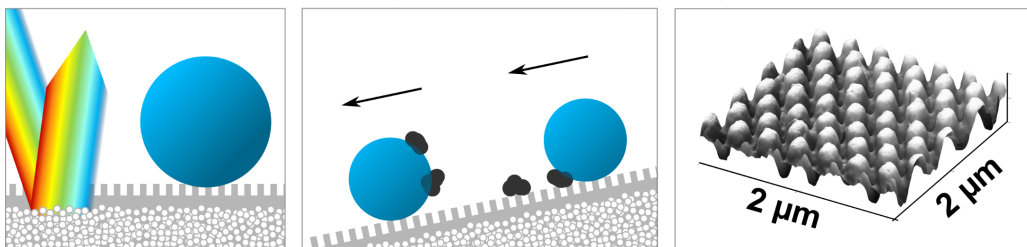
Figure 1.1: Schematic outline of this thesis.

dioxide (CO_2) has been shown to be a suitable fabrication method to mimic the bio-inspired strategies by creating nano-sized air inclusions [17]. In Chapter 3, supercritical CO_2 foaming, which has been utilized and adapted for various applications in this study, is presented in detail.

In Chapter 4 the previously mentioned disadvantages associated with the predominantly used white pigment TiO_2 are discussed in further detail and porous polymeric pigments are presented as an alternative approach to achieve a white coloration. Thus, the objective here is to investigate the transferability, limitations and optimal parameters of the supercritical foaming process for successful foaming of microparticles and, if necessary, explore modifications of the process. Subsequent objective is the evaluation of their suitability for use as alternative white pigments.

In addition to the interest in white surfaces for aesthetic reasons, they can

also have valuable functional benefits. A simple everyday example is the comparison of the temperatures of white surfaces with dark ones, when exposed to blazing sunlight. While the bright surface reflects a large proportion of the incoming radiation, the dark surface absorbs a large proportion and heats up thereby. For objects in prevailing hot climatic conditions, where heat up is generally rather undesirable, choosing the right surface coloration, e.g., for vehicles [18] or buildings [19], therefore is a step towards saving energy costs on air conditioning. The consideration of reflection, transmission and absorption properties needs not be restricted to the visible parts of the light. Surfaces with additionally well tuned optical properties in the infrared part of the spectrum can achieve cooling even beneath ambient temperature, a passive mechanism referred to as radiative cooling. This strategy takes advantage of the partial transmittance of the Earth's atmosphere for certain wavelengths to emit excess thermal radiation back into space. The search for materials with suitable optical properties, their optimization and efficient use currently is a rapidly emerging field of research. Hereby porous polymers have been found to be a well-suited material category [20, 21, 22, 23, 24, 25], with advantages such as their low-cost and the option for large-scale production standing out in particular [26]. The objectives of Chapter 5 thus are the assessment of suitable materials for both, passive radiative daytime cooling and supercritical CO_2 foaming, the production of porous polymers foils and the evaluation of their optical properties for the applicability in passive radiative daytime cooling.

White porous polymers could greatly benefit from dirt-repellent or self- cleaning surface properties, especially when used in outdoor applications either for aesthetic or functional reasons, as e.g. for passive radiative daytime cooling. A superhydrophobic, self-cleaning surface structure could prevent and limit contamination and thus ensure functionality with less maintenance. Such superhydrophobic surface structures are common in nature and offer a great inspiration for the functional structuring of surfaces. In Chapter 6 suitable functional surface structures in nature are discussed and a strategy is targeted to utilize supercritical CO_2 foaming to imprint bio-inspired structures and simultaneously generate a white color impression in one step. Subsequent objective is the evaluation of the patterning in the micro and nano-size range, the resulting changes in surface characteristics and the foaming with accompanying influence on the optical properties.

Finally, a brief summary of the findings and possible directions for further research are discussed in Chapter 7.

Chapter 2

Theoretical Background

For a better understanding of Chapters 4 to 6, some important basics on optics and the analytical methods used are outlined in the following. Out of the large selection of standard works about the basic principles of optics, the textbooks [2, 27, 28, 29] were used for this review. First, basic interactions of light at interfaces are described, as under certain conditions, light can be reflected over a wide wavelength range by combining several interfaces. Since these are difficult to manufacture and result in a silvery, instead of a white color, in the following the scattering of light at scattering centers is focused on. Distinctions of different scattering types are described according to the size of the scattering center. Mie scattering, which is particularly important for this work, is discussed in more detail. Scattering of light is also a common strategy in nature to achieve a white color impression in a material efficient way. Therefore different species and their respective approach for a white coloration are summarized. Subsequently, the main optical and surface analytical methods used in this work are described.

2.1   Light interactions at interfaces

When light passes from one transparent medium to another and both differ in their refractive index n, interactions such as reflection, transmission and refraction occur at the interface. The intensity of the reflected and the transmitted light can be calculated with the Fresnel equations for any angle of incidence. For the simplest case with normal incidence on the interface $\theta_1 = 0$, the reflectance can be simply calculated from the refractive indices by $R = \left(\frac{n_1-n_2}{n_1+n_2}\right)^2$. When the angle of incidence θ_1 and the refractive indices n_1 and n_2 are known, the angle of refraction θ_2 can be calculated from the Snell's law $n_1 \sin\theta_1 = n_2 \sin\theta_2$, as depicted in Figure 2.1 a). The refractive index of materials varies with the wavelength, which is called dispersion of the medium. Thus the refraction of light

is wavelength-dependent, too. Typically the refractive index decreases with increasing wavelength, thus long-wave red light is deflected less than short-wave blue light.
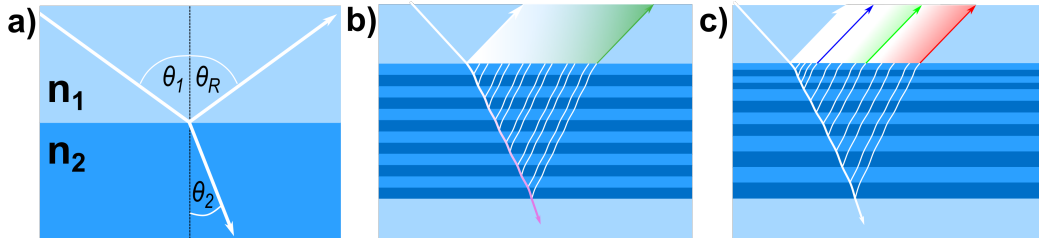
Figure 2.1: a) Light travels through a medium with the refractive index n_1 with the angle of incidence θ_1. At the interface to a medium with the refractive index n_2 reflection and refraction of light occurs with the angle θ_R and θ_2, respectively. Multilayer systems with multiple interfaces possessing constructive interference optimized for b) high reflection of a specific wavelength and c) for a broadband reflection. In b), the respective layer thickness remains uniform and is tailored to constructive interference of the desired color. In c), the layer thicknesses vary to allow constructive interference for a variety of colors, which add up to a broadband reflection.

When considering the interaction of light with more than one interface, enhancement or attenuation of light can occur due to interference effects. Prerequisite are multiple interfaces arranged approximately parallel with distances short compared to the wavelength of light. The resulting interference effects are due to the superposition of the proportions of light reflected at each of the different interfaces involved. The superposition of these waves can cause a complete cancellation (destructive interference) of both waves, a complete addition of their amplitudes (constructive interference) or any intermediate of these both extremes. Which case occurs and for which wavelength of light depends on the angle of incidence, the respective refractive index and the layer thickness.

Destructive interference of a thinfilm of low refractive index and well tuned thickness on top of a high refractive index material is widely used for antireflective coatings [30]. An alternative approach for antireflective coatings based on nano-structured surfaces will be introduced in Chapter 6. The alternate stacking of multiple high and a low refractive index materials $n_1 < n_2 < n_3$ is shown in Figure 2.1 b), an assembly also referred to as 1D-photonic crystal, Bragg reflector or dielectric mirror [31]. The constructive interference of light strongly enhances the reflection for the wavelength the system is tuned to, a phenomena also broadly used in nature to create vibrant colors, prominent examples of

which are *Morpho* butterflies or the elytra of Japanese jewel beetles [30].

For a broadband reflection approximately equal intensity of the reflected light over the entire spectrum is required. This can be accomplished by combining a multitude of layers of different thicknesses [32]. Thereby each layer will promote the constructive interference of a specific wavelength, as depicted in Figure 2.1 c). The varicolored reflections add up and create a broadband reflection over all wavelengths. A similar approach is technically implemented in so-called chirped mirrors and can also be found in nature for example in the silvery beetle *Plusiotis optima* [32, 33]. So for applications aiming at high reflection of a broad wavelength range, the use of alternating layers differing in refractive index and thickness might be a possible approach, which was also proposed as strategy for passive radiative cooling devices, further described in Chapter 5. The main disadvantage, however, is that the interference in thinfilms and multilayer systems depends strongly on the angle of incidence θ_1. Thus, chirped multilayers tuned for broadband reflection in the visible wavelength range are silvery in appearance. Furthermore the production of these multilayer systems needs sophisticated fabrication methods. High broadband reflection however can also be achieved by the uniform scattering of all wavelengths corresponding to a white colour impression.

2.2   Scattering of light

Scattering of light refers to the deflection of a portion of light from its original direction as it passes through matter due to interaction with a scattering center. In general, one can distinguish between elastic and inelastic scattering phenomena. For elastic scattering, the sum of the kinetic energies after the interaction is the same as before and the scattered light has the same frequency as the incident light. In inelastic scattering, part of the energy is converted, for example, into excitation energy. In the following only elastic scattering phenomena will be considered. When distinguishing scattering phenomena, the size of the scattering center in relation to the wavelength of the incident light is important.

Rayleigh scattering [34] applies to particles, which are small (about $< \frac{1}{10}\lambda$) compared to the wavelength of light. As the intensity of scattered light is proportional to $\frac{1}{\lambda^4}$, Rayleigh scattering is highly wavelength dependent. At the atmospheric molecules for example, especially the blue, short-wavelength part of the sunlight is scattered, which creates the blue appearance of the sky. Mie scattering [1] applies for particles with roughly the same size range as the wavelength. When the particle size exceeds λ the scattering becomes independent on wavelength, this is why clouds, mist or fog formed from water droplets appear white to gray. For particles with diameters much larger than the wavelength (about

10λ) geometrical optics can be applied. Often the dimensionless size parameter x is used to determine whether to consider geometrical optics, Mie or Rayleigh scattering:

$$x = \frac{2\pi r}{\lambda} \tag{2.1}$$

Thereby r stands for the radius and λ for the wavelength. Rayleigh scattering is considered for $x \ll 1$, for $x \gg 1$ geometrical optics can be applied and for $x \approx 1$ Mie scattering is suitable.

2.2.1 Mie scattering

The Mie solution solves Maxwell's equations for spherical scatterers with a size in the range of the wavelength of the incident light. For light scattering by a single spherical particle in this size range, embedded in a homogeneous medium one can calculate the scattering cross-sectional area C_{sca}. It depends on particle size, the incident lights wavelength and the refractive index of the particle and surrounding medium. For interaction of light with an absorbing medium, the area of the incident wave that is absorbed C_{abs} has to be considered similarly. The sum of both gives the total extinction cross section [2]:

$$C_{ext} = C_{sca} + C_{abs} \tag{2.2}$$

For a non-absorbing medium thus $C_{ext} = C_{sca}$ applies, which is assumed in the following. The scattering cross-section defines the absolute area on which the scattering takes place. It is different from the actual physical cross-section, due to diffraction of light in close proximity to the particle. In Figure 2.2 a) the scattering cross-sections of different materials as a function of the particle diameter are compared. The data was generated using the MiePlot computer program [35], which is based on Bohren and Huffman's code for electromagnetic scattering by spheres known as BHMIE [27, 36]. Here, we consider spherical non-absorbing particles at an incident light of 550 nm wavelength and a surrounding medium with n=1.5. The refractive indices used for calculation were 2.75, 2.0 and 1.0 representing TiO$_2$, zinc oxide (ZnO), and air, respectively. However, without considering the physical cross section of the scattering particle, no statement can be made about the different materials scattering ability. Due to the dependence of C_{sca} on the physical size of the particle, it is useful to normalize it. This is done by dividing C_{sca} by the area of the geometric cross section of a spherical particle of radius r [27, 2]:

$$Q_{sca} = \frac{C_{sca}}{\pi r^2} \tag{2.3}$$

Thereby, one separates the intrinsic light-scattering strength from the influence of the physical size of the particle and receives the dimensionless scattering ef-
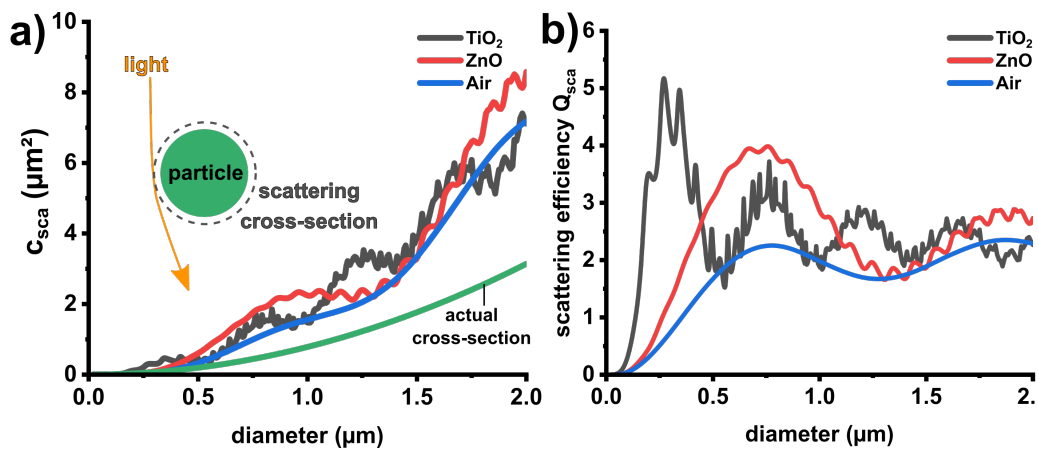
Figure 2.2: a) Scattering cross-section C_{sca} of spherical particles of different refractive index and particle size. The C_{sca} is larger than the geometrical cross-section of a spherical particle, because light travelling in close proximity to a particle of different refractive index than the surrounding medium changes its path due to diffraction. b) Normalized to the geometrical cross-section one gets the scattering efficiency Q_{sca}. The data was calculated with MiePlot [35].

ficiency Q_{sca}. The respective extinction and absorption efficiencies Q_{ext} and Q_{abs} can be calculated analogously. The higher the scattering efficiency Q_{sca}, the stronger is the scattering. It depends on the refractive index contrast between the surrounding medium and the particle, on the wavelength of the incident light and on the particle size. Q_{sca} can exceed one due to the fact that a particle can scatter more light than actually hits its physical cross section. In Figure 2.2 b) the scattering efficiency Q_{sca} of different materials is shown as a function of the particle diameter for incident light of 550 nm wavelength and a surrounding material with refractive index n =1.5. TiO$_2$ and ZnO are both common white pigments. TiO$_2$ has a refractive index of n = 2.55 - 2.75 [37] depending on the crystal configuration. ZnO has a lower refractive index with n = 2.0 [38]. Air with n =1 is to imagine as a spherical air-inclusion in the surrounding material. For TiO$_2$, for example, this ideal particle size is in the range of 200-300 nm. TiO$_2$ can scatter light particularly well due to its high refractive index and the resulting high contrast to the embedding medium, followed by ZnO and then the air inclusion. Although TiO$_2$, for example, seems to have a clear advantage due to its high refractive index, the strategy of using air as a scattering center is highly beneficial from a material efficiency perspective. In addition, one has to consider the numerous disadvantages of conventional pigments such as the energy-intensive production, the issue of environmentally harmful by-products and the potential health risks for humans, as discussed in detail on TiO$_2$ in Chapter 4. Examples

from nature, where suitable base materials are synthesized at ambient conditions and their efficient use is vital, show how scattering can be implemented efficiently with air as low refractive index material.

2.2.2 White appearance in living nature

In nature very efficient light scattering strategies have evolved, which combine a transparent matrix material as high and air as low refractive index component to provide the necessary refractive index contrast. Typical matrix materials in nature are cellulose, chitin, and keratin exhibiting refractive indies of only 1.47, 1.54 and 1.55, respectively, at a wavelength of about 580 nm [39, 40]. Intensive research was carried out on white or white patterned insects, such as butterflies [41, 42] and beetles [15, 43, 44]. Typically, butterfly wings are densely covered with overlapping scales, as shown in Figure 2.3 a). The basic scale anatomy features ridges along the length of the scale (longitudinal ridges) joined by perpendicular cross-connections (cross ribs) [46]. These structures alone can act as light scatterers, resulting from the difference in refractive index with the surrounding medium air [41]. For scales that are unpigmented in the visble part of light a white color is created, as can be seen e.g. for *Heliconius melpomene*, whose white scales feature only this basic anatomy [41]. However the reflectance can be further enhanced by incorporating additional scatteres, as it was observed in some butterfly species such as *Delias nigrina* or *Pieris rapae* [41]. The scales of the latter for example have ellipsoidal beads with dimensions of about 100–500 nm lined up within the scale interior, as shown in Figure 2.3 a). In a cross section, the beads appear to be hollow surrounded by a 5–8 nm thick membrane [41]. The bead shape is assumed to be optimized for scattering of visible light [42]. Interestingly, for male *Pieris rapae* these beads contain the UV-absorbing pigment leucopterin [41, 42]. The resulting increased absorption coefficient in the UV-wavelength range leads to an increased refractive index in the visible wavelength range compared to pure chitin [42].

Another type of light scattering beads can be found in the white patches on the longhorn beetle *Calothyrza margaritifera*. These are covered with hair-like chitinous scales, which contain spherical chitin beads of an average diameter of about 300 [15] to 550 nm [43], as shown in Figure 2.3 b). The white beetle of the genus *Cyphochilus* has been object of several studies, as it obtains an astonishingly high reflectance of about 60 to above 70% [15, 44] with very thin scales of only about 5-7 μm thickness [47, 48]. These scales (see Figure 2.3c)) possess an internal porous chitin network composed of cylindrical filaments of about 250 nm in diameter, which are separated by air voids of approximately 600 nm in width [15, 47, 49]. The filling fraction of the filaments seems to be optimized for effective light scattering [15] and minimal material use [50].
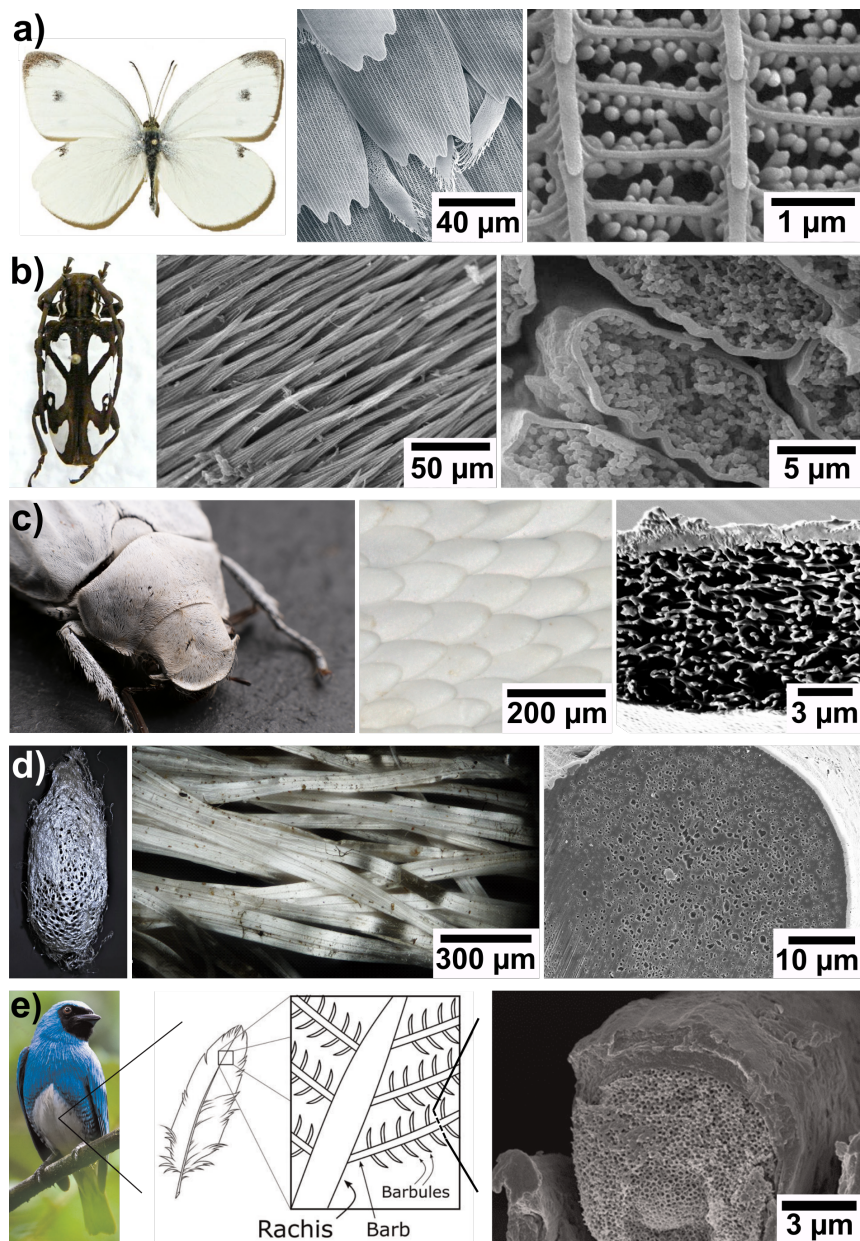
Figure 2.3: Examples of white appearance in nature created by nanostructures. a) The butterfly *Pieris rapae* has wing scales set with beads, adapted from [41, 42]. b) The beetle *Calothyrza margaritifera* has hair-like scales filled with spheres, adapted from [43]. c) The scales of the beetle *Cyphochilus insulanus* contain a porous network of interconnected filaments, photograph by Marcus Breig. d) The cocoon of the comet moth *Argema mittrei* is made of silk fibers interspersed with air voids, adapted from [22]. e) The male swallow tanagers *Tersina viridis* belly feather barbs contains air voids, adapted from [45].

10

While in the strategies presented so far the material with the high refractive index is the scattering center, in the form of spheres, ellipsoids or filaments, there are also strategies in which the scattering center is formed from the low refractive index medium air instead.

The cocoon of the comet moth *Argema mittrei* is composed of silk fibres of about 50 μm diameter [22] and both, the coocon as well as the individual fibres exhibit a silvery white appearance, as shown in Figure 2.3 d). This is due to light scattering caused by the elongated air inclusions that propagate through the length of the fiber [22]. The cross-sectional sizes of the air inclusions correspond well with the wavelength range of visible light with sizes ranging from a few tens of nanometers to about a micron. Thereby single fibers achieve a high reflectance of more than 60% [22]. An additional material property of the comet moths silk is its high emissivity in the mid-infrared [22], a feature which will be discussed in further detail in Chapter 5 on the subject of passive radiative cooling.

The white color impression of birds plumage is on the one hand caused by multiple reflections at the surfaces of the hierarchical arrangement of adjacent barbs and finer barbules (see Figure 2.3 e)) [51, 52]. On the other hand reflections and scattering caused by foam-like nanostructures (the spongy matrix, medulla) in the feather rachis and barbs contribute to the white appearance of unpigmented feathers [45, 51, 52, 53]. As an example the male swallow tananger *Tersina viridis* with its white belly feathers and barbs permeated with air inclusions is presented in Figure 2.3 e) [45].

These biological materials with refractive indies in the range of 1.47 to 1.55 [39, 40] achieve effective light scattering, although the refractive index is much lower than that of conventional pigments. These low refractive indices are however in the same range as for several industrially commonly used polymers [39]. That suggests that these, despite their low refractive index compared to white pigments, also have the potential to effectively scatter light when used in conjunction with air inclusions. An especially advantageous method to generate light scattering nanopores in technical polymers is the so-called supercritical CO_2 foaming, which will be described in detail in Chapter 3.

2.3   Analytical methods

2.3.1   Scanning electron microscopy

For the assessment of the porous structures created by foaming cross-sections of foamed polymers were investigated by scanning electron microscopy. The scanning electron microscope (SEM) uses an electron beam instead of light. The electrons are emitted by the cathode, pass a Wehnelt cylinder (a hollow cylinder

acting as an aperture) and are accelerated by a voltage of 0.5 to 30 kV towards the anode. The assembly of cathode, Wehnelt cylinder and anode is termed electron gun [54]. The beam diameter of about 10-50 μm has to be reduced and focused on the sample. This is done by a lens system of one or more condenser lenses, apertures and an objective lens, achieving a beam spot size of about 5-10 nm. Two beam deflection coils for x- and y-deflection in front of the objective lens scan the sample surface line-by-line with the electron beam. The sample is placed on a stage below the microscope column, the electrons are detected subsequently to their interaction with the sample. For gaining information concerning the surface topology mainly the low energy secondary electrons are collected by detectors located lateral above the specimen and visualized subsequently. In order to minimize spreading and attenuation of the electron beam by gas molecules the microscope column and the specimen chamber have to be evacuated. As non-conductive samples suffer charge effects, thus to obtain high resolution images especially at high magnifications, non-conductive samples are often coated with an electrically conductive metal. The non-conductive samples in this study have been sputtered with silver at 25 mA for 120 seconds. In this work a Zeiss SUPRA 60 VP was utilized. The image processing package Fiji was used for measuring the sizes of the structural features of interest [55]. For visualization of the inner pore structures of the samples cross-sections were prepared with freeze-fracturing in liquid nitrogen.

2.3.2   Optical microscopy and spectrophotometry

For a first assessment of the light scattering abilities of samples in the visible wavelength range optical microscopy was used. Hereby the microscope *Axioscope 5/7/Vario* equipped with a *Axiocam 305 color* camera and the software *ZEN core V 3.0* (all from *Carl Zeiss Microscopy GmbH*) was utilized. Measurements on the micrographs were carried out using the image processing package Fiji [55].

A spectrophotometer was used to evaluate the optical properties of the porous samples in terms of reflectance. From a broadband light source, the light is guided through a slit and then separated into different wavelengths by means of a movable diffraction grating. Only the light of a specific wavelength is passed through an output slit subsequently. The wavelength passing through is controlled by the position of the grating. The light beam is then directed to the sample via various mirrors. In conjunction with an integrating sphere (Ulbricht sphere) both, the specular reflected and the diffusely scattered part of light can be collected. This is particularly advantageous, as the diffuse component of the reflection is predominant for the porous structures in this study. The inner walls of the sphere are covered with a white, highly reflective coating, thus incident light undergoes multiple diffuse reflections and is distributed equally all over the spheres inte-

rior. The experimental setup for transmittance and reflectance measurements is shown in Figure 2.4. For transmittance measurements the sample is placed in
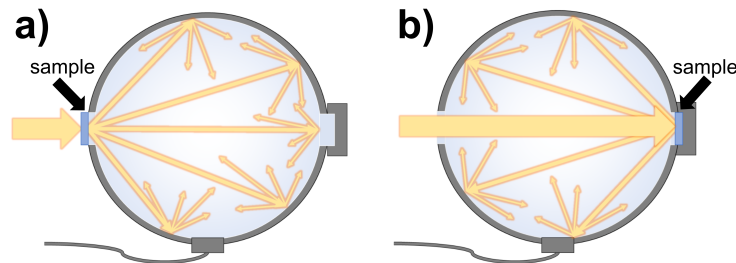
Figure 2.4: Integrating sphere with sample placement for a) transmittance and b) reflectance measurements. The transmitted respective reflected light is scattered multiple times on the highly reflective inner walls of the sphere.

front of the integrating sphere and the light passing through is collected (Figure 2.4 a). For the reflectance measurement the sample is placed at the exit port of the integrating sphere (Figure 2.4 b). The incident light strikes the sample and the reflected light, diffuse as well as specular, is detected. Partly transmitted light does not contribute to the measurement, as it is absorbed by the black cover lid behind the sample. For separate measurements of the transmittance (T) and reflectance (R) the Kirchhoff relationship applies [56]:

$$R + T + A = 1 \tag{2.4}$$

Considering a material with no absorbance (A) the transmittance can be directly deduced from the reflectance, and vice versa. In this study the UV-Vis-NIR Spectrophotometer *Lambda 950* from *Perkin Elmer* has been used equipped with a Spectralon® coated 150 mm integrating sphere. A tungsten halogen light source emits in the visible (Vis) and near-infra-red (NIR) and a Deuterium light source covers the ultraviolet (UV). Thereby the nominal spectral range covered is 175 up to 3300 nm. All measurements were normalized with a diffuse reflectance standard Spectralon® from *Labsphere*.

2.3.3 Fourier-transform infrared spectroscopy

In order to evaluate the sample properties in the infrared range of the spectrum, which is crucial for passive radiative cooling applications, Fourier-transform infrared spectroscopy (FTIR) was utilized. Infrared spectroscopy measures the absorption of infrared light by a material. The absorbed light causes an excitation in terms of vibrations and rotations of molecular bonds having frequencies corresponding to the absorbed wavelength range. In contrast to the previously

described UV-VIS spectroscopy, where each wavelength is measured separately, all wavelengths are measured simultaneously in the FTIR spectroscopy. The infrared light originating from a broadband light source is modulated using an interferometer, then interacts with the sample and finally reaches the broadband detector. The generated interferogram is then converted into a spectrum by the Fourier Transform operation.
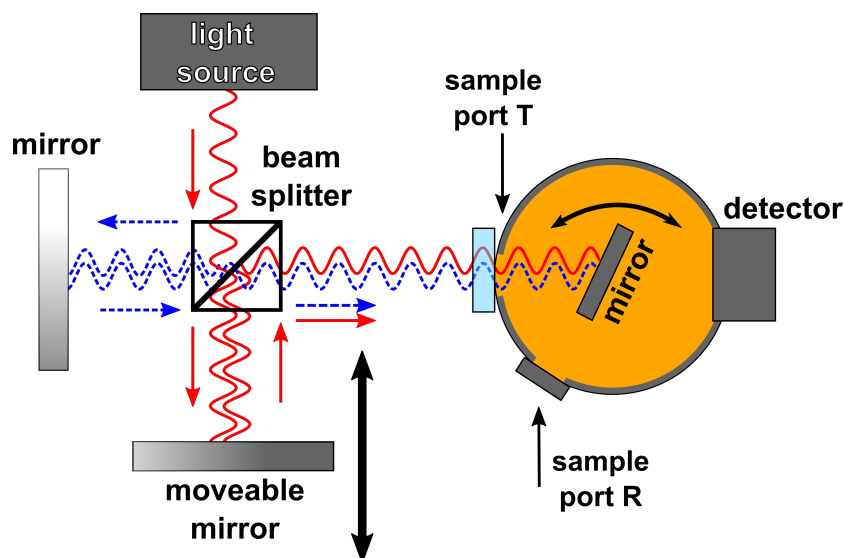
Figure 2.5: Scheme of the functional principle of a Michelson-Interferometer and the sample placement for transmittance and reflectance measurements, used in conjunction with an integrating sphere in FTIR measurements. For transmittance measurements the sample is placed at sample port T and at sample port R for reflectance measurements, respectively.

The central part is the Michelson-Interferometer, the functional principle is illustrated in Figure 2.5. The incident light is lead through a beam splitter, whereby one part is reflected (blue, dashed line) and one part is transmitted (red line). Both fractions of light are then again reflected by mirrors and lead back to the beam splitter. Again one fraction is transmitted and one is reflected. Reflected and transmitted part are rejoined and interfere with each other. Please note that there is also a reassembly of light fractions heading towards the light source, which is not shown here, as it does not contribute to the measurement. Depending on the position of the movable mirror the difference in pathway Δx of the two rejoined beam changes. When the light interferes at $\Delta x = m\lambda$ this results in a maximum in intensity. Thereby m is an integer, for $m = 0$ both mirrors would have exact the same distance to the beam splitter and the rejoined light is in phase as it has traveled exact the same distance. For a distance of $\Delta x = 1/2\lambda$ a minimum with zero

intensity is reached accordingly, due to destructive interference. All other distances in path length lead to intermediate intensities of the recombined beams. The photodetector records the light intensity of the rejoined beams as electrical signal, which oscillates at the same wavelength, as the original light input. For a broadband light source all the multiple wavelengths included are contained in the interferogram. With the Fourier Transform operation the interferogram is converted into a spectrum. When a sample is placed in the light path before the detector it absorbs certain frequencies (partially). This absorption alters the interferogram and thereby the resulting spectrum.

In this study the diffuse reflectance and transmittance of polymer samples has been examined with the FTIR spectrometer *Vertex 70* from *Bruker* in conjunction with a gold integrating sphere. Hereby, either the diffuse reflectance or transmittance are measured, depending on the placement of the samples and the rotation of the gold mirror inside the integrating sphere, as depicted in Figure 2.5. For transmittance measurements the sample is placed in front of the sphere and the inner mirror directs the light towards the inner sphere. Thereby all reflectance sample ports are closed with covers of the same material as the sphere coating. Analogous to integrating spheres tuned for the visible wavelength range, the infrared light undergoes multiple diffuse reflections and is distributed equally all over the spheres interior. For reflectance measurements the mirror directs the incoming light on the reflectance sample port.

2.3.4   Atomic force microscopy

Atomic force microscopy (AFM) is used in this work to obtain the surface topography of metallic molds and the respective counterparts embossed with them, as shown exemplary in Figure 2.6 b). The surface topography thereby is needed to evaluate the quality of the molding process at different process parameters (see Chapter 6). One main advantage apart from the detailed three-dimensional information about the surface structure, is that no conductive surface is needed. This is of special interest here, as sputtering would alter the samples optical properties and surface energy. With a sputtered surface the samples would be unsuitable for other subsequent analysis methods such as spectroscopy or contact-angle-measurements. Furthermore these AFM standard measurements can be performed at ambient conditions.

The measurement principle, depicted in Figure 2.6 a), is based on the detection of forces acting between a sharp tip and the sample surface. The pointed tip is in the nano-meter size range and ideally narrows to a width of only a few atoms. Depending on the distance of the tip to the sample, attractive forces such as Van der Waals and capillary forces act and, on the other hand, repulsions due to the Pauli principle or electrostatic forces occur. The tip is attached to a can-
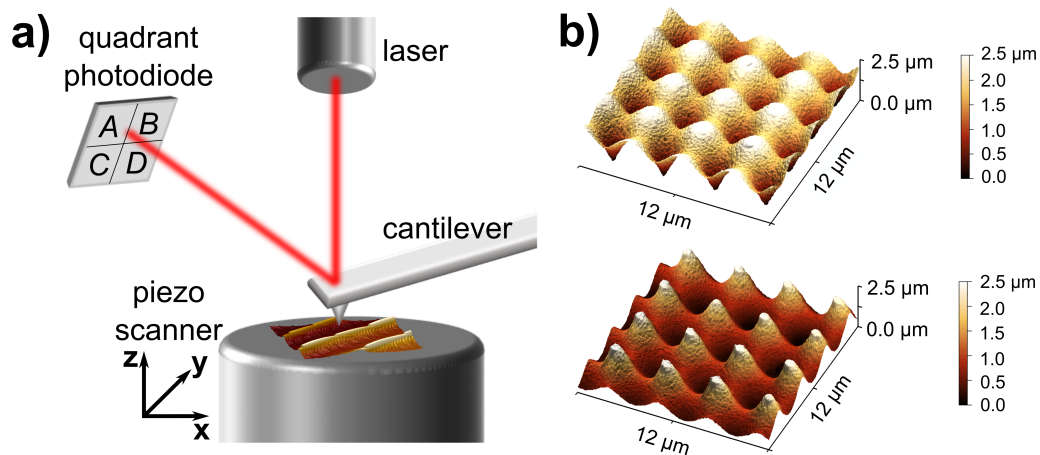
Figure 2.6: a) Scheme of the simplified measurement principle of an AFM. Deflections and torsion of the cantilever caused by interaction with the sample cause a deflection of the laser beam, which is detected by a four-quadrant photodiode. b) Surface height maps of a metallic microstructured mold (top), used as negative for the replication of the positive structure in PMMA (bottom). The color bar indicates the height of the profile.

tilever, which acts as a bending spring. When the tip approaches the specimen the surface interactions cause the cantilever to deflect. Attracting forces result in a downward deflection, while repulsive forces cause an upward deflection. A laser beam is focused on the back of the cantilever and reflected. Thereby any deflection of the cantilever will deflect the reflected laser beam. This is detected by means of a four-quadrant photodiode. Hereby the difference between quadrants A+B and C+D (see Figure (2.6) corresponds to cantilever deflections, while the difference between quadrants A+C and B+D accounts for torsion of the cantilever. In the constant-force measurement mode for example the force between specimen and tip and thus the bending of the cantilever, is kept constant. This is achieved by adjusting the z-position with piezoelectric elements through a control loop. The specimen is scanned in the x- and y-directions as well by means of piezoelectric elements. The topographical image of the specimen is then generated from the directional information obtained. The main operation modes of the AFM are the contact, the non-contact and the tapping mode. In contact-mode the tip is in direct contact with the sample surface, e.g. as described previously for the constant force mode. Main disadvantage is the wear of the tip and that the sample might take damage. In non-contact mode the tip hovers above the sample while being oscillated by piezoelements. As the oscillating tip approaches the sample, the frequency of the cantilever changes and can be used as a control

signal. In the tapping mode the oscillating tip slightly touches the surface. The excitation takes place at a fixed frequency close to the resonance frequency of the cantilever. Interaction between surface and tip change the frequency, thereby damping the amplitude of oscillation and the shifting phase. The oscillation amplitude can be used as control signal to readjust the distance via the feedback loop. The shift in phase is a material characteristic of the sample. So in addition to the topography also material properties can be detected. The topography measurements have been performed with *All-in-One* cantilevers from *Budget Sensors*. The AFM *Dimension Icon* ® from *Bruker* was used in this work and the software *Gwyddion* [57] was used for the evaluation of the recorded data.

Chapter 3

The CO_2 foaming process of polymers

For the fabrication of micro- and nano-porous polymers various approaches have been developed, of which phase separation techniques, imprinting and templating methods as well as foaming are the most common concepts [58, 59]. In foaming approaches the pore formation is induced by a gas, which evaporates out of a solvent, emerges from a chemical reaction during the polymerisation or is used either directly or in its supercritical state. This direct use of a gas as a physical foaming agent is the focus of this study. It has, compared to other foaming techniques, the advantage to leave no traces of solvents behind in the polymer [59]. The development of fine-celled polymer foams by this method started in the early 1980s at the Massachusetts Institute of Technology (MIT), which established the direct use of pressurized gases to create porous polymers exhibiting pores in the size range of 2 to 25 µm [60]. The since then emerging research on these gas-blown polymer foams first aimed for the fabrication of microcellular foams, which are defined by an average cell size of < 10 µm and a cell density of $>10^9$ cells/cm^3. Main target was to obtain weight reduction and therefore decreasing material costs, while having only minor losses in the mechanical strength. In addition to their beneficial mechanical properties microcellular foams show low thermal conductivity and the ability to dissipate impact energy [61, 62]. Meanwhile the development towards nanocellular foams progresses, targeting average cell sizes < 1 µm and cell densities $>10^{15}$ cells/cm^3, since further improvements in mechanical, thermal and impact properties are expected to occur [61, 62].

3.1 Procedure and principle of supercritical CO_2 foaming

In this study a batch configuration is used as foaming setup, hereby a polymer sample is positioned in an autoclave, which is sealed and subsequently pressurized with a gas. For the general procedure the autoclave is heated and the temperature is maintained during the process. The autoclave is connected to a gas source, in this setup it is a rising tube bottle for liquid CO_2. A syringe pump (*ISCO D-Series*) pressurizes CO_2, controls and maintains the desired pressure, in this case up to 50 MPa. The syringe pump holds about 260 ml of CO_2 at the given initial pressure of the bottle. A fast, reproducible release of the pressure is accomplished with a pneumatic valve (*NC 2000bar,1/4HP,DN3* from *SITEC-Sieber Engineering AG*). In the pressure-drop-method applied throughout this work a foam structure evolves in the polymer subsequent to the depressurization.

For understanding the foam formation mechanism a closer look on the interaction between the polymer and the applied gas at high pressure conditions is needed. The gas of choice in this study is CO_2, which became prevalent as a foaming agent, due to a range of advantages associated to it: It is an inert, non-flammable and not least inexpensive gas, as it can be obtained as a by-product from various chemical production processes [63]. It is non-toxic and therefore an environmental friendly replacement for conventional foaming agents, which are often harmful or leave, as mentioned previously, pollutant residues in the material [59, 63]. The supercritical state of CO_2 has remarkable diffusion characteristics with a liquid-like density and gas-like diffusivity, which are easily accessible at a pressure of P = 73.75 bar = 7.38 MPa and at a low temperature of 31.0°C [58, 62, 63]. Beside this, the main reason that (supercritical) CO_2 has gained this importance for foaming and various other polymer applications [63], is based on its ability to act as a plasticizer or solvent for polymers with good CO_2 solubility [64, 65, 66]. This phenomena of plasticization can be observed in the considerable decrease in the glass transition temperature T_g of an amorphous polymer (or the melting temperature T_m for a semicrystalline polymer), when exposed to CO_2 at high pressures [64, 65, 66, 67]. By absorption of CO_2 in its matrix the polymer can reach a viscous or rubbery state, where it softens and gets deformable at a much lower temperature, the effective T_g might even drop below room temperature under certain pressure conditions [68]. In the CO_2 foaming method this phenomena enables the growth of pores at low temperatures in a CO_2 supersaturated polymer, as summarized in Figure 3.1. First the polymer is saturated with CO_2 under constant, appropriately chosen temperature and pressure conditions, typically until the concentration of gas in the sample reaches the solubility limit. As CO_2 diffuses into the polymer matrix the T_g decreases,
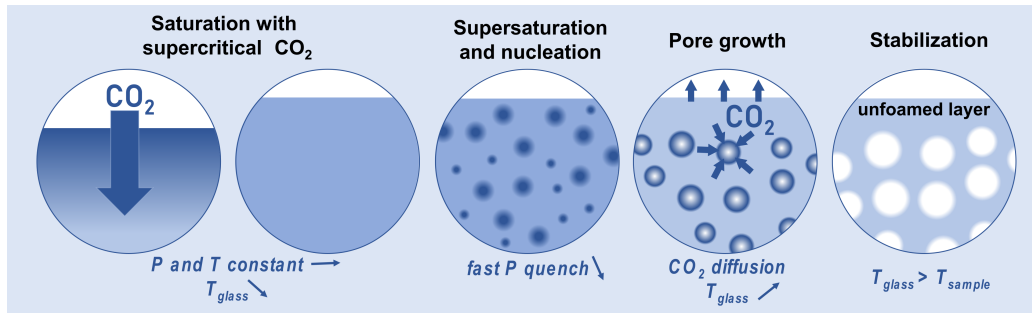
Figure 3.1: Scheme of the applied foam formation mechanism: The polymer is saturated with CO_2 under constant temperature and pressure conditions until solubility limit is reached, whereby the polymers T_g decreases. As the pressure is released rapidly, the solubility of CO_2 in the polymer matrix decreases. The polymer is supersaturated under the new pressure and temperature conditions and nucleation occurs. Pores start to grow due to CO_2 diffusing out of the polymer matrix into nuclei of a critical size. Hereby, the T_g increases again and the foam structure finally stabilizes as T_g reaches T_{sample}. Pre-published by the author in [69].

the polymer thereby swells up and becomes viscous, when the temperature of the polymer is higher than its effective T_g at the given pressure and temperature conditions. In the next step a thermodynamic instability is induced either by the rapid increase of temperature or the sudden decrease of pressure. The latter pressure-drop-method has been applied in this study by releasing the pressurized gas from the autoclave. This depressurization causes a supersaturation of the polymer, as the solubility of CO_2 in the polymer matrix is much lower under the new conditions [70]. As a consequence of the supersaturation nucleation occurs, which is the first stage of the formation of a new stable thermodynamic phase within a metastable phase, in this context a gas phase in a supersaturated polymer [70, 62]. For further growth nuclei have to reach a critical size, above which the energy required to form the new stable phase is smaller than the energy gain from the formation of the new stable phase. So as the new phase has a lower free energy than the initial phase, the driving force of the phase separation is the difference in free energies between the two phases [62]. The higher the supersaturation, the lower is the activation energy to be overcome for nucleation [62, 70]. Subsequently pore growth can proceed due to gas molecules diffusing from the polymer matrix into the newly formed nuclei, which were able to overcome the activation energy for nucleation [70]. Finally the cell structure solidifies, either by cooling it down actively or by the stabilizing effects occurring due to the pressure quench [61]. As the gas diffuses out of the polymer matrix

and into the growing pores and the surroundings, the T_g rises towards its normal value under ambient conditions. The structure solidifies as T_g has risen to the actual temperature of the sample [71]. An additionally stabilizing mechanism is due to the Joule-Thomson effect -the fast decrease in temperature that occurs for most gases in case of a rapid expansion- which decreases the temperature of the sample during pressure quench [61].

Key parameters to control and tune the pore formation process and the resulting morphology of the porous polymer are pressure, temperature, pressure quench and saturation time [68, 72, 73]. The appropriate process parameters depend on the polymer to be foamed, its interactions with the gas used and the subsequent foaming mechanism (here pressure-drop) to be applied. Generally, the pore size increases with rising temperature, while the pore density decreases [68]. Due to the fast diffusion of CO_2 out of the sample during the pressure release a layer with depleted gas concentration near the surfaces is formed. Here the concentration of CO_2 is too low for nucleation and pore growth and the layer remains unfoamed, whereby its thickness decreases with increasing saturation pressure [72]. Since a thin unfoamed layer is targeted throughout this study, the highest possible pressure of the setup of 50 MPa was utilized. Amorphous polymers tend to absorb CO_2 in a greater extent than crystalline polymers [65, 67] and the solubility of CO_2 in most polymers is enhanced at lower temperatures [61], which must be taken into account when estimating the saturation time.

3.2   Estimation of the saturation time

For macroscopic samples such as pieces of bulk polymer or sheets, the CO_2 uptake and saturation can be determined by different weighing methods. The gravimetric method determines whether the sample is fully saturated by exposing the sample to CO_2 in an autoclave for varying periods of time. The sample is then taken out and weighed at regular intervals. Saturation is achieved when the weight of the sample remains unchanged. However this method is not accurate, as there will be rather unpredictable loss of gas during the depressurization and the subsequent removal of the sample out of the autoclave [62]. A more accurate option is the use of a magnetic suspension balance (MSB) for examining the gas uptake. Hereby the sample is attached to a magnet, levitated inside the autoclave and periodically weighed within, while the electronics of the balance stay at ambient conditions [70]. Unfortunately, this method has a limited pressure range typically up to 25 MPa [62], which is not sufficient for the high pressures of up to 50 MPa applied in this study. Another common method to estimate the uptake of CO_2 based on weight measurement are desorption experiments [62] as described in detail by Berens and Huvard [74]. Hereby the sample is first fully

saturated and rapidly taken out of the autoclave. Subsequently the weight loss of the sample is measured during the diffusion of CO_2 out of the polymer. The amount M_t of CO_2 still absorbed by the sample at the desorption time t is given by [74]:

$$M_t = \frac{w_t - w_0}{w_0} \tag{3.1}$$

Whereby w_t is the sample weight at time t and w_0 is the initial dry weight of the sample.

For Fickian diffusion out of a plane sheet [62, 75, 76]:

$$\frac{M_t}{M_\infty} = 4\sqrt{\left(\frac{Dt}{\pi l^2}\right)} = 4\sqrt{\frac{D}{\pi}} \cdot \frac{\sqrt{t}}{l} \tag{3.2}$$

with the equilibrium uptake M_∞ for $t = \infty$ and the sheet thickness l, desorption curves can be used to estimate the diffusion coefficient D and the CO_2 uptake in the polymer. The desorption curve is created by plotting M_t versus $\sqrt{t}$ [74, 77]. The amount of CO_2 in the saturated polymer M_0 before desorption ($t = 0$), is indicated by extrapolating the initially linear part of the desorption curve to the intercept [74], as shown exemplary in Figure 3.2.
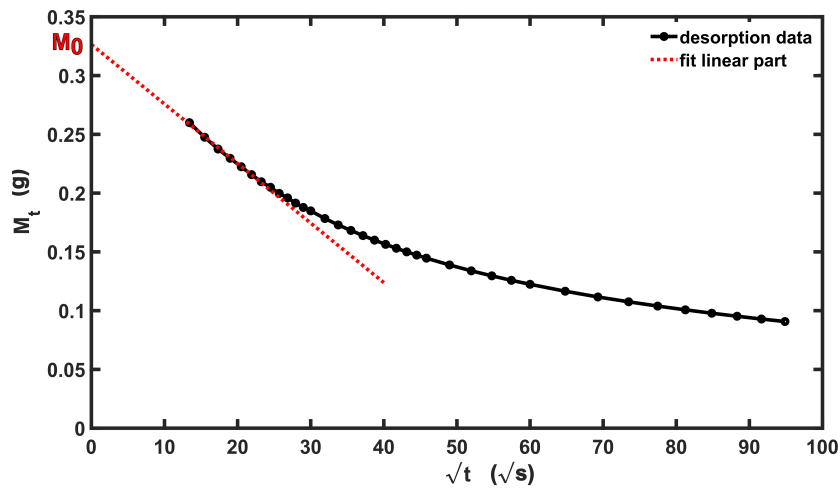
Figure 3.2: Desorption curve of a 1 mm thick PMMA sheet after 22 h saturation in supercritical CO_2 at 40°C and 50.5 MPa. The intercept of the linear fit indicates the amount of CO_2 in the polymer before the pressure release.

For thin films or small particles, as used in this study, however this method could not be successfully implemented. The reason is that the CO_2 escapes from the films or microparticles too fast to accurately measure the weight loss. This

is because the time between the pressure release and the removal of the sample from the autoclave for the weight measurement has to be considered. In the method described by Berens and Huvard [74] it takes only about 10 to 20 seconds, while in the high pressure measurement setup of the present study the removal of the sample from the autoclave takes at least about 2 to 3 minutes. The amount of gas loss during this removal procedure is unpredictable. This leads to inaccuracies due to the missing weight measurements in the time span shortly after the pressure release, this method therefore was not applied in the following. Furthermore the prerequisite for the precision of the described method is, that no visible changes in shape occur in the polymer [74]. The foaming, however, causes significant changes in the shape the applicability of the method is questionable here.

The saturation time can be estimated by literature values of the diffusion coefficient of CO_2 and the samples geometry. The CO_2 diffusion time can be calculated for a spherical sample geometry by [78]:

$$t_d = \frac{r^2}{D} \tag{3.3}$$

and for a planar film by [79]:

$$t_d = \frac{l^2}{D} \tag{3.4}$$

Hereby r is the radius of the particle, l is the thickness of the film and D is the respective diffusion coefficient of CO_2 in the polymer at the given pressure and temperature conditions. Webb and Teja obtained the diffusion coefficients for CO_2 in different polymers among them also PMMA, based on the previously described gravimetric methods [77]. For thick, transparent polymers, an appropriately modified autoclave with a viewing window can be used to study the diffusion front propagation during the absorption of CO_2 [80]. Nikitin et al. accordingly studied the pressure and temperature dependence of diffusion coefficient of CO_2 in PMMA, based on the observation of the diffusion front propagation versus time [80]. They observed a strong dependence on the molecular weight of PMMA, whereby the low molecular weight PMMA (120×10^3) has an around 10 times higher diffusion coefficient than the high molecular weight PMMA (4098×10^3). For the pressure range from 9 to 25 MPa at a fixed saturation temperature of 38°C the diffusion coefficient increases with higher pressure. At a fixed pressure of 12.5 MPa and an applied temperature range from 38 to 65°C the diffusion coefficient increased with temperature [80]. Li et al. studied the diffusion of CO_2 in PMMA of a molecular weight of 500×10^3 in a pressure range from 6 to 18 MPa and for temperatures between 30 and 70°C [81]. Here, too, the tendency was that higher saturation temperatures increase the diffusion coefficient.

Table 3.1: Literature values for the diffusion coefficient D of CO_2 in PMMA for different temperatures and pressures.

Temperature ($^{\circ}C$)	Pressure (MPa)	D $\times 10^{-10}$ ($\frac{m^2}{s}$)	Reference
40	10.5	1.04	Webb and Teja [77]
38		0.43	
50	12.5	0.44	Nikitin et al. [80] (high M_w)
65		0.5	
38	25	0.64	
38	25	6.8	Nikitin et al. [80] (low M_w)
30		0.65	
40		0.69	
50	18	0.76	Li et al. [81]
60		0.81	
70		0.9	

In summary low molecular weights and higher temperatures increase the diffusion coefficient, leading to a faster diffusion. Based on diffusion coefficients from literature (summarized in Table 3.1 for PMMA) one can estimate the saturation time of the polymer. Based on the diffusion coefficients of Nikitin et al. at 38°C and 25 MPa for example, a PMMA sheet of 1 mm thickness would have an estimated saturation time of about 25 min for low molecular weight material and for high molecular weight material about 260 min. Thus, if the molecular weight of the material is not known, there is sometimes a considerable time span to be considered for the saturation time.

In this study, the focus lies the achievement of a high reflectance, thus it is reasonable to use it as indicator for an additional experimental estimation of the saturation time. For this purpose, the sample, whose saturation time is to be estimated, was foamed at different saturation times, while temperature and pressure are kept the same. The foamed polymers are subsequently compared in terms of reflectance, the measurement of which is covered in detail in Chapter 2. If shape and magnitude of the spectrum do not change considerably with prolonged saturation time anymore, it can be considered sufficient for the present application case. At lower temperatures, more CO_2 can be dissolved for most polymers [61] and in addition the diffusion rate is lower [80, 81]. Hence the saturation time should be estimated for the lowest temperatures applied, because here the diffusion takes longer and more CO_2 is absorbed. Conversely, for higher temperatures less CO_2 can be absorbed and it diffuses faster, hence the estimates

made for lower temperatures will cover the saturation times expected for higher temperatures. In the current work the lowest foaming temperature applied is 40°C, which is therefore used for reflectance based saturation time estimations. In Figure 3.3 the spectra of a 1 mm thick PMMA sheet foamed after different saturation times is shown. At an exposure time of 15 min the polymer is obviously not sufficiently saturated to achieve a high reflectance, but after 60 minutes saturation the reflectance changes only slightly and the overall shape of the spectra is maintained. For thin films and particles in the micrometer range much shorter
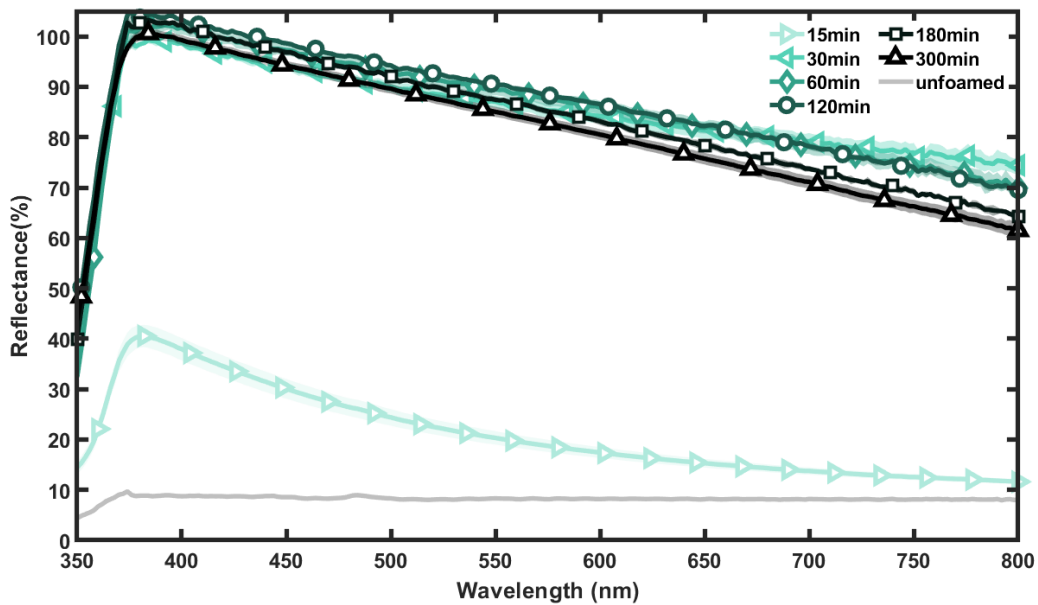
Figure 3.3: Reflectance of foamed PMMA samples of 1 mm thickness for different saturation times at 40°C foaming temperature and 50 MPa. The shaded areas indicate the respective standard deviation of three measurements.

saturation times are to be expected in dependence of the thickness or diameter, respectively. However in the setup used here the minimum exposure time should not be less than 10 min, since the system first heats up after the pressurized gas is introduced into the autoclave. Within the first 10 min, the temperature decreases to the target temperature again. If the pressure is released beforehand, the polymer will not be foamed at the specified target temperature.

Chapter 4

Porous polymeric microparticles as scattering white pigments

This chapter focuses on the search for alternatives to replace conventional white pigments, foremost the commercially highly relevant white pigment titanium dioxide (TiO_2). The sections 4.4, 4.5 and 4.6 of this chapter have been published in similar form by the author in Borgmann et al. [69]. The search for alternatives to TiO_2 pigments is of special interest due to critical sustainability aspects in the production and the intensifying discourse on potential health risks. These issues are discussed in more detail in the following and an overview of current replacement strategies based on porous polymers is given. In this work the strategy of utilizing air inclusions as scattering centers is implemented by foaming of initially transparent polymethyl methacrylate (PMMA) microspheres with supercritical CO_2. The properties of the foamed, white polymeric pigments with light scattering nano-pores are evaluated as possible replacement for TiO_2 pigments.

4.1   Industrial production of TiO_2 pigments

The production of TiO_2 accounts for more than 90% of the global titanium mineral consumption [37, 82]. TiO_2 pigments are produced either by the sulfate or the chloride process, of which each requires different raw materials and refinement steps, which are summarized in Figure 4.1 [37, 83]. From the naturally occurring titanium ores used for TiO_2 production the most relevant source is ilmenite, a titanium-iron oxide mineral in the form of sand or rock [12, 84]. Other naturally occurring ores used for the production of TiO_2 pigments are leucoxen and rutile, which are both emerging from weathering of ilmenite [37]. These titanium ores are further processed to produce "titania slag" or "synthetic rutile",

26

which then is suitable for the production of TiO_2 pigments either by the sulfate or the chloride process [37]. The refinement of ilmenite to titania slag is done by means of highly energy intensive processes [12] such as the Sorel process where the chemical reduction of the iron oxide content is done in an arc furnace [37]. While the titania slag is mainly used for the sulfate process, further refinement by thermal treatment or pressure leaching in hydrochloric acid (HCl) can be used to obtain "upgraded slag", which has a higher TiO_2 content of at least 85%, making it suitable also for the chloride process [12]. The most common refinement process of ilmenite and leucoxen to synthetic rutile are the Benilite process and the Becher process, respectively [37]. Without going into too much detail here, it should be noted that the Benilite process requires a carbonaceous energy carrier such as heavy oil, high temperatures of 850 - 1100°C in a rotary kiln and a subsequent acid leaching procedure with HCl [12, 37]. The Becher process is carried out in a rotary kiln at about 1200°C, subsequent leaching is done with an ammonium chloride (NH_4Cl) solution [12]. On the basis of titania slag, synthetic and natural rutile, which are obtained under high energy consumption, finally TiO_2 pigments can be produced either by the sulfate or the chloride process.
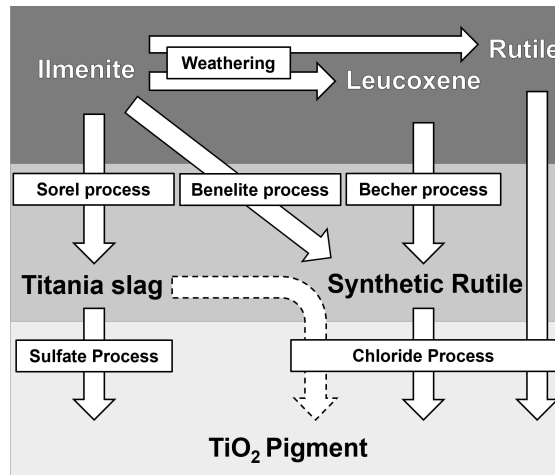
Figure 4.1: Main titanium ores, their refinements and the processes used for the production of TiO_2 pigments. Adapted from [37].

In the sulfate process ilmenite or the further refined titania slag serve as base material and are dissolved in highly concentrated sulfuric acid (H_2SO_4) enriched with sulfur trioxide (SO_3) [37, 83]. The resulting titanyl sulfate ($TiOSO_4$) is thermally hydrolyzed, thereby metatitanic acid ($TiO(OH)_2$) precipitates out [37]. In this step rutile seed crystals can be added, if pigments in the rutile rather than in the anatase crystal configuration are desired [37]. The TiO_2 crystals are grown in a kiln with processing temperatures of up to 1000 °C [37]. The kiln temper-

ature and the addition of anneling salts (e.g. aluminium-oxide) are used to tune the particle size and to improve weathering resistance [37, 83]. Main disadvantage of the sulfate process is the necessary recycling and disposal of the waste products ferrous sulfate and dilute sulfuric acid and the emission of sulfur oxides from the kiln to be avoided [12, 83].

In the chloride process natural and synthetic rutile and sometimes suitable high grade titanium ores or further refined titania slag are used. The base material reacts with chloride and the carbon source coke at temperatures from 900-1000 °C [12, 37]. As it is an exothermic reaction controlled internal and external cooling of the reactor is needed [83]. The resulting gaseous Titanium-tetrachloride ($TiCl_4$) is then condensed and further purified by distillation and other chemical treatments to reduce impurities such as metal chlorides originating from the base material [12, 37, 83]. In the last step the purified $TiCl_4$ is oxidized at temperatures above 1500 °C to form TiO_2 in the rutile crystal configuration [12]. Depending on the application, various subsequent surface treatments are usually necessary, which in turn have their own processes, associated by-products, energy balances and waste management issues, which will not be discussed further here, but are summarized in [37]. Although the chloride process is considered to be more environmentally safe than the sulfate process, here too non recyclable waste products such as un-reacted coke, ore solids and metal chloride solids are generated [12].

In summary both processes as well as the preceding refinements of the raw ores, are highly energy demanding. In addition one has to consider the mining of raw materials and the usually obligatory surface treatments on the pigments. Many of the chemicals used, their intermediates and their waste products are toxic, corrosive or generally harmful to the environment. Especially the costs of appropriate waste disposal have been responsible for large increases in the manufacturing costs of TiO_2 [83]. Therefore, cost effective alternative products are needed, which produce less or even no environmentally invasive contaminants and can be produced with less energy intensive processes [13].

4.2   Health concerns associated with TiO_2

In recent years, there have also been growing concerns that TiO_2 could be harmful to humans and the environment, especially when it comes to particle sizes in the nanometer range inevitably entering the environment [85, 86, 87, 88, 89, 90, 91, 92]. In order to derive policy measures the relevant scientific studies on health aspects of TiO_2 were reviewed and evaluated by different expert groups [4, 5, 6, 7, 8, 9]. In 2006 the International Agency for Research on Cancer (IARC) conduced an assessment on TiO_2, because findings from animal experimental

studies suggested that inhalation of TiO_2 particles causes cancer in the respiratory tract of rats [4, 93]. Therefore, humans could also be affected by TiO_2 dusts in terms of occupational exposure during the production, packing, milling, production site cleaning and maintenance. It was concluded that there was sufficient evidence that TiO_2 is carcinogenic in experimental animals and as a consequence the assessment group categorized TiO_2 as an IARC Group 2B carcinogen, meaning it is possibly carcinogenic to humans [4, 93]. The Committee for Risk Assessment (RAC) of the European Chemicals Agency (ECHA) decided in 2017 that the hitherto available scientific evidence meets the criteria of the Classification, Labelling and Packaging Regulation[1] (CPL) to classify TiO_2 as a category 2 substance via inhalation, which means it is suspected of being carcinogenic when inhaled[2] [94]. In 2020 the corresponding official regulation was published [95, 96].

In this context another aspect of human health with high political interest is the use of TiO_2 in the food industry, where it is known as food additive E171 to ensure a visually appealing appearance in a variety of edible products. In 2017 the National Research Institute for Agriculture, Food and the Environment (INRAE) - together with their scientific partners the French Agency for Food, Environmental and Occupational Health and Safety (ANSES), CEA-Université Grenoble-Alpes, Synchrotron SOLEIL and Luxembourg Institute of Science and Technology - published a study on the toxicity of TiO_2 in rats for oral exposure [6, 90]. In the animal experiment rats have been exposed to food grade TiO_2 particles in a daily oral dose, which is considered to be roughly equivalent to human exposure through food. It was shown that TiO_2 particles break through the intestinal barrier, enter the blood stream and can subsequently be found in the liver of the animals. After an oral exposure to TiO_2 particles for 100 days a harmful effect on the immune system of the animals was observed as well as intestinal inflammation and the indication of an initiating and also promoting effect of TiO_2 on the early stages of intestinal tumour formation in animals. It was emphasized that these results however cannot be extrapolated to humans [6, 90]. In 2019 ANSES conducted an actualized assessment upon political demand and considering the uncertainties regarding the harmlessness of TiO_2 it was recommended to limit the exposure to TiO_2 of workers, consumers and the environment, e.g., by favouring safe, non-nanomaterial and equivalent products [8]. Thereupon the French Minister for the Economy and Finance[3] and the Minister of State, Minister for Ecological and Solidarity Transition[4] decided as a precaution, to prohibit the marketing of foodstuffs containing TiO_2 for one year as from 1 January 2020

---

[1]In Europe the implementation in the legislation is done by the CLP

[2]corresponds to H351 through the inhalation route in the GHS

[3]Ministre de l'économie et des finances, Bruno Le Maire

[4]Ministre d'Etat, ministre de la transition écologique et solidaire, François de Rugy

[10]. A study from 2020 addressed the question if pregnant women are exposed to food grade TiO_2 nanoparticles and if a transfer through the placenta to the foetus is possible [97]. Human placentae as well as the first stool of newborns were examined as an indication of exposure to substances during pregnancy [97]. It was demonstrated that TiO_2 accumulated in the placenta, that it can passage across the human placenta and that it was present in the stool sample indicating the foetal exposure to nanoparticles [97]. The European Food Safety Authority (EFSA) stated in 2021, it could not be ruled out, that TiO_2 might cause DNA or chromosomal damage, thus it can not be considered as a safe food additive anymore [98]. As a consequence the European Commission banned TiO_2 as a food additive in Europe in January 2022 with a six months phase-out [11]. The ban on food-grade TiO_2 in Europe and upcoming insights from the ongoing research will probably further intensify the controversial political debate on the use of TiO_2, whether used in food or in other consumer goods. It is quite likely that this further stimulates consumer awareness on possible harmful effects of TiO_2, especially since its utilization in foods serves only an aesthetic aspect. The growing interest of many companies in completely unobjectionable alternative products is certainly due to both aspects.

4.3 Alternative strategies for effective scattering with low refractive index materials

The success of TiO_2 as a white pigment is based on its ability to scatter light particularly effective due to its high optical density and its lack of absorption in the visible range of light. With a refractive index of 2.75 in the rutile and of 2.55 in the anatase configuration TiO_2 achieves a high refractive index contrast to the embedding medium, e.g. transparent polymers or the binder of a paint [37]. As described previously, in nature efficient light scattering is often achieved by air-pores in a transparent matrix. The refractive index of air is low compared to the surrounding medium and provides the required refractive index contrast. Typical bio-polymer materials such as cellulose, chitin or keratin exhibit a refractive index of only 1.47 to 1.55 [39, 40], which corresponds well with the refractive index range of several industrially common polymers [39]. That suggests that these, despite their low refractive index, also have the potential to effectively scatter light when used in conjunction with air inclusions.

Indeed, while well known all along from nature, more recent technical implementations of this principle have been developed either analogously or in some cases might be even inspired by nature [99], in particular the paint industry has addressed the topic. The so far most significant implementation [100] of this prin-

ciple are hollow polymeric spheres featuring a single air void within a polymeric core based on the invention from Kowalski and Vogel in 1984 [101, 102]. Available under product name *ROPAQUE™* the hollow-sphere polymeric pigments are used as opacifiers for the partial substitution of TiO_2 in paints and feature typical particle sizes of 400 nm [103, 104]. The production method is based on osmotic swelling, whereby an acid core polymer is encapsulated with a thermoplastic (polystyrene or acrylic) shell [105]. Due to subsequent addition of a basic solution the coated sphere swells by water intake upon osmotic pressure, the air void in the shell forms as the encapsulated liquid evaporates [105]. These shells are stable enough to withstand mechanical loads of paint application and drying [106]. However, higher mechanical strain could cause the destruction of the thin shell and thus cause a loss in opacity [13]. Another commercially available product is *Spindrift™*, spherical particles with up to 30 µm in diameter featuring submicron-sized air inclusions typically around 700 nm and therein incorporated TiO_2 particles [107]. Depending on the void size two different mechanism can be identified: For air voids smaller 100 nm the effective refractive index of the polymer matrix is decreased, which enhances the light-scattering ability of the TiO_2. For air voids in the size range of visible light the air voids scatter light in addition to the embedded TiO_2 [107]. Another direction that research has taken is the synthesis of polymer particles, referred to as nanorattles, that contain a single air void in which a single TiO_2 particle is trapped. Nanorattles are intended to improve the scattering ability of the incorporated TiO_2 by providing a higher refractive index contrast and by preventing agglomerations of TiO_2, which decrease the efficiency [108]. The formation principle of the air void is comparable to the previously described formation of hollow spheres, here though with an additional TiO_2 core. Even during the drying process the collapse of some nanorattles is observable, thus the resistance to mechanical stress is an open question [108]. A strategy for introducing porosity in aqueous latex paints is to emulsify droplets of a volatile fluid, which leads to cavities in the latex film after evaporation [107]. This however, is a specific strategy for this particular type of paint. Finally, sometimes TiO_2 replacements are a direct exchange with other materials such as ZnO or calcium carbonate ($CaCO_3$), whose fabrication is in turn associated with energy-intensive processes and the formation of by-products, which are discussed more in detail elsewhere, e.g. from Ruszala et al. [13].

In the following the fabrication of porous polymer particles with nano-sized air inclusions is presented. To introduce the porous structure supercritical CO_2 foaming is used, which is known to be suitable for a variety of polymers, as previously discussed in Chapter 3. It has the advantage to leave no solvent residues behind in the polymer [59]. The process parameters are controllable in a way, that pore size and density and thus light scattering properties of the polymeric particles can be altered. Additional advantage of the approach is the formation

of a closed and unfoamed outer shell of a few micrometers thickness around the porous core. The internal structure of the foamed particles and their resulting optical properties are investigated in the following to determine the most suitable process parameters. The mechanical stability is examined by means of micro compression and heating experiments. Finally, the suitability of the foamed particles for paints is demonstrated.

4.4 Materials and Methods

Supercritical CO_2 foaming, previously described in detail in Chapter 3, is utilized to create light scattering air pores in an initially transparent polymer. The polymeric raw material of choice, important considerations of process parameters and variations, as well as the analytical methods used are discussed in the following [a].

4.4.1 Polymer particles

Transparent, monodisperse, cross-linked PMMA microspheres *Spheromers* ® from *Microbeads* have been used as raw material in nominal diameters of 10, 20, 40 and 60 μm. These are typically utilized as mechanically robust additives for thermoplastics, coatings and paint formulations in order to increase scratch resistance and modify texture, gloss and structure [109].

Table 4.1: Properties of PMMA microspheres (*Spheromers* ®) according to corresponding technical data sheet.

Spheromers® Properties	10-60 μm
Coefficient of variation CV	< 5%
Refractive index	1.487 - 1.492
Particle density	1.2 g/cm^3
Glass transition temperature T_g	130°C
Hardness Rockwell HR	M80-M100

PMMA has a great affinity for CO_2 and is therefore well suited for CO_2 foaming [61]. Cross-linking modifies several properties, for instance the T_g increases compared to conventional PMMA [110, 111]. This is based on the reduction in molecular mobility induced through the conjunction of the linear chains by the

---

[a]Section 4.4 has been published in similar form by the author in [69].

cross-linking agent [110, 111]. Therefore, a higher temperature range for successful foaming is expected compared to previous studies [17]. Benefits of cross-linking of PMMA are not only the enhancement of the thermal stability, also the mechanical stability improves strongly and properties such as tensile strength, elasticity, surface hardness and chemical resistance increase as well [111]. These enhanced properties could be highly advantageous for the performance of the composite material containing the foamed microspheres.

4.4.2 Foaming parameters and variations

Foaming with supercritical CO_2 was tested in the temperature range from 60 to 150°C at a pressure of 50 MPa. CO_2 in a purity of 99,995 % (Kohlendioxid N45) from *Air Liquide* was used. Based on literature values for the diffusion coefficient of CO_2 in PMMA [80] and the spherical geometry of the particle samples [78], a saturation time of 30 min was determined to be sufficient for complete saturation of the 60 μm diameter microspheres and accordingly also the smaller diameters. To prevent contamination of the autoclave and the piping with microspheres, additional inserts must be used during the foaming process. These are metal housings that can be screwed directly onto the pressure inlet of the autoclave. Analogous to the construction of the autoclave, the base of the insert here also consists of a sintered plate to enable pressure equalisation, CO_2 diffusion and pressure release. Two sizes are used, in the following called insert I and II, with a capacity of about 3.8 and 7.6 ml respectively. After foaming the microspheres tend to form a solid pellet and must be mechanically brought back to the original powder state for further measurements. This is achieved for these laboratory scale quantities by means of a mortar. In a variation of the foaming process the microspheres are embedded in a diffusion barrier as depicted in Figure 4.2. This prevents the fast escape of CO_2 during the pressure release step as suggested by Orsi *et. al* [78]. The barrier is made of water-soluble polyvinyl alcohol (PVA) with a molecular weight M_w of 200000 (*Merck KGaA*). In accordance with the suggested procedure, an aqueous 5% (wt/vol) PVA solution was used as embedding solution. The particles were weighed into the solution in a concentration of either 1 wt% or 10 wt%. The first one was used for the preliminary examination by optical microscopy, the latter for the final procedure as it yielded the best results in terms of high reflectivity (see Figure 4.3). The particle containing solution was then filled into PDMS molds. After air-drying at room temperature for at least 72 h, a stable PVA foil with enclosed PMMA particles was obtained. Since the CO_2 has to additionally diffuse through the enclosing PVA barrier, the saturation time was increased to 120 min. After foaming the barrier film was dissolved in H_2O and rinsed several times. Finally the particles were filtered out and air-dried for further examination. For further optimization, polyvinylpyrrolidone
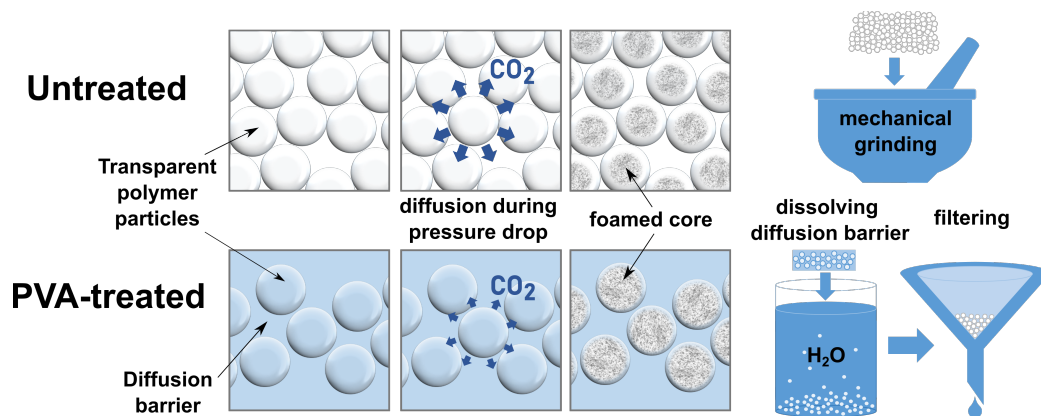
Figure 4.2: Preparation steps for foaming of untreated polymer particles and polymer particles embedded in PVA solution. The untreated particles loose CO_2 during the pressure release. The particles form a solid pellet after foaming and must be mechanically brought back to powder form for further use. Comparatively less CO_2 is lost in the pressure release step for particles embedded in a PVA barrier film. In addition to previous embedding, this procedure also requires the dissolution of the surrounding PVA layer in water and subsequent cleaning, filtering and drying of the particles. Pre-published by the author in [69].
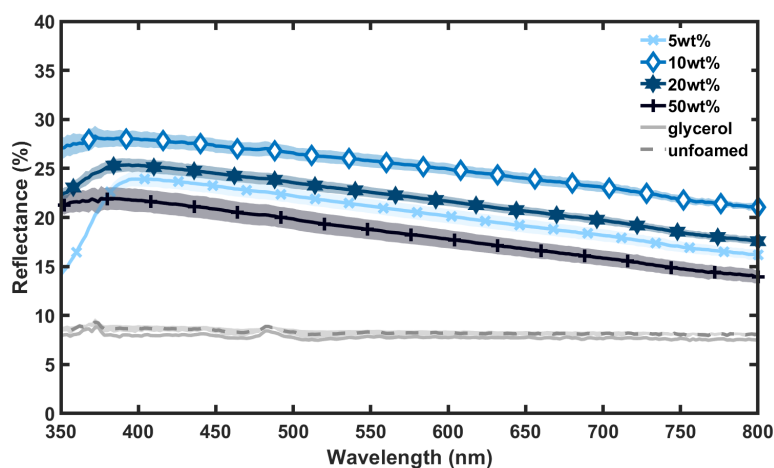
Figure 4.3: Reflectance spectra of PMMA microspheres with a nominal diameter of 60 μm in glycerol. All were foamed in a PVA diffusion barrier at 100°C, 50 MPa, 120 min but with different wt% of PMMA microspheres embedded in PVA. Each reflectance spectrum is averaged from 4 measurements and the shaded areas indicate the respective standard deviation.

(PVP) with a molecular weight of M_w 40000 from *thermo scientific* was tested as alternative water-soluble embedding material. Analogously to the embedding procedure with PVA an aqueous 5% (wt/vol) PVP solution was used.

4.4.3   Sample preparation techniques

For a first estimation of the foaming success optical dark field microscopy was sufficient. The particles were immersed in glycerol solution (*EMSURE® 85%* from *Sigma Aldrich*) to suppresses most reflections at the interface. The difference in refractive index of glycerol solution (n = 1.45 [112]) and PMMA (n = 1.49 [39]) is sufficient to perceive the outer boundaries of the particles. For the comparative analysis of the optical properties, foamed particles were embedded in a PMMA matrix to achieve a refractive index match. This ensures that light interactions of the porous cores will dominate, while nearly no reflections occur at the outer surface of the particles. Particles were embedded in a PMMA resin *SKresin 1390* from *S u. K Hock GmbH* with a concentration of 5 wt%. The formation of air bubbles in the resin was prevented by a vacuuming step. The mixture was cast in moulds of 25 mm diameter and 3 mm depth and cured with the UV-light source *Ultra Vitalux 300 W 230 V E27* from *Osram*. The fabricated sample disks were milled down and polished to a thickness of 1 mm, resulting in 5 to 7 disks for each sample. Another method applied for the comparative analysis of the optical properties in integrating sphere measurements is based on transparent solutions containing microparticles filled in cuvettes. This allowed a fast comparison of the samples, independent of high-precision tools and with less sample material required. Here a glycerol solution *EMSURE® 85%* from *Sigma Aldrich* was used with a 1 wt% concentration of particles. The 85% glycerol solution possess a very similar density to the polymer particles [112], which prevents the particles from floating up in the the cuvette during the measurement. For scanning electron microscopy all samples were sputtered with silver with a nominal film thickness of 15 nm. For the nano-CT individual microspheres were attached to needletips with a 2-component epoxy resin *UHU plus endfest 300* (*UHU GmbH & Co.KG*) by means of a micro manipulator.

4.4.4   Nano-CT

For a detailed study on the pore structures a phase-contrast X-ray nano-computed tomography examination (nano-CT) and subsequent data analysis was kindly carried out by Cristine Santos de Oliveira, the results of which are summarized in Figure 4.5. The study was conducted under the direction of Dr. Juliana Martins de Souza e Silva at the Institute of Physics at the Martin-Luther-Universität Halle-Wittenberg in Halle, Germany. The nano-CT was performed with a *Carl*

Zeiss Xradia 810 Ultra X-ray microscope operating with a Cr X-ray source (5.4 keV) and a fixed working distance. Each microsphere sample was glued to the tip of a stainless steel pin and mounted in the sample holder. Imaging of the entire microspheres was carried out in large field-of-view mode (LFOV). A total of 1001 projections with a field-of-view of 64 μm^2 and a pixel size of 64 nm were obtained over 180 degrees, each with an exposure time of 80 s. For the assessment of the pore size and pore density, imaging was carried out over the upper central axial section of the sphere using the high-resolution mode (HRES). Thereby two imaging experiments were done with projections having a field-of-view of 16 μm^2 and a pixel size of 32 nm. A total of 1001 projections were acquired, each with an exposure time of 60 s. Those two imaging experiments were virtually combined after reconstruction. Image reconstruction was done using the integrated software *XMReconstructor* from *Carl Zeiss AG*. A filtered back-projection algorithm was used and projections have been previously re-aligned using adaptive motion compensation to compensate for movement during the measurements. Images were exported as a stack of TIFF.

Image processing and segmentation was performed with *Avizo 9.4.0* software from *Thermo Fisher Scientific*. For LFOV measurements denoising of the virtual 3D images was performed using the non-local means filter in 3D using a search window of 21 voxels, a voxel comparison neighborhood of 5 voxels and a similarity value set to 1.0. The two HRES images from each sample were virtually aligned and stitched together using a Lanczos algorithm for the dataset merge. Image denoising for the merged data sets was performed in two steps: first a gaussian filter was applied in 3D with standard deviation set to 2 for all axes, then non-local means filter was applied in 3D using the same parameters as LFOV, but with a similarity value of 0.6. The segmentation of the microsphere pores in HRES was performed using the watershed algorithm, with starting seed threshold values based on entropy-criterion automatic segmentation [113, 114] applied in local regions of interest inside the sample. Pores with less than 15 voxels were removed to avoid noise being incorrectly attributed to pores. The porosity was estimated only for the region containing pores, from six volumes of interest with $160 \times 160 \times 160$ voxels, ensuring sampling of all the regions with varying porosity within the porous core. The measurement in these regions was conducted in HRES mode with a voxel size of 32 nm, which is well below the size of the majority of pores inside the polymer spheres.

4.4.5 Evaluation of thermal and mechanical stability

For evaluation of the thermal stability of the foamed particles a *HS-300 Type B Heating Stage* from *Spectrolab* was utilized. A sample of white particles foamed in PVA at 90°C was glued onto a 0.3 mm thick coverslip. The sample was exposed

to a temperature of 60-120°C for 10 min each and the result was evaluated by optical microscopy.

Micro compression experiments on foamed and unfoamed microspheres were kindly performed by Dr. Juan Li under the direction of Prof. Christoph Kirchlechner at the Institute for Applied Materials (IAM) at the Karlsruhe Institute of Technology (KIT). The examination was conducted with a *G200* nano indenter from *Keysight Technologies*, the particles were compressed by a diamond flat punch with 50 μm diameter. Individual particles were glued on a microscope slide and identified using the *G200* optical microscope. This assured that only a single particle was compressed at a time. The stage system has a positional accuracy within 1 μm. As loading function, a constant normalized force increase of $\dot{P}/P = 0.05\,s^{-1}$ with 2 s hold segment at the peak force was chosen.

4.4.6 Paint formulation

Either foamed or unfoamed particles were added to a transparent, synthetic resin dispersion binder *GERSTAECKER Acrylbinder* at a concentration of 20 wt %. A stencil of 1 mm thickness was used to apply the paint onto a transparent PMMA substrate. The wet paint layer had a thickness of 1 mm due to the use of the stencil. After drying the layer had a thickness of about 600 μm.

4.5 Results

Supercritical CO_2 foaming of PMMA microspheres and the pores created thereby are examined in the following[b]. Special focus lies on the changed optical properties and a variation of the foaming process for further improvement of the reflectance. Foamed microspheres are tested for their mechanical and thermal stability to estimated their suitability for application in paints, which is finally demonstrated by integrating foamed microspheres into a paint.

4.5.1 Microscopic examination of light-scattering pores

Foaming was performed at temperatures ranging from 60 to 150°C at a pressure of 50 MPa with 30 min saturation time. The success of pore formation was controlled by optical dark-field microscopy as shown in Figure 4.4. Due to light-scattering pores the foamed core can be distinguished from the unfoamed, transparent layer around it. The assessment of the unfoamed layer in the temperature

---

[b]Section 4.5 with the exception of subsection *Reflectance improvements by diffusion barrier foaming* in section 4.5.5 has been published in similar form by the author in [69].

range of 100 to 140°C showed typical average thicknesses of about 9 to 10.5 µm as summarized in Table 4.2.
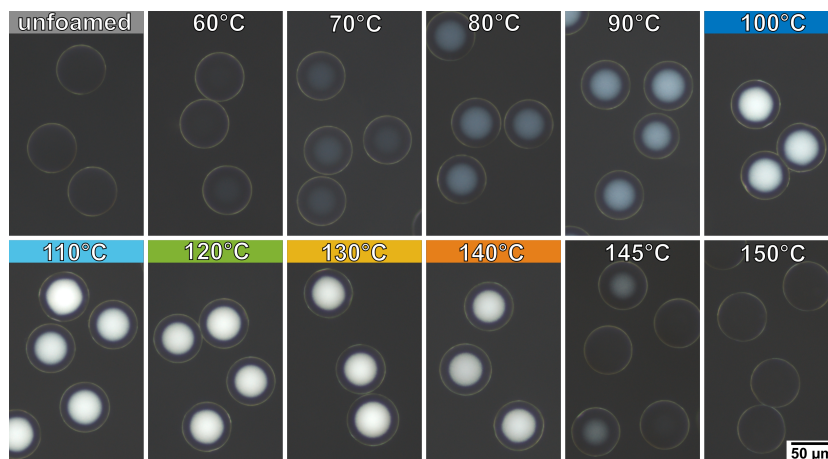
Figure 4.4: Optical micrographs of monodisperse PMMA microspheres with a nominal diameter of 60 µm retained in glycerol solution. The microspheres were foamed at temperatures from 60 to 150°C with otherwise identical parameters. Through foaming light scattering nanopores are formed inside the microspheres. The foaming appears most efficient in terms of a white appearance in the temperature range of 100 to 140°C, as highlighted by the colored bars. As the foaming temperature is further increased the foamed center diminishes, until no foamed core is perceptible. Pre-published by the author in [69].

A slight turbidity is already visible for foaming temperatures of 60°C compared to the unfoamed microspheres. With increasing foaming temperature the scattering effect increases. Microspheres, foamed in the temperature range from 100 to 140°C, have a clearly perceivable white core (see colored bars in Figure 4.4). Increasing the foaming temperature further, the scattering effect reduces. The microspheres foamed at 150°C appear as clear as the unfoamed ones. This result can be attributed to the higher diffusion rates at higher temperatures [80], by which too much CO_2 diffuses out to be available for foaming. An indication for this effect is the increased thickness of the unfoamed layer of about 14 µm for the microspheres foamed at 145°C (see Table 4.2). Consequently, the microsphere foamed at 100 to 140°C were selected for further evaluation of the pore size and density and corresponding changes in optical properties. The thus necessary production of a larger amount of particles was achieved by the use of the larger insert II for foaming in this temperature range. The corresponding thicknesses of the unfoamed layers of this foaming cycle is in the same range as for the use of the insert I (compare Table 4.2).

Table 4.2: Thickness of the unfoamed layer with corresponding standard deviation observed for untreated PMMA microspheres after foaming at varying temperatures and in different inserts.

T	Foaming insert I unfoamed layer	Foaming insert II unfoamed layer
°C	(µm)	
70	11.8±0.64	
80	9.8 ±0.51	
90	9.5 ±0.49	
100	9.5 ±0.62	9.9 ±0.59
110	9.3 ±0.57	8.9 ±0.74
120	10.1±0.56	9.4 ±0.62
130	10.1±0.38	10.0±0.39
140	11.0±0.42	10.4±0.60
145	14.0±0.86	

4.5.2 Pore sizes and density of foamed microspheres

The white appearance of some foamed particles in optical dark-field microscopy indicates scattering and thus pore sizes of approximately $\frac{\lambda}{2}$ [37]. For scattering of the visible range of light these have to be 200 to 400 nm in diameter. Based on this estimate it is of interest to verify if the pores are already in a size range that allows particularly effective scattering. For spherical air pores embedded in a matrix with a refractive index of $n = 1.5$, Ross predicted the highest scattering efficiencies for an air void diameter of 225 nm [115]. This estimation is applicable at void concentrations of less than 8 % by volume [115]. Park and Hong conducted an experimental study on the light scattering of films containing hollow polymer particles of different void sizes [116]. Maximum scattering was achieved for a void diameter of about 280 nm [116]. Auger and McLoughlin calculated the optimum void size at a void volume concentration of 15 % to be around $220 - 250$ nm depending on the theoretical framework applied [117].

Using nano-CT the pore size and density of the foamed microspheres was assessed to determine if the pores sizes are suitable to scatter light as effectively as possible. A particular advantage of this method is that it is non-destructive and provides detailed information about the internal three-dimensional microstructure achieved by foaming. Figure 4.5 a) shows the large field-of-view mode (LFOV) 3D virtual image from a microsphere foamed at 130°C. It reveals the foamed core within an unfoamed layer, corresponding well with the results al-

ready obtained by optical microscopy. An example of a high-resolution mode (HRES) measurement of the upper central axis of the microspheres is marked in blue in Figure 4.5 a). Figure 4.5 b) shows the corresponding 3D reconstruction with a cross-sectional view in c). The representative cross-sectional tomographic slices d) - h) in Figure 4.5 indicate the change in pore density and pore size associated with the variation of the foaming temperature. The corresponding histograms of the pore sizes (see d) - h) in Figure 4.5) can be fitted with a normal or a log-normal distribution [118]. Both result in similar values, whereby in this case the normal distribution offers a better fit and is therefore used here (see Table 4.3).

Table 4.3: Comparison of estimated average pore sizes for a normal, respective a log-normal distribution fit with corresponding coefficient of determination (R^2).

	Normal distribution		Log-normal distribution	
T	Pore size	R^2	Pore size	R^2
(°C)	(nm)	(%)	(nm)	(%)
100	181 ± 61	96.1	200 ± 76	97.7
110	214 ± 79	97.0	242 ±104	95.4
120	266 ± 94	97.8	299 ±120	93.3
130	289 ± 89	96.8	310 ± 89	90.6
140	295 ± 88	98.5	317 ± 93	94.9

With increasing foaming temperature the average pore size increases from 181 ± 61 nm up to 295 ± 88 nm in the temperature range from 100 to 140°C. Thus, the average pore size corresponds well within the predicted range for efficient scattering of visible light by air voids [115, 116, 117]. The porosity initially shows a distinct increase from only 3 ± 1 % at 100°C to 7 ± 2 % at 110°C and finally up to 12 ± 3 % at 120°C. Hereafter, the density remains in this range despite increasing foaming temperatures. This indicates that the maximum pore density that can be achieved under the given foaming conditions was reached. The estimated porosity for samples foamed at 100 to 140°C coincides very well with the range considered in previous studies [115, 117]. However, the pore morphology deviates from the assumed perfectly spherical air voids for the theoretical estimations. Volumetric images suggest that approximately spherical pores merge during foaming and result in larger pores with a random shape (Figure 4.5 b) and c), pores in red and green color). In general, it should be noted that the above results for pore size and density are for individual exemplary microsphere samples. Thus the next step is to further investigate the optical properties of a multitude
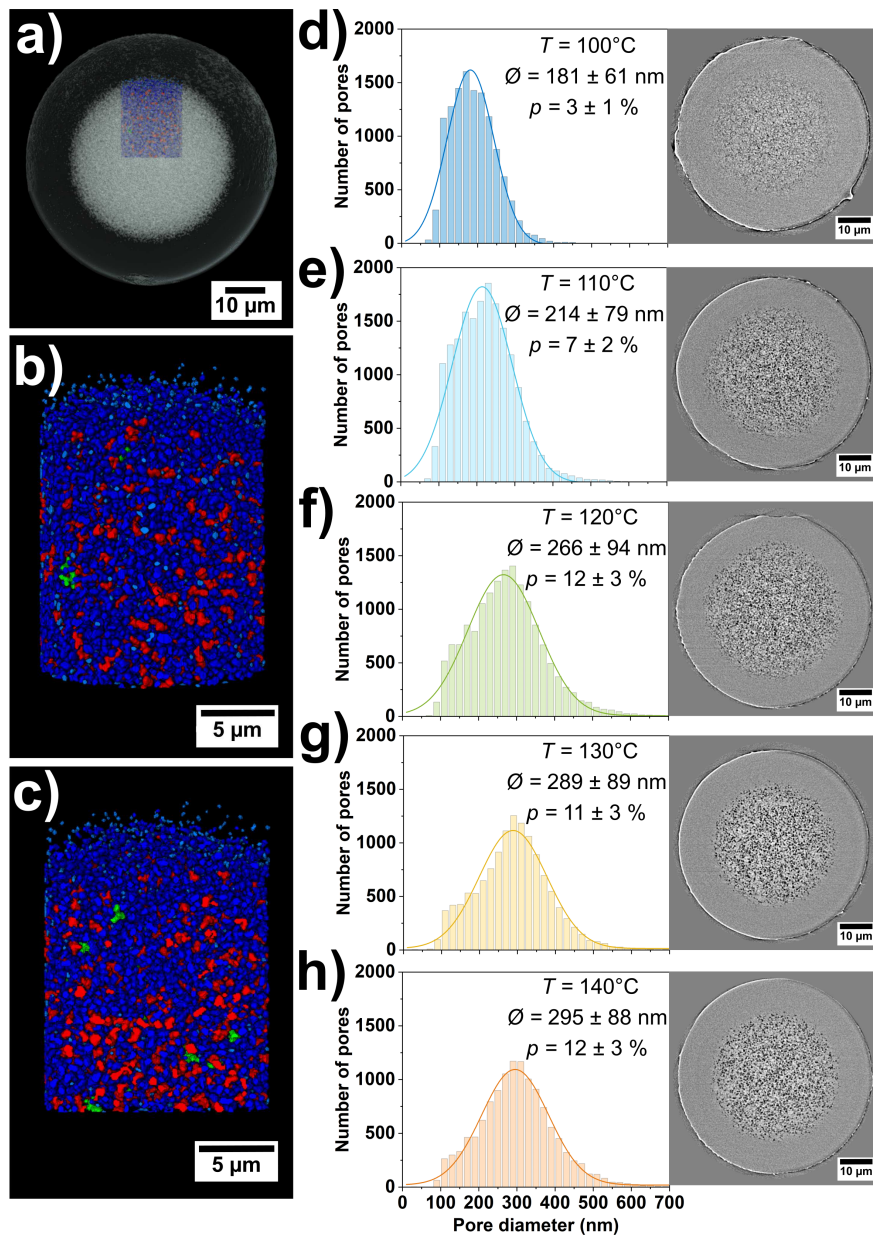
Figure 4.5: a) Nano-CT 3D virtual image of a microsphere foamed at 130 °C . The colored section marks the location of the high-resolution (HRES) measurements. b) Virtual image of the segmented pores in HRES and the corresponding cross-sectional cut in c). The colors correspond to pore diameters: light blue $0-250$ nm, blue $250-500$ nm, red $500-750$ nm, green $750-1000$ nm. d)-h) Representative cross-sectional tomographic images of microspheres foamed at 100 to 140°C with corresponding histograms of the pore sizes. The estimated average pore sizes is indicated by ø and the porosity by *p*. Pre-published by the author in [69].

41

of microspheres and to determine the best foaming parameters in terms of reflectance.

4.5.3 Optical properties of foamed microspheres

For comparison of the optical properties of the microspheres foamed at different parameters, these were embedded in PMMA at the same concentration. The resulting sample disks were subsequently trimmed to the same thickness. The reflectance spectra of these samples were measured over the wavelength range of 350 to 800 nm as shown in Figure 4.6.
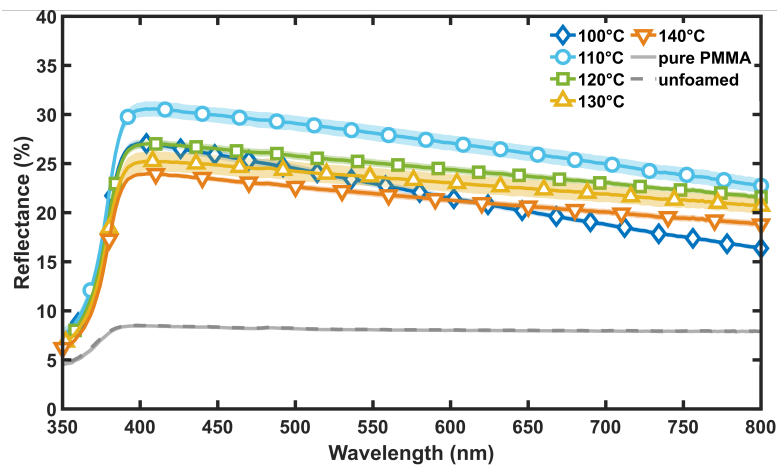
Figure 4.6: Reflectance spectra of sample discs containing microspheres foamed in the temperature range from 100 to 140°C. The microspheres are embedded in PMMA with a concentration of 5 wt%. The resulting sample discs were milled down and polished to 1 mm thickness. Each spectrum is averaged from 5 reflectance measurements and the shaded areas indicate the respective standard deviation. Pre-published by the author in [69].

Plain PMMA samples as well as samples with embedded unfoamed microspheres are transparent. The reflection of only about 8% is attributed to reflections at the smooth sample surfaces. This indicates the successful refractive index matching between the PMMA microspheres and the PMMA embedding material. The low reflectance below 400 nm of all samples is attributed to the short wavelength range absorption of the UV-curing PMMA resin. All foamed samples show increased reflectance with a slight decrease towards the longer wavelengths, which can be attributed to the decrease of the refractive index of PMMA from the short to the long wavelength range [39]. The nano-CT results show that the sample containing microspheres foamed at 100°C has the smallest pore

sizes of 181 ± 61 nm (see Figure 4.5 d)). It exhibits a steep increase in reflectance towards the shorter wavelength range, while showing the lowest reflectance of all foamed samples for wavelengths of $600 - 800$ nm. This can be explained by the dependence of the light scattering on the pore size, as smaller pores or particles tend to scatter short wavelengths stronger than longer wavelengths. Despite the low pore density of 3 ± 1 %, the reflectance is comparable to the samples foamed at 120 to 140°C, which all possess much higher pore densities (Figure 4.5 f)- h)). The highest reflectance is achieved for the sample foamed at 110°C, although the pore density has not reached its maximum here. The corresponding pore size of 214 ± 79 nm is in good agreement with the optimal pore size of 225 nm predicted by Ross [115]. With 7 ± 2 % the pore density is also within the valid scope of his prediction [115, 116]. The samples foamed at 120, 130 and 140°C have a higher pore density all in the same range with 11 ± 3 % to 12 ± 3 %. Therefore, the differences in reflectance between them is to be explained with the difference in pore size. The general trend of higher reflectance for shorter wavelengths could be an advantage as for many applications an increased reflection of the blue part of light is desired. This is because a bluish undertone is perceived as fresh for most humans compared to yellowish undertones [37].

4.5.4   Optimization towards reduced unfoamed layers

The previously achieved thickness of the unfoamed layer of around 10 μm might be a limiting factor, as it reduces the number of light scattering pores in the microsphere. The reduction of this skin layer is thus addressed as an optimization target. It is caused by the loss of CO_2 to the surroundings in the pressure release step [78, 119, 120]. The thickness of the unfoamed layer decreases with increasing saturation pressure [72]. Therefore, a high pressure of 50 MPa, which is the upper limit of the current setup, was applied. Orsi et al. reported the production of hollow particles by embedding polystyrene particles (50 to 0.2 μm) in a PVA-based barrier to prevent the loss of CO_2 during the pressure release [78]. CO_2 foaming with this surrounding PVA-barrier created cavities at the particle surface, which was proposed for the use as reservoirs for encapsulation for drug delivery [78, 121, 122]. Inspired by this study an aqueous PVA solution was utilized as embedding solution for PMMA spheres of 60 μm diameter. After solvent evaporation the particle loaded PVA samples were foamed within the temperature range from 50 to 150°C at 50 MPa, respectively. To account for the additional time needed for CO_2 to diffuse through the barrier, the saturation time was increased to 120 minutes [78]. After foaming the diffusion barrier was dissolved in H_2O. A comparison of the methods with associated pre- and post-processing steps is shown in Figure 4.2. After filtering and drying the particles were examined with optical dark-field microscopy, as described previously.
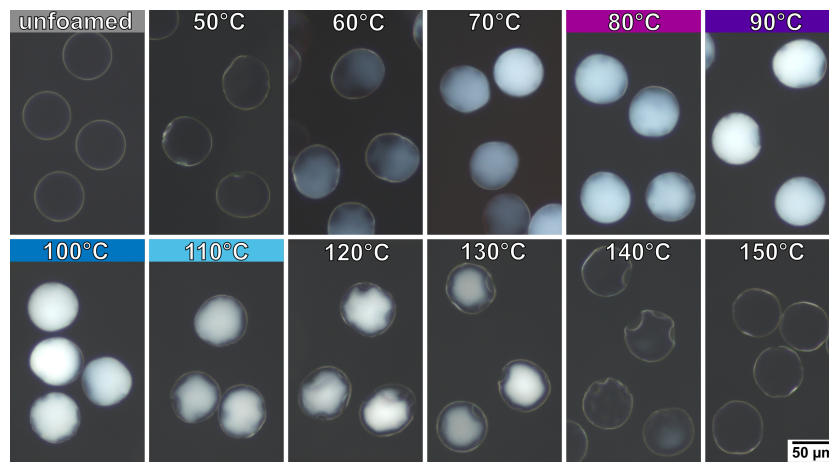
Figure 4.7: Optical micrographs of monodisperse PMMA microspheres with a nominal diameter of 60 μm in glycerol solution. The microspheres were embedded in a PVA diffusion barrier layer and foamed at temperatures ranging from 50 to 150°C with otherwise identical parameters. In this foaming variation the white color impression already appears in a lower temperature range of 80 to 110°C. The unfoamed layer is considerably reduced and distinct changes in the particle shape are observable. Pre-published by the author in [69].

The optical microscopy images in Figure 4.7 show the successful foaming in terms of a white color impression, which is achieved already at temperatures of 80 to 100°C. The unfoamed layer in this temperature range is already reduced to a thickness not resolvable by optical microscopy. Samples foamed at 110°C or higher show a thin unfoamed layer, its formation can be attributed to an increased viscosity of the PVA barrier layer to be expected with rising temperatures. Thereby more CO_2 can escape to the surroundings. The unfoamed layer has an irregular shape due to visible deformations of the particles. These occur mostly in the shape of rounded indentations at the surface. The layer thicknesses tend to be several micrometers thinner than those obtained without diffusion barrier, with average thicknesses of 6.0 ± 1.5 μm, 5.7 ± 1.4 μm and 6.9 ± 0.8 μm for foaming temperatures of 110, 120 and 130°C, respectively. However, the non-uniformity of the unfoamed layer impedes the accuracy of the measurement.

The reflectance spectra measured with an intergating sphere presented in Figure 4.8 show the reflectance of the PMMA sample discs containing particles foamed in a PVA-barrier film at 80 to 110°C, respectively. The sample discs have been prepared analogously to the previously embedded samples. Despite the reduced unfoamed layer, the reflectance obtained is within the same range as for the microspheres foamed without a barrier film. However, the direct comparison to the samples foamed at 100°C with and without diffusion barrier, shows an
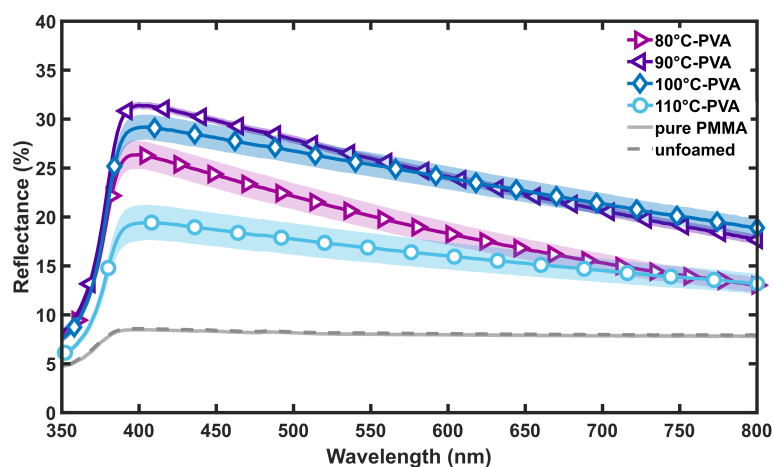
Figure 4.8: Reflectance spectra of sample discs containing microspheres foamed within a PVA diffusion barrier in the temperature range from 80 to 110°C. The microspheres are embedded in PMMA with a concentration of 5wt%. The resulting sample discs were milled down and polished to 1 mm thickness. Each spectrum is averaged from 5 reflectance measurements and the shaded areas indicate the respective standard deviation. Pre-published by the author in [69].

enhancement of the reflectance of a few percent over the whole spectrum (Figure 4.6 and 4.8). In contrast to this, the reflectance for the PVA embedded sample foamed at 110°C is strongly reduced compared to its pure foamed counterpart.

In summary, with otherwise equal foaming parameters the use of the PVA diffusion barrier yielded only a slight improvement of the reflectance properties. The optimal foaming temperature for high reflectance is shifted towards lower temperatures. Further investigations of the diffusion barrier concerning other molecular weights, different materials or the use of plasticizers might lead to an enhanced barrier function and thus making more CO_2 accessible to the pore formation. In general, the PVA diffusion barrier allowed the implementation of lower process temperatures, reduced unfoamed layers and has the potential to enhance the scattering properties.

4.5.5 Improvement towards smaller foamed particles

For varnishes, paints and paper mostly particles smaller than 60 µm are desired, as these products are processed to very thin layers. Also, foamed particles of 60 µm diameter are still distinguishable as granular turbidity within the embedding material, while smaller particles are not perceived as individual particles anymore. The use of a diffusion barrier could allow the foaming of smaller particles, which otherwise loose to much CO_2 during the pressure drop to achieve a

45

foamed core. PMMA particles of 10, 20 and 40 μm nominal diameter were embedded in PVA solution analog to the described procedure. Subsequently foaming was performed at temperatures of 80, 90 and 100°C. As shown in Figure 4.9 particles of 40 and 20 μm diameter have a foamed core at the temperature range tested. That is a considerable improvement, as for particles of 20 μm diameter no foamed core was achieved, when foamed without diffusion barrier. Particles of 10 μm diameter do not appear to have light scattering pores and are therefore transparent. Here deformations of the samples foamed with a PVA barrier are recognizable, too. Due to the resolution limitations of optical microscopy these are further assessed by SEM.
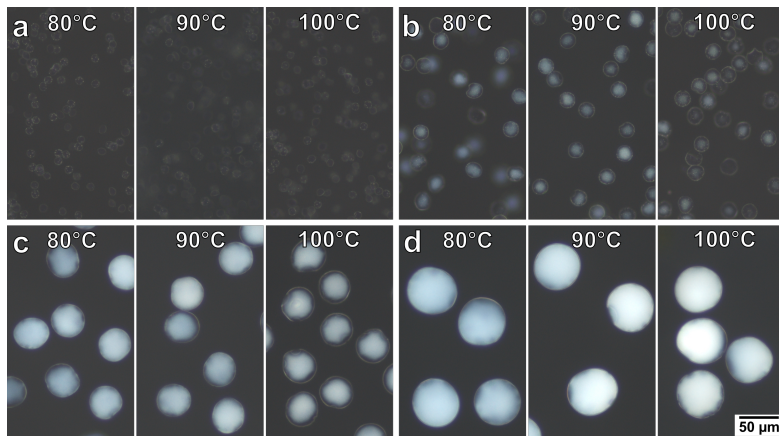
Figure 4.9: Optical micrographs of PMMA microspheres with nominal diameters of a) 10 μm, b) 20 μm, c) 40 μm and d) 60 μm in glycerol. The microspheres were embedded in a PVA diffusion barrier and foamed in the temperature range from 80 to 100°C with otherwise identical parameters. Pre-published by the author in [69].

Surface deformations caused by foaming with diffusion barrier

As evident from Figure 4.10 the particles foamed with the diffusion barrier possess rounded pits of different sizes at their surface. One can observe here that the particles of 10 μm diameter show severe deformations (see Figure 4.10 a) and inset). These dimples might be caused by the hindered, but nevertheless occurring, escape of gas at the particle surface. Thereby, a gas void could form in the PVA diffusion barrier, deforming the currently softened particle. For the small particles these gas voids could become large enough to create the various non-spherical particle shapes observed. Figure 4.10 e) illustrates schematically how the various observed deformations could originate from the formation of a gas

void between the particle and the diffusion barrier. The size and shape of the gas void thereby determines the shape of the particle deformation. This explanation is supported by the SEM images of foamed particles shown in Figure 4.10 f). These particles were preserved in their PVA embedding after foaming and show large voids in the PVA matrix in conjunction with strongly deformed particles.

The observation of rounded surface indentations is in good agreement with other studies on supercritical CO_2 foaming with a PVA-based gas diffusion barrier [78, 119, 120]. Orsi et al. [78] described the formation of open hollows for polystyrene (PS) particles foamed in a PVA barrier film. They reported a resulting bowl shaped profile for particles with a diameter of 5 to 0.2 µm. They observed preferential void formation close to the surface and the occasional formation of open hollows along with closed inclusions within one particle. Barroso-Solares et al. utilized a PVA based diffusion barrier on solid Polycaprolactone (PCL) fibers, thereby producing hollow fibers permeated by surface pores after pressure induced foaming [119]. Cuadra-Rodriguez et al. successfully reduced the unfoamed layer of PMMA films with a PVA diffusion barrier and likewise reported a porous surface structure after foaming [120].

The observations reported in the present work indicate a transition between the formation of nanoporous inner structures combined with surface indentations (for 60-20 µm particles), towards the sole formation of the latter without a foamed core (for 10 µm particles). As CO_2 diffuses through the surface, its concentration in the surrounding matrix is depleted [70]. Therefore, it is not available for further nucleation and pore formation in close proximity [70, 72, 78]. For small particles the CO_2 concentration might be depleted by the preferential void formation close to the surface to an extend that not enough gas is left to form a foamed core [72, 78]. As the particle size decreases the surface to volume ratio becomes more and more unfavorable, which might further enhance the loss of CO_2 out of the surface. This may be hindered by the barrier film but not completely prevented.

Reflectance improvements by diffusion barrier foaming

The utilization of a diffusion barrier made of PVA clearly showed an effect on foaming. The benefit was evident for the hereby successful foaming of 20 µm particles. Therefore, the strategy of foaming particles within a barrier film is pursued further. It is to be expected that the optimal foaming parameters may vary for different particle sizes and different barrier materials such as PVA and PVP. It should be noted that a modification of the system was carried out in order to be able to foam in several autoclaves in parallel. Two additional autoclaves with associated valves were added to the system. Therefore, the following results will not be directly compared with those obtained before the modification. The
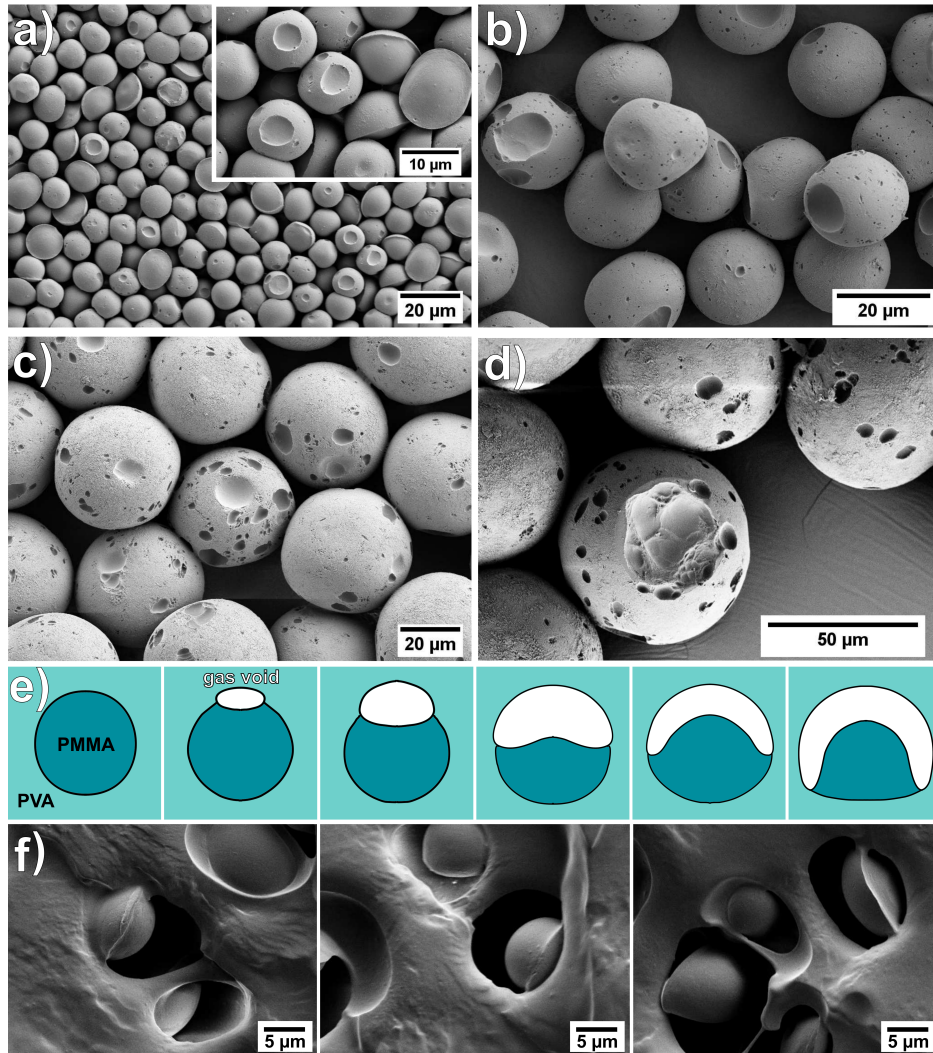
Figure 4.10: SEM micrographs of PMMA micospheres with nominal diameters of a) 10 μm, b) 20 μm, c) 40 μm and d) 60 μm showing surface deformations after foaming within a PVA diffusion barrier. e) A possible explanation for these is the formation of gas voids at the interface between microsphere and PVA barrier during the foaming process. The gas voids might be imprinted into the polymer, which is soft and deformable during foaming. The gas voids size and shape thereby determines the shape of the deformation. f) SEM micrographs of foamed 10 μm microspheres, which are still embedded in the PVA barrier film, show deformations matching the voids formed in the surrounding PVA material. Pre-published by the author in [69].

48

following experiments however were all carried out after the modification and are therefore comparable. The reflectance of 40 μm particles foamed without a diffusion barrier in the temperature range from 80 to 110°C is shown in Figure 4.11. The particles were immersed in a glycerol solution in a concentration of 1 wt%, as described previously.
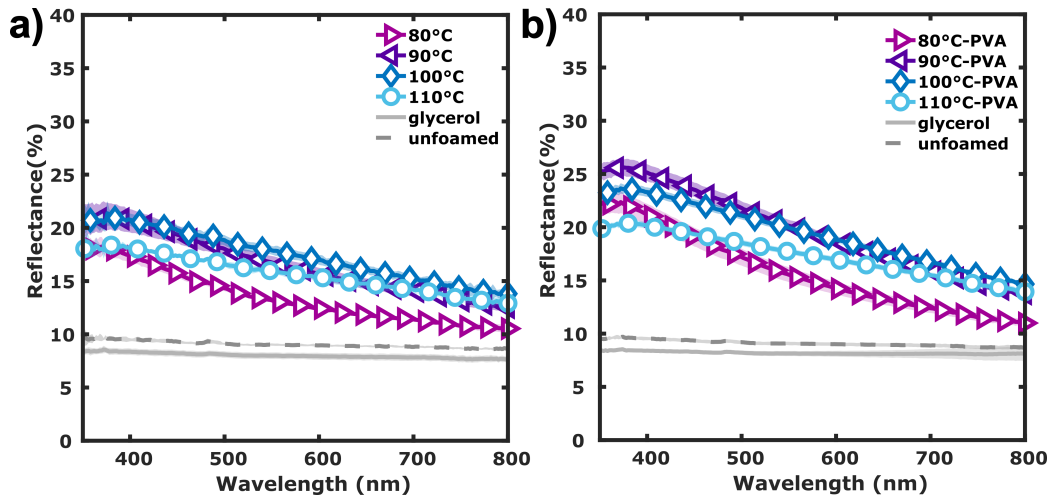
Figure 4.11: Reflectance spectra of 40 μm PMMA particles in glycerol, which were foamed a) without diffusion barrier and b) in PVA diffusion barrier in the temperature range from 80 to 110°C. Each reflectance spectrum is averaged from 4 measurements and the shaded areas indicate the respective standard deviation.

The small difference in the refractive index allows scattering effects of the particle surface to contribute to the measurement, thus including effects caused by the observed surface deformations. The reflectance of all samples is around 20% in the short wavelength range and expectedly decreases in the long wavelength range. The sample with particles foamed at 80°C shows the lowest reflectance over the whole spectrum. The particles processed at 90 and 100°C show a similar reflectance in the short wavelength range, whereas the particles foamed at 110°C reach a lower reflectance. Towards the longer wavelength range the reflectance values become more similar to each other. For 40 μm particles foamed in the same temperature range but embedded in a PVA diffusion barrier, the reflectance in the blue region of the spectrum is slightly increased and reaches between 20 and 25%. Towards the red region of the spectrum, however, it decreases to values of 10 to 15% similar to those reached by particles foamed without diffusion barrier. In the short wavelength range, the sample with particles foamed at 90°C reaches highest reflectance.

For 20 μm particles foamed in a PVA diffusion barrier in the temperature range from 80 to 110°C a much lower reflectance is achieved compared to the
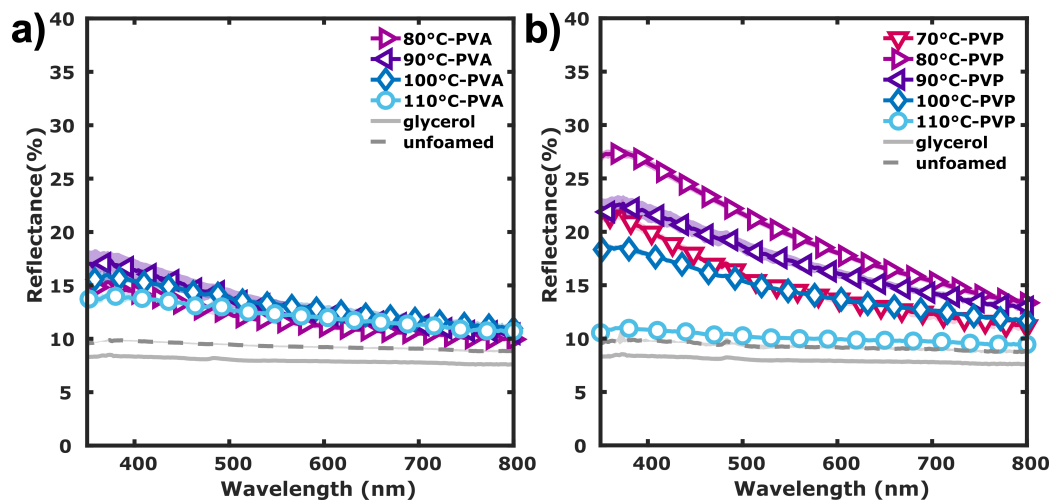
Figure 4.12: Reflectance spectra of 20 μm PMMA particles in glycerol, which were foamed in a diffusion barrier based on a) PVA and based on b) PVP in the temperaure range from 80 respectively 70 to 110°C. The shaded areas indicate the respective standard deviation of 4 measurements.

40 μm particles foamed at the same conditions, as shown in Figure 4.12 a). The spectra resemble those of the larger particles, but with a maximum reflectance of only about 15% in the short wavelength range. Towards the longer wavelength range the reflectance is only slightly higher than that of unfoamed particles. Analogously to the embedding in a PVA-based diffusion barrier 20 μm particles were embedded in PVP and foamed in the temperature range from 70 to 110°C. The corresponding reflectance spectra of the particles immersed in glycerol is shown in Figure 4.12 b). The reflectance in the short wavelength range of the spectrum is greatly increased, with the maximum achieved for a foaming temperature of 80°C. Thus the optimal temperature range is again shifted towards lower foaming temperatures. However towards longer wavelengths the reflectance decreases steeply below 15% for all samples, which is nonetheless higher than the reflectance achieved in this range with the PVA diffusion barrier. The pronounced improvement in reflectance achieved by utilizing a PVP-based diffusion barrier could be associated to the difference in the T_g of both polymers. PVA has a T_g of about 80°C [123], while PVP has a much higher T_g of about 110 to 180°C depending on the degree of polymerization [124]. It can therefore be assumed that the PVA diffusion barrier becomes deformable already at lower foaming temperatures compared to the PVP-based barrier, which thus prevents the unwanted diffusion of CO_2 more effective.

4.5.6 Thermal and mechanical stability of foamed microspheres

The stability of the pore structure under heat load is important for various applications, as some production processes require one or more heating and drying steps. The thermal destruction of the pore structure and the resulting recovery of transparency was investigated using a thermostatic heating stage. When foamed 60 μm particles were heated up to 110°C no visible change in the white color impression was observed as shown in Figure 4.13. Heated further to 115°C fading was observed and heated at 120°C the particles turned transparent. This temperature-dependent loss of opacity is an important aspect to consider when processing the foamed particles.
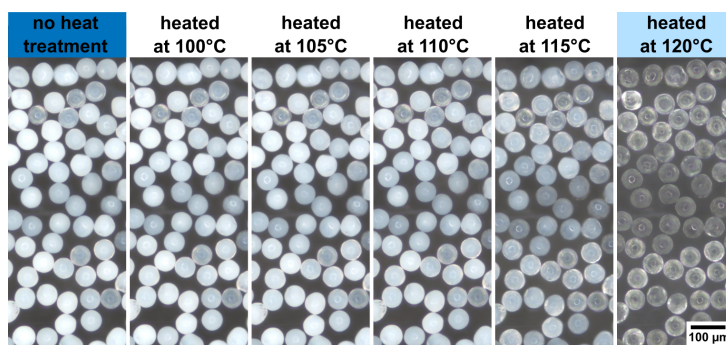
Figure 4.13: Optical micrographs of foamed particles after being heated, starting at a temperature of 100°C increasing in 5°C steps with 10 minutes heating time respectively. The white appearance of the microspheres begins to fade at about 115°C. When heated at 120°C the microspheres turn transparent again, indicating the destruction of the light-scattering nanopores. Pre-published by the author in the supplementary material to [69].

Another aspect is the mechanical stability of the foamed particles compared to their unfoamed counterparts. Based on own observation the foamed particles are mechanically stable enough to withstand manual milling in a mortar. In addition, the properties of foamed and unfoamed particles were tested using micro particle compression. A series of tests with maximum loads from 50 to 250 mN were measured in an increment of 50 mN on each type of particle. The particles were glued to a microscopy slide separately to ensure that one particle was compressed at a time. The exemplary load-displacement curve of an unfoamed and a foamed particle with the maximum load of 250 mN applied is shown in Figure 4.14 a).

Whether any fracture of the particles occured due to the loads applied was investigated by SEM. For the unfoamed particles a clear imprint of the flat punch
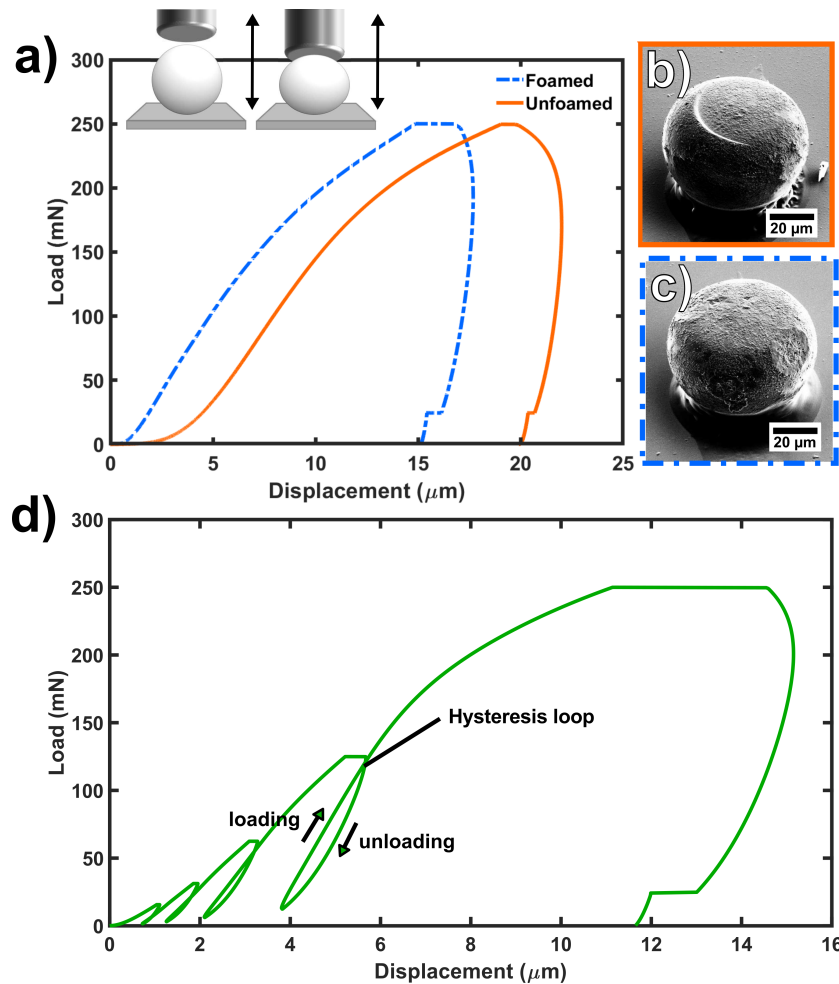
Figure 4.14: a) Representative load-displacement curves of a foamed (dash line) and an unfoamed (solid line) microsphere, which are compressed with the maximum load of 250 mN and subsequently unloaded. The corresponding SEM micrographs of the b) unfoamed and the c) foamed microsphere after the micro compression experiment show the flattening of the initially spherical shape. d) The exemplary multi-cycling loading-unloading curve of an unfoamed microsphere shows hysteresis-loops. These were observed for both, foamed and unfoamed microspheres, demonstrating their viscoelastic behavior. Panels a)-c) were prepublished by the author in [69] and panel d) was pre-published in the corresponding the supplementary material.

was observed for particles loaded with 200 and 250 mN respectively, as it is shown exemplary in Figure 4.14 b). In the case of the foamed particles, the first deformations are observed for loads of 150 mN, which get more pronounced for higher loads of 200 and 250 mN. Here, the deformation takes the form of a flattening in shape in comparison to the previous spherical particle, as shown in Figure 4.14 c). In a multi-cycling loading-unloading experiment as shown exemplary in Figure 4.14 d), hysteresis loops are found in both foamed and unfoamed particles. This demonstrates the viscoelastic behavior of both types of particles. Overall, neither was any fracture of the particles nor a loss of white color impression observed in the foamed particles due to mechanical loading.

In summary, heating at temperatures above about 115°C causes the foamed particles to lose their white color impression. Mechanical stress can deform the overall particle shape, but the white color remains. It can therefore be assumed that the particles are well suited for applications without high temperature loads and that the mechanical stability of the particles is not severely changed by foaming.

4.5.7   Practical application

The monodisperse PMMA particles used here as base material are utilized as functional additives for various paints, coatings, varnishes and lacquers to obtain super matte paints with good scratch resistance [109]. It can therefore be assumed that the particles are well suited for incorporation into various types of paints. As a proof of concept a transparent dispersion binder was used as a base for the paint formulation, used e.g. in the art sector for self-mixing of acrylic paints. Either unfoamed or foamed 60 µm particles were then added as polymeric pigments to the transparent color base. For this purpose, particles foamed at 90°C in the process variation with PVA diffusion barrier were selected, as they reached a high reflectance in the integrating sphere measurements. The paint containing the unfoamed, transparent particles produced hardly any opaque effect as shown in Figure 4.15 a) (left). The formulation with foamed particles resulted in a bright white color impression as shown in Figure 4.15 a) (right). The design was created by means of a laser cutter. The particle-based paint can also be applied by brush to a classic painting base, such as a canvas, an example of which is shown in Figure 4.15 b).

Some important aspects have to be considered for an application in paint formulations. The formation of pellets and agglomerates occurs for both presented variations of foaming. Thus the foamed particles must be mechanically converted back into a lump-free powder form. Alternatively a homogenization step could be applied to the paint formulation before use. For different color formulations, differences in refractive index may occur. Therefore the required particle con-

Figure 4.15: a) Photograph of a substrate covered with a transparent acrylic paint containing either unfoamed (left) or foamed (right) microspheres with a nominal diameter of 60 µm, both at a concentration of 20 wt %. The mixture containing unfoamed particles results in a transparent to hazy appearance, while the paint containing foamed particles shows a white, opaque coloration. b) The paint can be applied with a brush as well, as shown here on black primed canvas for example. The paint used contains unfoamed (left), foamed (middle) or in a PVA-diffusion barrier foamed microspheres (right). Pre-published by the author in [69].

centration will vary depending on the base formulation. For many paint and coating applications, the particle size is a crucial factor, as thin coatings of a few hundred micrometers or less are desired [107]. Thus typical pigments are much smaller than those presented here, which are rather in the size range of extender particles exhibiting sizes up to 50 µm [107].

4.6   Conclusion and Outlook

In the following the chapter is summarized and possible scale-up options are discussed with special consideration of the use of diffusion barriers for supercritical CO_2 foaming [c]. In this chapter, a method and favourable parameters were presented to equip cross-linked PMMA particles with light-scattering nano-pores. The successful supercritical CO_2-foaming of the particles was confirmed by optical dark field microscopy. The resulting pore properties concerning pore size and density were assessed using nano-CT. The pore sizes are in good agreement with predictions from literature for effective light scattering by air voids. Reflectance measurements of foamed particles embedded in a refractive index

---

[c]Section 4.6 has been published in similar form by the author in [69].

matching PMMA matrix demonstrated their light scattering abilities. The foaming process was further optimized by utilizing different diffusion barriers to minimize the unfoamed layer and to enable the foaming of smaller particles. The surface deformations observable after foaming with the PVA-diffusion barrier were visualized by SEM. It was concluded that particles are deformed due to the formation of gas voids at the interface of particle and diffusion barrier. In addition, it was investigated how the particles react to heating and to mechanical stress through compression. The foaming does not impair the mechanical properties of the particles, which provides important clues for their further processing. As exemplary application a paint containing foamed particles was presented. This simple color formulation created a distinct white color impression.

The presented foaming process is limited by to factors. First, it is a batch process. Consequently, the foamed volume depends on the size of the autoclave. To overcome this issue, a serial process would be needed. Here, foam extrusion with supercritical CO_2 [62] followed by subsequent grinding to the desired particle size might be an option. In this case, however, the resulting particles would vary in size and lack a skin layer. Both constraints might be a drawback for some industrial applications.

The second limiting factor is the cumbersome addition and dissolution of the diffusion barrier. Here, it might be beneficial to coat particles in large quantities with a layer of well defined thickness. In cosmetics and pharmaceuticals, tablets, pills or powdered ingredients are often coated, e.g. to control the release of active ingredients in the body, to mask unpleasant tastes or odours or to protect the embedded substance from environmental influences, to name but a few. Therefore, there are already numerous established manufacturing processes from laboratory to industrial scale for coating particles in the micrometre range [125]. The following processes represent a selection made according to the usual size range of the particles utilized, the initial state of the coating and the core material respectively (liquid and solid) and the feasibility to use aqueous solutions of the polymeric diffusion barriers examined in this work.

In spray-drying a dispersion of core particles in polymer solution is utilized, subsequent spraying into a heated chamber causes a solidification of the shell material due to solvent evaporation. Typical particle sizes range from 5-5000 µm, instead of forming core-shell particles the resulting microcapsules have a polynuclear or matrix-like morphology, whereby the core particles are prone to aggregation. Water-soluble polymers are suitable for this process offering the benefit to use water as harmless solvent [125].

Fluidized bed coating can be used for particles in the size range from 20 to 1500 µm. Fluidization occurs when a granular material is converted to a liquid-like state by pumping a liquid or gas up through the granular material. Hereby the liquid coating is sprayed from either top, or bottom (Wurster´s coater) or

tangentially on the moving particles. As the solvent evaporates a solid shell is formed, this process can be continued until the desired layer thickness is achieved [125]. The Layer-by-layer coating method is based on the self-assembly of differently charged polyelectrolytes, which are deposited in alternating layers on a substrate due to electrostatic attraction. At least two oppositely charged polyelectrolytes are required, each of which is present in aqueous solution. The process starts with an exposure phase of the polyelectrolyte, whose charge is opposite to the surface charge of the substrate. A cleaning step is followed by the exposure to the other polyelectrolyte. This alternating deposition of polyanions and polycations is repeated until the desired layer thickness is achieved, the technique is used for particles in the size range of 0.02-20 µm [125, 126].

A shortened version of this chapter was published as the article "Porous polymeric microparticles foamed with supercritical CO_2 as scattering white pigments" by Luisa Maren Borgmann, Siegbert Johnsen, Cristine Santos de Oliveira, Juliana Martins de Souza e Silva, Juan Li, Christoph Kirchlechner, Guillaume Gomard, Gabriele Wiegand and Hendrik Hölscher, Bioinspiration & Biomimetics, Volume 18, Number 2, 026011,(2023)

Chapter 5

Porous polymers for passive radiative daytime cooling

The energy demand for air conditioning is expected to increase dramatically, causing a large negative impact on the environment, if the current technical level remains unchanged [127]. Considering the environmental impact of current air-conditioning technologies it is necessary to take into account both, their indirect CO_2 emission from electricity consumption and the direct emission of highly potent greenhouse gases from leaking refrigerants. Both issues might be omitted or reduced by utilizing passive radiative daytime cooling strategies. These are based on the fact that materials with suitable optical properties in the solar as well as in the infrared part of the spectrum can achieve cooling even below ambient temperature. The partial permeability of the earth's atmosphere to certain wavelengths can be exploited to emit thermal radiation into space. In particular, porous polymers have emerged as well-suited materials for passive radiative cooling [20, 21, 22, 23, 24, 25] since they have low production costs and the possibility of large-scale fabrication [26]. Thus the suitability of porous polymers produced by means of supercritical CO_2 for passive radiative daytime cooling is evaluated in the following.

5.1 Motivation and Background

Increasing temperatures due to ongoing global warming and the thereby further intensifying phenomena of urban heat islands [128], will strongly enhance the energy demand for cooling [19, 129]. This leads to the challenging question of how we can mitigate heat and provide cooling in a sustainable way in the future. To date the air-conditioning market is estimated over 100 billion US$, with more than 140 million units sold annually and rapidly growing sales worldwide

[129]. Today the use of cooling devices such as air conditioners and electric fans accounts for about 20% of the total electricity used in buildings worldwide, equivalent to about 10% of today's global electricity consumption [127]. In 2018 the International Energy Agency (IEA) estimated that the energy demand for air-conditioning will be tripled by 2050 (see Figure 5.1), if there will be no policy action towards higher efficiency standards [127].
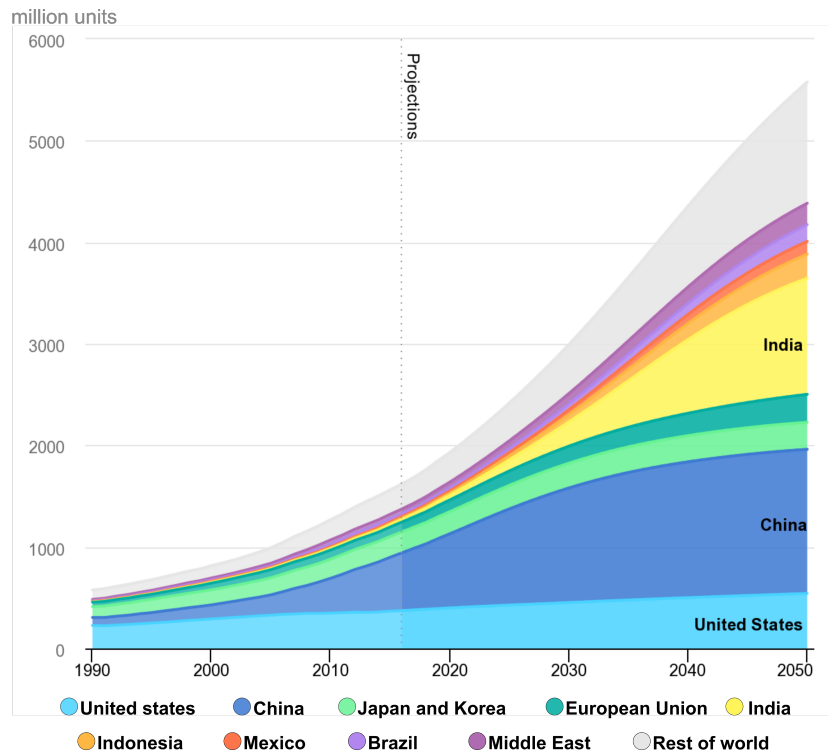
Figure 5.1: Estimation of the global air conditioner stock until 2050 by the International Energy Agency (IEA). Last updated 26 Oct 2022. Licence: CC BY 4.0 [130].

Their recommendation for mandatory energy performance standards already points out one of the main problems with today's air conditioning systems: The nowadays prevalently used technology is based on vapour compression refrigeration cycle, which has a high electricity consumption. This ironically further reinforces global warming, at least as long as the energy supply is based on greenhouse gas emitting sources. Another problem with conventional air-conditioners is the necessity of refrigerants: vapour compression air-conditioning technology is based on repeatedly evaporating and condensing refrigerants, hereby the conversion from a liquid to a gas absorbs heat, while condensing releases heat [127, 129]. The great majority of those refrigerants, e.g. hydrofluorocarbons

(HFCs) and their mixtures, have a significant global warming potential, that can be more than ten thousand-fold more potent than that of CO_2 [127, 131]. Thus the Kigali amendment to the Montreal Protocol in 2016 aims at an over 80% reduction in the HFCs consumption by 2047 [132]. Consequently, current research aims mainly on finding less environmentally harmful refrigerants, improving the energy efficiency of vapor compression systems, and developing alternative active cooling systems [129, 133]. Another scientific approach however emphasizes the development of entirely passive strategies for cooling, and thereby offers opportunities that go beyond the mere improvement of existing systems.

Especially in the context of urban heat islands, it has been recognized that energy-demanding conventional cooling systems are part of the problem and thus numerous passive mitigation and cooling strategies have been developed [128, 134]. An urban heat island refers to a metropolitan area that has a much higher temperature compared to the rural areas surrounding it, leading to a significant increase of the electricity demand for cooling purposes [19, 128, 135]. An increasingly implemented passive cooling method is the use of plants on building facades and roofs, which creates a cooling effect through evapotranspiration [134, 136]. In combination with photovoltaic systems, significant increases in efficiency through cooling can be achieved, provided that the vegetation does not shade the solar cell [136, 137]. Additional positive aspects of urban vegetation are the oxygen enrichment, the mitigation of air pollution, the increase in biodiversity, and the enhanced well-being of residents [134, 136, 138]. However, for vegetation-based mitigation strategies appropriate climatic conditions, such as sufficient precipitation, must be met. In very hot and dry regions artificially irrigating extensive urban vegetation may be too energy- and cost-intensive. These hot regions with dry air and predominantly clear skies on the other hand are highly suitable for the so-called passive radiative cooling method.

5.2 Passive radiative daytime cooling

The basic prerequisite for the concept of passive radiative cooling is the fact, that the earth's atmosphere is partially transparent to radiation, providing a so-called transparency windows through which thermal radiation from the earth can be emitted into space [139, 140]. The earth's atmosphere gaseous components, primarily N_2, O_2, CO_2 and water vapor, cause wavelength dependent absorption, scattering and emission of radiation [141]. However, for a clear sky with low humidity at best, the atmosphere is transparent in certain wavelength ranges as shown in Figure 5.2.

For passive radiative cooling the transparency window in the wavelength range of 8–13 µm is of special interest, as it matches well to the blackbody ra-
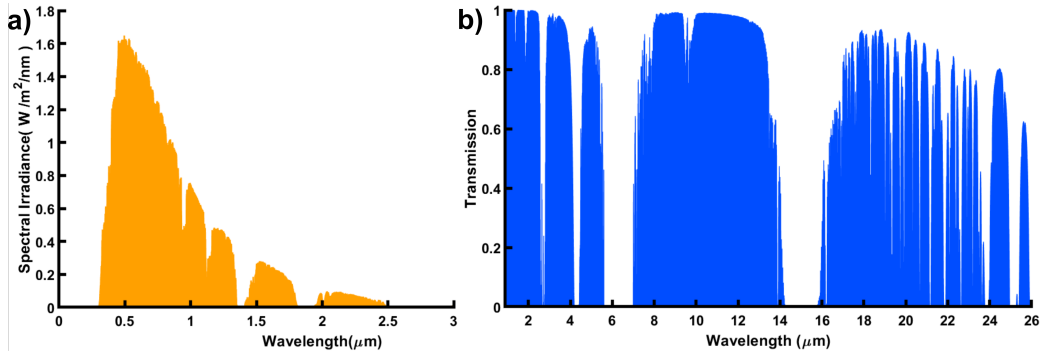
Figure 5.2: a) Reference spectrum representing the terrestrial solar spectral irradiance on a sun-facing, 37° tilted surface for an airmass of 1.5, the data was accessed from the National Renewable Energy Laboratory [142] b) The transmission spectrum of the atmosphere for an airmass of 1.5 and a water vapour column of 1 mm, the data was generated with ATRAN [143] and provided by the Gemini Observatory [144].

diation spectrum of objects on earth with a temperature of roughly 300 K [139]. Outer space with an average temperature of 3 K, thereby serves as an ideal heat sink for the emitted thermal radiation, resulting in cooling of the emitting object [139] as schematically shown in Figure 5.3. Under clear, night skies, this passive cooling effect through radiative heat transfer is readily available and has been widely used, as for example in the Persian culture to freeze water during clear nights despite ambient temperatures above the freezing point [140, 145].

Attempts to use this strategy during the daytime are hindered by the energy uptake of incoming solar radiation, an obstacle that has only been overcome in recent years [146, 147]. A device for sub-ambient daytime cooling requires to absorb as little of the solar spectrum as possible, which corresponds to a wavelength range of 0.3-2.5 μm (see Figure 5.2). At the same time it is required to emit strongly within the atmospheric window wavelength range of 8-13 μm. On closer examination, however several other factors must be taken into account [147], as summarized in Figure 5.4.

The net cooling power $P_{cool}(T)$ of a cooler with temperature T, being exposed to solar and atmospheric radiation, the latter in dependence of the ambient temperature of T_{amb}, is defined as [147]:

$$P_{cool}(T) = P_{rad}(T) - P_{atm}(T_{amb}) - P_{solar} - P_{conv+cond} \quad (5.1)$$

The temperature-dependent power radiated P_{rad} by a cooler with the area A, the temperature T and the spectral and angular emissivity $\epsilon(\lambda, \theta)$ is [147]:
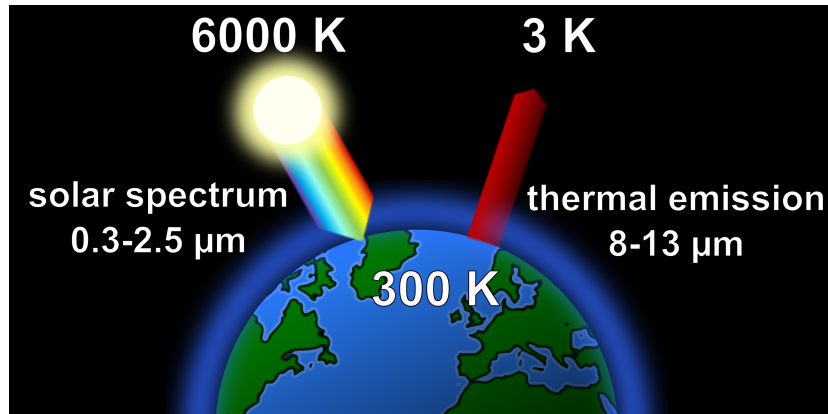
Figure 5.3: The sun surface has a temperature of about 6000 K. Its emitted radiation undergoes attenuation through the earths atmosphere, resulting in the terrestrial solar spectrum. With the incoming solar radiation absorbed and in turn outgoing thermal radiation in the infrared, the earth temperature is roughly 300 K. The partially transparent atmosphere allows thermal radiation to emit back to space, which has a temperature of about 3 K and acts as a heat sink.
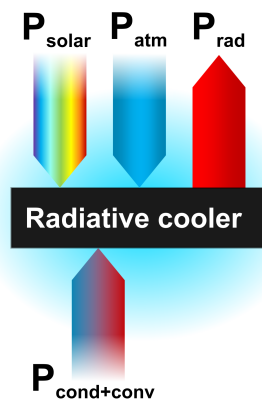
Figure 5.4: In exposure to sun and sky the net cooling power of the radiative cooler $P_{cool}(T)$ results from the power radiated by the cooler (P_{rad}) minus the power from incoming radiation from the sun (P_{solar}) and from the atmosphere (P_{atm}), as well as losses caused by conduction and convection ($P_{conv+cond}$). Daytime cooling occurs when $P_{cool}(T)$ is positive at the ambient temperature, thus when the cooler emits more heat, than it absorbs. Adapted from [148].

$$P_{\text{rad}}(T) = A \int d\Omega \, cos\theta \int_0^\infty d\lambda \, I_{\text{BB}}(T, \lambda) \, \epsilon(\lambda, \theta) \tag{5.2}$$

Hereby the angular integral over a hemisphere is given by:

$$\int d\Omega = 2\pi \int_0^{\pi/2} d\theta sin\theta \tag{5.3}$$

and the spectral radiance of a blackbody at the temperature T at a wavelength of λ is:

$$I_{\text{BB}}(T, \lambda) = \frac{2hc^2}{\lambda^5} \frac{1}{e^{\frac{hc}{\lambda k_B T}} - 1} \tag{5.4}$$

with the Planck´s constant h, the Boltzmann constant k_B and c the speed of light in vacuum.

The power absorbed by the cooler from thermal atmospheric radiation (P_{atm}) at the ambient temperature T_{amb} is given by [147]:

$$P_{\text{atm}}(T_{\text{amb}}) = A \int d\Omega \, cos\theta \int_0^\infty d\lambda \, I_{\text{BB}}(T_{\text{amb}}, \lambda) \, \epsilon(\lambda, \theta) \, \epsilon_{\text{atm}}(\lambda, \theta) \tag{5.5}$$

Thereby the angle-dependent atmospheric emissivity is:

$$\epsilon_{\text{atm}}(\lambda, \theta) = 1 - t(\lambda)^{\frac{1}{cos\theta}} \tag{5.6}$$

with $t(\lambda)$ as the atmospheric transmittance in zenith direction (vertically upward). The radiation emitted from the atmosphere to which the cooler is exposed, is present during day and night and corresponds mainly to wavelengths longer than $4\,\mu m$. The atmospheres constituents N_2 and O_2 contribute only to a minor part, while CO_2, ozone, and water vapour have major contribution to the radiation absorbed (and hence emitted) from the atmosphere [141, 26]. Thus a high water vapour content in the air is a critical factor as the increased absorption and emission decreases the transparency of the atmospheric window. In the case of an overcast sky the atmosphere becomes a near blackbody radiator with a temperature of roughly 1-2°C inhibiting radiative cooling [141]. Another important point is the direction in which the radiator emits, emission towards the zenith direction (corresponding to air mass 1.0) is the most effective, as larger zenith angles increase the path length through the atmosphere.

The incident solar power absorbed by the cooler is given by [147]:

$$P_{\text{solar}} = A \int_0^\infty d\lambda \, \epsilon(\lambda, \theta_{\text{sun}}) \, I_{\text{AM1.5}}(\lambda) \tag{5.7}$$

The solar illumination $I_{\mathrm{AM1.5}}(\lambda)$ is represented by the AM 1.5 spectrum [143, 144], as shown in Figure 5.2 and the cooler is assumed to face towards the sun at an fixed angle θ_{sun}. The attenuated solar spectrum is estimated for a given air mass to consider the atmospheric path length traveled, because the longer the light travels through the atmosphere, the greater is its attenuation.

The power lost due to non-radiative heat transfer via convection and conduction is [147]:

$$P_{\mathrm{conv+cond}} = (T, T_{\mathrm{amb}}) = A h_c (T_{\mathrm{amb}} - T) \tag{5.8}$$

whereby h_c is a combined heat coefficient to describe the undesired heating caused by the contact of the cooler to other surfaces and the surrounding air, given here as $h_c = h_{\mathrm{cond}} + h_{\mathrm{conv}}$. For the described sub-ambient temperature cooling this energy gained by non-radiative heat transfer is obstructive. Heat transferred from side and bottom surfaces facing the cooler can be suppressed by using highly insulating materials [141]. Convection can be hindered by shielding the cooler with a covering material [149, 150]. The material for such convection shield has to be highly transmitting in the infrared, especially in the atmospheric window, to allow the cooler an unobstructed emission of thermal radiation towards the space [141].

In summary, to obtain a cooling effect we need $P_{\mathrm{cool}}(T)$ to be positive, which can be achieved by a cooler that generates strong thermal radiation through the atmospheric transparency window into space, while minimizing heat gain through absorption of radiation from the sun and the atmosphere, as well as from convective or conductive heat transfer. In order to prevent heat gain by solar radiation the cooler has to be highly reflective in the solar wavelength range from 0.3 to 2.5 µm.

5.2.1 Current strategies and suitable materials

These very specific material requirements of having lowest possible heat absorption of atmospheric and solar radiation, while simultaneously emitting selectively in the atmospheric transparency wavelength range, are challenging to obtain. In 2013 Rephaeli et al. theoretically predicted the capability of a metal-dielectric photonic structure to achieve passive radiative daytime cooling [146]. The proposed structure consists of two photonic crystal layers for high thermal emissivity comprising of a quartz-based periodic square hole array on a silicon carbide (SiC) layer again on top of a broadband solar reflector [146]. This reflector in turn consists of multiple alternating layers of magnesium fluoride (MgF_2) and TiO_2 of different thicknesses deposited on a silver substrate [146]. In 2014 Raman et al. then experimentally demonstrated subambient cooling during daytime with a simplified multilayer structure of alternating silicon dioxide (SiO_2) and

hafnium dioxide (HfO_2) layers of different thickness to achieve high solar reflectance due to multilayer interference, combined with strong thermal emission [147]. These multilayers were deposited via electron beam evaporation on top of a silicon wafer previously coated with silver and an adhesion layer in between [147]. Subsequently, a large variety of other 1D and 2D photonic multilayer structures were developed, which are summarized in detail elsewhere [26, 141, 148]. Those passive radiative cooling materials based on elaborate multilayer systems or sophisticated patterned surfaces are demanding in their manufacture, the resulting high costs and the frequently limited up-scaling opportunities are therefore an obstacle for their further development.
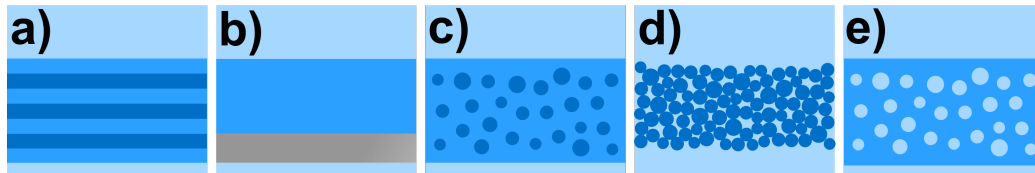
Figure 5.5: Different concepts were developed to achieve passive radiative cooling, including a) multilayer interference systems, b) infra-red emissive materials with metallic back reflectors, c) particles embedded in a material, d) systems of agglomerated particles, e) infra-red emissive materials with air-inclusions for light scattering and various combinations of the concepts.

A step towards less complex fabrication methods and new up-scaling perspectives is done by using particles, which are oftentimes embedded within a polymeric material [149, 151, 152] or in some cases are based purely on particles [153, 154]. Gentle and Smith introduced a passive radiative cooling structure based on a Polyethylen (PE) film containing spherical SiC and SiO_2 nanoparticles of approximately 50 nm diameter, attached to a smooth aluminum sheet [151]. The PE film is highly transparent within the atmospheric window, while the nanoparticles cause the high absorption and emission in the atmospheric window. The cooling performance was theoretically analysed, the focus was on cooling under nighttime conditions and the optical properties for wavelengths above 3 μm [141, 151]. Zhai et al. likewise used randomly distributed spherical SiO_2 particles, here embedded in polymethylpentene matrix, which is transparent in the solar spectrum [149]. The SiO_2 particles enhance the infrared emissivity and in order to achieve a high reflection of the solar radiation a silver coating of 200 nm was deposited on the backside [149]. Another strategy of nanoparticle based radiators is to generate the required high reflectivity of the solar spectrum likewise by nanoparticles instead of using a silver coated backside.

Bao et al. for example proposed a two-layer radiator, the upper layer of which

uses TiO_2 nanoparticles for effective reflection of visible light and the lower layer of which uses SiO_2 or SiC particles for high infrared emission [153]. It should be noted that the coating is made by spray coating of a particle-isopropyl alcohol solution on an aluminium substrate. The final coating consist of particles without a surrounding material, therefore leaving open the question of the mechanical stability against wear. Huang and Ruan introduced a similar two layer design strategy with TiO_2 particles for high solar reflectance and carbon black particles for enhanced infrared emission, here though embedded within an acrylic resin [155].

In another particle based approach from Peoples et al. only TiO_2 particle are utilized likewise embedded in an acrylic matrix [152]. Hereby mixtures of different particles sizes from 50 to 800 nm created a broadened size distribution resulting in an enhanced solar reflection compared to single particle size containing systems [152]. With these particle-based approaches, as already discussed previously for TiO_2, the energy consumption in production of these particles, emerging occupational safety and health issues, as well as the environmental impact have to be considered.

A very simple implementation of a radiative cooler was presented by Aili et al. [156]. The authors investigated the emission properties of the polymers PMMA and polyvinylidene difluoride (PVDF), which were chosen due to their functional groups whose vibrations cause the characteristic absorption and emission in the atmospheric window wavelength range. Both were found to be very suitable passive radiation cooling applications, PVDF performed slightly better due to lower absorption in the solar range and higher emission in the atmospheric window. While the high emissivity is due to the composition of the polymer itself, the necessary high solar reflectance is achieved here by a simple reflective layer of silver at the backside [156]. A product based on a similar approach is commercially available in the form of a metallized foil [157].

Ultimately, it is also possible to omit the use of multilayer systems, metallic coatings and particle-based systems altogether, which would greatly reduce material and production costs. The strategy behind is to create porous structure in a material that has a high emission in the range of 8-13 μm and whose air pores are tuned to effectively reflect solar radiation. Apart from the cost factor this strategy also has the advantage that, unlike particles, air voids do not produce additional material-dependent absorption of certain wavelengths, e.g. in the near-infrared range, which would reduce the performance of the emitter.

Porous polymers for passive radiative cooling

Different variations of this concept have recently been developed, many of which are as well made of synthetic polymers [22, 25], others use natural materials as

base material [22, 150], and some use ceramics [158, 159]. In the context of this work, purely polymer based porous structures are of particular interest. Some recent examples of porous passive radiative cooling materials, which are additionally depending on an metallic coating [160] or SiO_2 particles [161, 162] for their passive radiative cooling functionality, will therefore not be discussed in detail here.

Mandal et al. have successfully investigated the potential of porous structures for passive radiative cooling with the synthetic polymer poly(vinylidene fluoride-co-hexafluoropropene) P(VdF-HFP) [21]. The polymer exhibits a high absorption of wavelengths within the atmospheric window, while having a low absorption for radiation of the solar spectrum [21]. The light scattering voids created via a phase invasion method, are nano- and micropores, each with a broad distribution centered around 0.2 and 5.5 µm respectively [21]. Due to the porous network the material has a high reflectance of about 96% in the visible spectral range and an enhanced emittance in the long-wave-infrared of about 97% [21]. To be considered here is that the phase invasion process creates an open-pored structure, which might be prone to soiling and the accompanying reduction of solar reflectance. Additionally residues from the solvent acetone might remain within the material.

Shi et al. examined biological as well as synthetic materials, thereby focusing on the silk cocoon fibers of the comet moth *Argema mittrei*, which exhibits a reflective silvery appearance with a reflectance of 66% in the solar spectrum [22]. Combined with the high emissivity of 88% in the infrared due to the fibroin protein based silk composition, the cocoon fibres were presumed to act as a passive radiative cooling material [22]. The porous structure consists of elongated air voids propagating along the cocoon fiber, in the cross-section the void diameters are ranging from a few hundreds of nanometers into the micrometer range, while along the fiber length the voids are tens of microns long with constant diameter[22]. For further enhancement of the cooling potential of natural silk-based materials the authors altered regenerated silk from the moth *Bombyx mori* by removing the protein sericin to decrease unwanted absorption in the visible and near-infrared wavelength range [22]. Analog to the cylindrical air void structure observed in the biological role model Shi et al. fabricated fibres made of this modified silk as well as from the polymer PVDF, which possesses beneficial spectral properties for passive cooling [22]. In the utilized fiber spinning process the concentration of material and solvent controlled the pore density, a subsequent drawing process stretched the voids into an elongated shape. Due to the higher pore density obtained in the artificially created fibers compared to those of the comet moth, both the silk-based and the PVDF-based fibres showed an improved solar reflectivity of 73% and 93% respectively, as well as an enhanced thermal emissivity of 90% and 91% respectively [22].

Li et al. uses wood as a bio-based material source [150], thereby taking advantage of the porous network structure originally serving water and nutrient transportation [163]. A major component of wood is lignin, which serves the cell wall reinforcement [163]. As a furthermore highly light absorbing molecule it is currently the subject of research for application in sunscreens [164]. Li et al. therefore modified wood by chemical lignin removal and added a densification step by mechanical pressing for enhanced mechanical strength [150]. The remaining assembly of hollow cellulose fibres exhibits a white appearance with high reflectance, as well as a strong emission in the atmospheric window wavelength range with an average emissivity greater than 90% [150].

Nie et al. introduced porosity in a polydimethylsiloxane (PDMS) matrix in form of commercially available hollow, micron-sized glass bubbles, which were added to the polymer in different volume fractions up to 70% [165]. They achieved a solar reflectivity of 92% and the mid-IR emissivity of 85% [165]. However, the volume fraction of 70% glass bubbles raises the question of whether the necessary porosity can also be generated without this auxiliary material and thus more cost-effectively.

Indeed Zhao et al. likewise utilized PDMS, but rendered it porous by introducing water droplets in the PDMS precursor [166]. During the initial solidification of the emulsion the drops are trapped in the material. Upon the subsequent several days lasting curing process the water slowly evaporates causing shrinkage and finally the disappearance of the pores, while simultaneously the crosslinking of PDMS chains still takes place. Thereby, a kind of gap is formed during the crosslinking process, which is initially closed by inter-facial adhesion of the soft PDMS matrix rendering the cured material transparent. After full curing of the matrix these interactions can be overcome again by mechanical means such as stretching, scratching or wiping, thereby cavities are formed and create a porous structure. Interestingly, this procedure is reversible, the advantages of which will be discussed in detail later in this chapter. Depending on the stirring time of the initial emulsion average cavity sizes from 30 to 3 µm can be obtained. The solar reflection achieved with this structure is about 93% and in the long-wave infrared range the emission of 94% is reached [166].

Li et al. proposed the use of polyethylene oxide (PEO) nano fibres, which are non-porous [167] in contrast to the fibers with inner porous structure introduced by Shi et al. [22]. The porosity is achieved here by the random air voids forming between stacked fibers during the electrostatic spinning process [167]. The fibre diameters are broadly distributed around 800 nm and pile up to a sheet thickness of 500 µm, resulting in a high solar reflectivity of around 96% and a thermal emissivity of about 78% in the atmospheric window wavelength range [167]. Although the material can be produced in comparatively large areas, the fibrous, open-pored structure might be susceptible to soiling and thereby the successive

reduction of the reflectivity.

Wang et al. recently created a porous structure composed of PMMA with randomly distributed nanopores and an open hexagonal array of hemispherical micropores at the surface [25]. The surface micro pores were created by assembly of a SiO_2 microparticle monolayer, which was subsequently covered with a PMMA acetone dispersion containing nanosized SiO_2 particles [25]. After solvent evaporation an etching step in hydrofluoric acid removed the SiO_2 particles, resulting in a porous structure with ordered micropores of around 4.6 μm and nanopores of about 250 nm diameter. The authors report a high solar reflectance of 0.95% and a thermal emittance of 98%. However it is questionable whether the use of sacrificial SiO_2 particles, which have to be removed for creating porosity, is suitable on a large scale. In summary reaching a high reflectivity in the solar spectrum due to porosity combined with a high emissivity in the infrared range from 8-13 μm as a material property is a promising strategy for passive radiative cooling and based on previous results is expected to be easily implementable by means of supercritical CO_2 foaming.

5.3 Materials and Methods

Suitable polymeric materials discussed in the previous section, which exhibit a high emissivity in the desired wavelength range of the atmospheric window are P(VdF-HFP)[21], PVDF [22, 156], Polytetrafluoroethylene (PTFE) [160], PEO [167], PDMS [165, 166] and PMMA [156, 25]. In this study, the polymer PMMA was selected for its well-suited emission properties in the wavelength range of the atmospheric window [156], combined with its excellent CO_2 solubility and the resulting suitability for the supercritical foaming process [61]. In a first step PMMA foils with thicknesses of 120 μm and 250 μm from *Deutsches Kunststoff-Institut Darmstadt* have been chosen for supercritical CO_2 foaming and were investigated with respect to the resulting changes in their optical properties. Furthermore foils of PMMA co-extruded with PVDF were likewise tested for the suitability for supercritical CO_2 foaming and the thereby altered optical properties were investigated. The coextruded foils have been kindly provided by *Röhm GmbH* in different thicknesses and proportions of PMMA and PVDF. The type designation given by the supplier, as well as thickness and composition of the foils are summarized in Table 5.1.

The co-extruded foils are originally intended to serve as a protective layer to increase the weathering resistance for outdoor applications like polymeric facade panels, whereby the foil is laminated on top of the substrate surface [168]. According to the manufacturer PMMA hereby serves the good bonding to the substrate, while PVDF as the outermost layer provides increased chemical re-

Table 5.1: PMMA and co-extruded PMMA-PVDF foils for supercritical CO_2 foaming.

Foil type	Thickness	Composition		Abbreviation
	μm	μm		
		PMMA	PVDF	
Degalan	120	120	-	PMMA120
67E/SPA-87/1	250	250	-	PMMA250
EUROPLEX®	53	48	5	PMMA48-PVDF5
HC 99710	75	70	5	PMMA70-PVDF-5
EUROPLEX® LJ 21123/071/A	75	52	23	PMMA52-PVDF23
PLEXIGLAS®0F011	53	53	-	PMMA53

sistance and due to its low surface tension achieves an additional dirt-repellent effect [168]. For all foils, the temperature range investigated as foaming parameter starts from 40°C and is increased in 10°C increments until the films show excessive deformation or the achieved reflectance stagnates or decreases respectively. The pressure is maintained at 50 MPa, the maximum pressure of the set-up, in order to obtain an unfoamed layer as thin as possible [72]. To avoid further influencing parameters during the foaming process, the foils should be foamed as free-standing as possible. This allows diffusion of CO_2 over the entire sample surface, which greatly reduces the saturation time. However, since the film becomes deformable in the process an additional support is needed to prevent the film from collapsing. This is implemented using a simple metal frame in which the foil specimen is clamped, so that the specimen stands upright in the autoclave. The appropriate saturation time is determined experimentally at the lowest applied temperature of 40°C and analysed on the basis of the resulting reflectance of the polymer films.

5.4   Results

5.4.1   Optical properties of foamed polymers

In a first step the required saturation time is determined for the same type of PMMA foils of 120 µm and 250 µm thickness. Based on the diffusion coefficients of Nikitin et al. at 38°C and 25 MPa, a PMMA film of 250 µm thickness would have an estimated saturation time of about 1.5 min for low molecular weight

material and for high molecular weight material about 16 min. For the 120 μm thick film the estimated saturation time would reduce to less than a minute for low molecular weights and about 4 min for high molecular weights. For validation, both foils were foamed at 40°C and 50 MPa for different saturation times. The reflectance of the 120 μm foil, shown in Figure 5.6 a), remains constant for the applied saturation times, which is in good agreement with typical saturation times of a few minutes. Similarly for the 250 μm foil the reflectance does not change much, tending to slightly higher reflectance at shorter saturation times. A 30 minutes of saturation time is thus set for both foil types for the experiments on the influence of the foaming temperature.
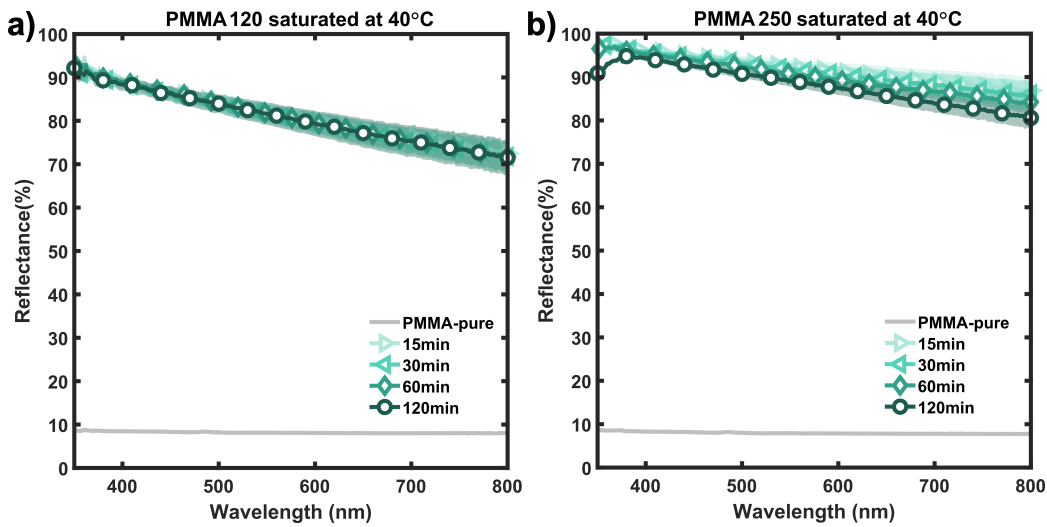
Figure 5.6: Reflectance spectra of a) 120 and b) 250 μm thick PMMA foils after different saturation times at 40°C and 50 MPa. The shaded areas indicate the respective standard deviation of 4 measurements.

The reflectance achieved for the PMMA foils of 120 and 250 μm thickness foamed in the temperature range from 40 to 90°C are shown in Figure 5.7. At 40°C foaming temperature a significant drop in reflectance from 90% to slightly above 70% can be observed for the 120 μm thick PMMA foil. From 50°C on, the spectrum shows a much less pronounced decrease in reflectance towards the long wavelength range. With raising foaming temperature, the reflectance also increases slightly. The comparatively steep decrease in reflectance for the 40°C foil can be explained by the expected smaller pore size and their ability to scatter short-wave light more strongly. The overall tendency of a decreased reflectance towards longer wavelengths observed for all samples is due to the refractive index dispersion of PMMA [39]. The 250 μm film shows a similar tendency at 40°C foaming temperature, but the decrease towards longer wavelengths is much

smaller with about 10% decrease. Here, too, only a slight decrease in reflectance towards the long wavelength range can be observed for foaming temperatures of 50°C and above. Here as well the reflectance increases slightly with higher foaming temperatures and reaches values slightly above 90% over the entire spectrum for temperatures above 70°C. When considering the results, it should be noted
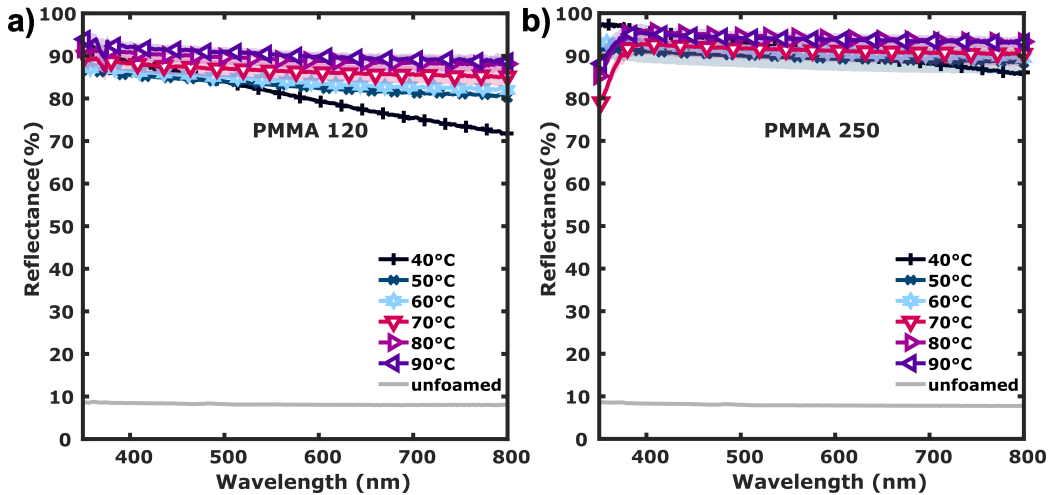
Figure 5.7: Reflectance spectra of PMMA foils of a) 120 and b) 250 µm thickness, foamed at different temperatures for 30 min at 50 MPa. The shaded areas indicate the respective standard deviation of 4 measurements.

that the PMMA films show a significant deformation when the foaming temperature exceeds 70°C, as shown in Figure 5.8. This restricts the further use of this foil type for for passive radiative cooling applications. Also, the increased brittleness of the material and the overall low mechanical stability observed is an additional exclusion criterion. The high reflectance achieved here however speaks in favor of a general suitability of the material PMMA, therefore in the following PMMA films coextruded with PVDF are investigated. The PVDF component hereby on the one hand is intended to contribute with suitable optical properties for passive radiative cooling, and on the other hand to offer mechanical support for the PMMA film. The foil PMMA-PVDF-70-5 with the largest PMMA layer of 70 µm nominal thickness is used to determine the saturation time. It should be noted that at about 70°C foaming temperature, the PMMA component starts to stick to the metal support frame and locally delaminates from the PVDF layer when detached, as shown in Figure 5.9 b). The PVDF foil stay undamaged after detachment of the PMMA component and appear translucent. The sample patches remain intact, they are slightly wrinkled at the surface, but overall flat. As shown in Figure 5.9 a), the reflectance does not change much with extended saturation times. A saturation time of 30 minutes is therefore assumed to be sufficient for
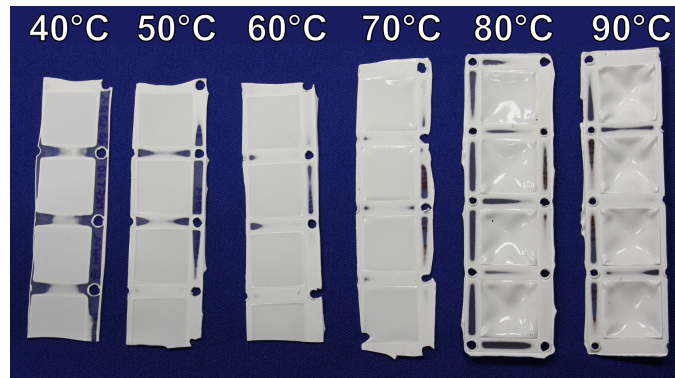
Figure 5.8: PMMA foil after foaming at different temperatures, after foaming temperatures above 70°C the foils get a deformed, curved shape instead of a flat one.
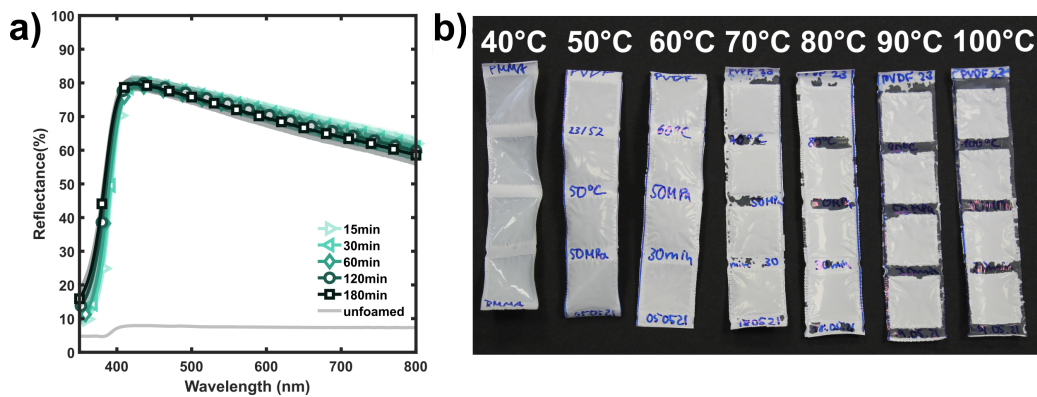
Figure 5.9: a) Reflectance spectra of co-extruded foil (PMMA-PVDF-70-5) after foaming at 40°C and 50 MPa at different saturation times. The shaded areas indicate the respective standard deviation. b) Co-extruded PMMA-PVDF foil after foaming at different temperatures, around 70°C the PMMA layer sticks to the holder and thereby delaminates from the PVDF layer.

all film types since those in comparison possess thinner PMMA layers to be saturated. The reflectance of the different film types after foaming in the temperature range from 40°C to 110°C is shown in Figures 5.10 and 5.11.
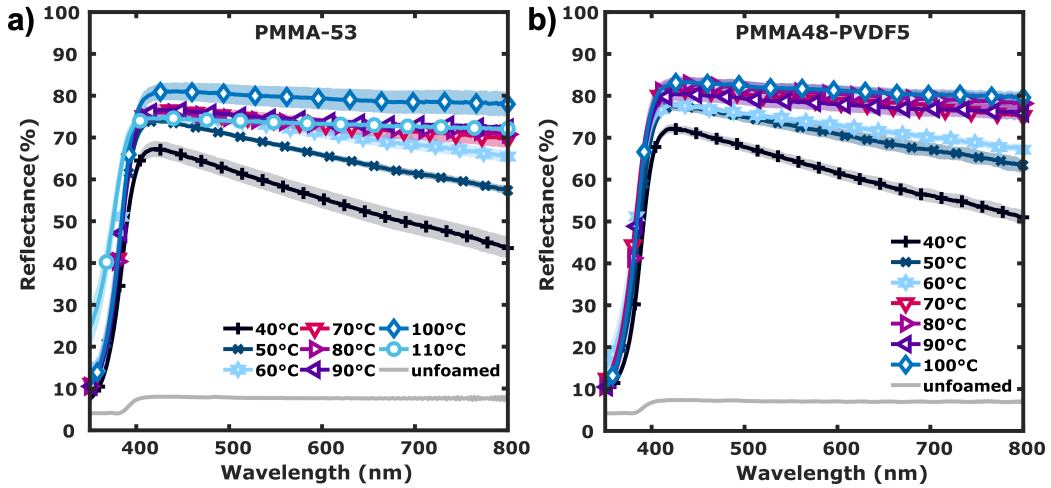
Figure 5.10: Reflectance spectra of a) PMMA-53 and b) PMMA48-PVDF5 foils after foaming at different temperatures. The shaded areas indicate the respective standard deviation of 4 measurements.

All foils show a significant decrease in reflectance for wavelengths below 400 nm, in good agreement with other spectra reported for PMMA [169]. This is due to the targeted outdoor use of the foils, which contain UV absorbing components to provide improved weatherability [168]. This is necessary as PMMA undergoes photodegradation, meaning physical and chemical changes under UV-radiation [170]. This might be a slight disadvantage for passive radiative cooling, as it enhances the energy uptake from solar radiation. Nonetheless a high weathering resistance and material durability under UV radiation exposure is as well necessary for this application, thus a trade-off between the theoretically optimal optical properties and the necessary material properties is needed. However for special applications, where a high transmission in the UV is needed, there are also PMMA materials available without UV protection [171]. For all foils, there is a clear drop in reflectance for longer wavelengths at low foaming temperatures of 40 and 50°C, an effect that becomes weaker with increasing temperature until the reflectance shows only a very slight decrease towards the long wavelength range. Again, the comparatively strong decrease in reflectance for foils foamed at low temperatures might be caused by the expected small pore sizes and the resulting efficient scattering in the short wavelength range. The transition to an approximately uniform spectrum between 40 and 70°C supports this assumption. The slight overall decrease in reflectance towards longer wavelengths
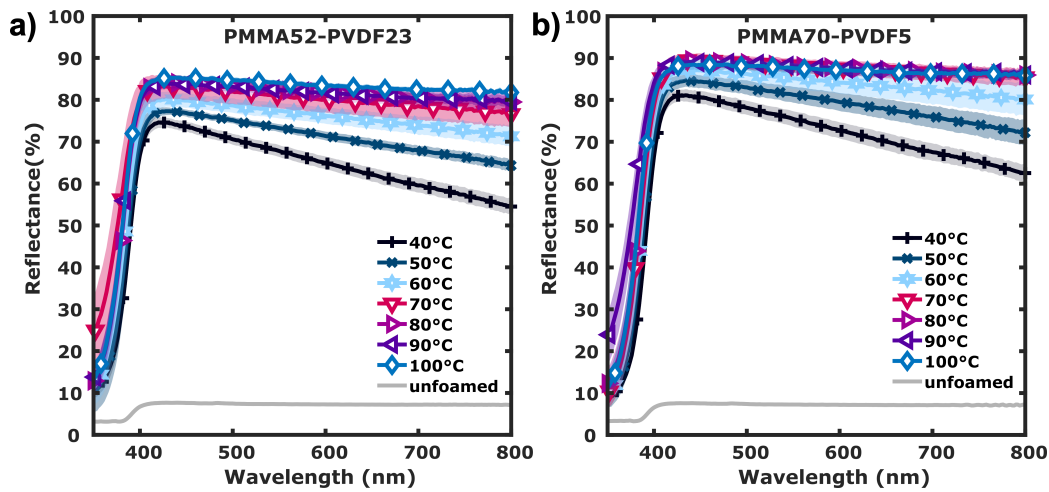
Figure 5.11: Reflectance spectra of a) PMMA52-PVDF23 and b) PMMA70-PVDF5 foils after foaming at different temperatures. The shaded areas indicate the respective standard deviation of 4 measurements.

observed for all samples is a result of the refractive index dispersion of PMMA [39] For the coextruded films, the reflectance changes only slightly above a foaming temperature of 70°C (see Figure 5.10 b) and 5.11). For the pure PMMA foil PMMA-53 (see Figure 5.10a)) there is a further improvement in reflectance observable at 100°C compared to the lower foaming temperatures. Thus a foaming temperature of 110°C was tested additionally here, but no further increase in reflectance was achieved thereby. The foils with a nominal PMMA component of 48, 52 or 53 µm thickness all reach a comparable level of reflectance of about 80%. The foil PMMA-PVDF-70-5 with the thickest nominal PMMA layer of 70 µm achieves the highest reflectance of about 85%, which is a good prerequisite for the intended use as passive radiative cooling material [152]. However, the assessments of the minimum reflection of solar radiation required for passive radiative daytime cooling ranges from >85% [152] over 88% [172] to >90% [147].

Corresponding pore sizes

The scanning electron microscopy micrographs of these foils cross-section show that the PVDF layer is not foamed, unlike the PMMA component, as shown exemplary for a foil foamed at 100°C in Figure 5.12 a). In addition, the PVDF layer is slightly thicker than expected, differing with more than 10 µm thickness from the nominal value 5 µm. The control measurement on unfoamed foils shows that this deviation in thickness is already present in the unfoamed films, and thus it is not due to foaming, as summarized in Table 5.2. The other foil types however

are very close to the nominal values stated (see Table 5.3). The temperature dependence of the pore size is illustrated by the micrographs in Figure 5.12 b)-d) showing representative pore structures obtained at 40, 70 and 100°C foaming temperature in the foil type PMMA70-PVDF5.
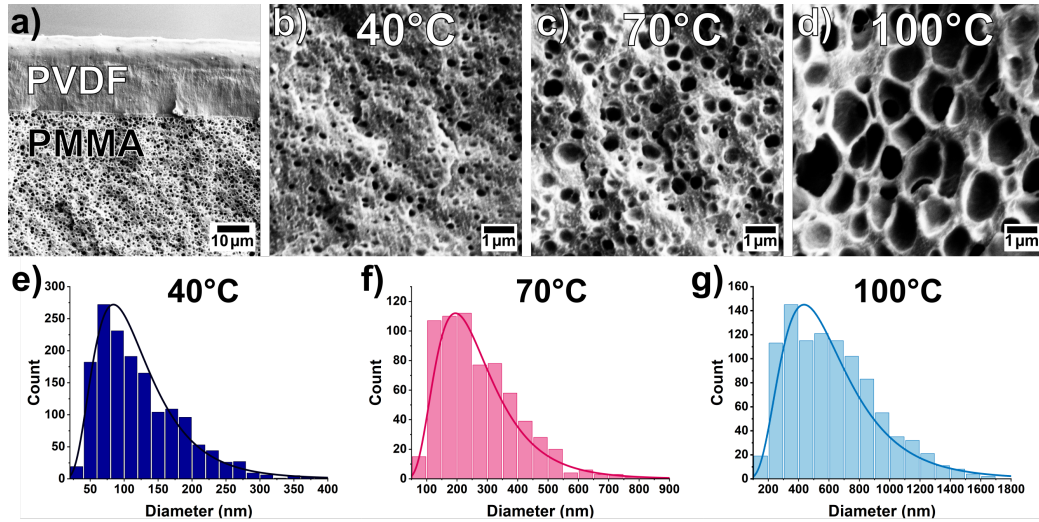
Figure 5.12: SEM micrographs of a) the cross-section of a co-extruded foil with foamed PMMA layer and unfoamed PVDF layer. Representative pore structures achieved at b) 40°C, c) 70°C and d) 100°C foaming temperature. The corresponding histograms of the pore sizes e)-g) are fitted with a log-normal distribution.

The corresponding histograms of the pore size distribution for the respective foaming temperatures are shown in Figure 5.12 e-g). As the distribution is asymmetric it is fitted here with a lognormal instead of a normal distribution, which was shown to be suitable in previous investigations of pore sizes [118]. Additionally, regarding the standard deviation of the arithmetic mean (Table 5.2), it is noticeable that subtracting three standard deviations from the arithmetic mean produces negative values, an indication for skewed distribution [173]. The probability density function of the lognormal distribution is [174]:

$$\frac{1}{x\sigma\sqrt{2\pi}}e^{\left(-\frac{(\ln(x)-\mu)^2}{2\sigma^2}\right)} \tag{5.9}$$

The median e^{μ} providing a robust estimate for lognormal distributions [173] is listed in Table 5.2 for the pore diameters obtained for different fomaing temperatures. The pore sizes of the foil foamed at 40°C are indeed small, mostly less than 200 nm, which explains the low reflectance observed in the longer wavelength range as suspected. For the foil foamed at 70°C the pore sizes are within the range one would expect for efficient light scattering [115, 116, 117] and indeed

Table 5.2: Pore diameters and average layer thickness of the foil type PMMA70-PVDF5 and its respective components estimated from SEM micrographs after foaming at different temperatures. The pore diameter is expressed with the arithmetic mean (AM) with corresponding standard deviation (SD) and for comparison with the median of the lognormal distribution.

| Temperature | Diameter | | Thickness | | |
	AM ± SD	Median	Total	PVDF	PMMA
$^\circ C$	*nm*		*µm*		
unfoamed	-	-	76.1	11.3	64.8
40	121.2 ± 61.4	107.1	93.6	12.0	81.5
70	271.8 ± 130.0	256.9	97.0	11.3	85.7
100	622.9 ± 295.2	701.1	160.4	13.8	146.7

for this sample the highest reflectance is reached at this foaming temperature. For higher foaming temperatures some pore diameters approach a size range, not corresponding to the wavelength of the incident light anymore. Since the reflectance is nevertheless high, it can be assumed that in addition to the scattering of light on the smaller pores, light is now reflected at the flat walls of the large, rather polyhedral shaped pores (see Figure 5.12 d)). The random orientation of the cell walls contributes to the non-directional reflection of the incident light and thus maintains the white color impression.

Reflectance and Transmittance of foamed polymers in the near infra red

So far all foils achieved a high reflectance in the visible range by foaming with supercritical CO_2 and the observations on the reflectance spectra are consistent with the pore sizes estimated by SEM. The so far investigated wavelength range up to 800 nm however does not take into account the optical properties in the near-infrared wavelength range (NIR), which is a component of the terrestrial solar radiation as well (see Figure 5.2). Therefore, the investigated wavelength range is extended up to 2 µm for the foils providing the high reflectance in the visible range. The reflectance and transmittance is shown in Figure 5.13 for the samples obtained with 100°C foaming temperature. In the near-infrared range, the reflectance is likewise increased due to foaming and, conversely, the transmission is reduced to the same extent for most wavelengths. The irruption observable in the reflectance and transmittance spectra between 1600 and 1800 nm indicates that the material is absorbing in this spectral range, albeit to a small extent. Other than that and the already mentioned strong absorption below 400 nm,
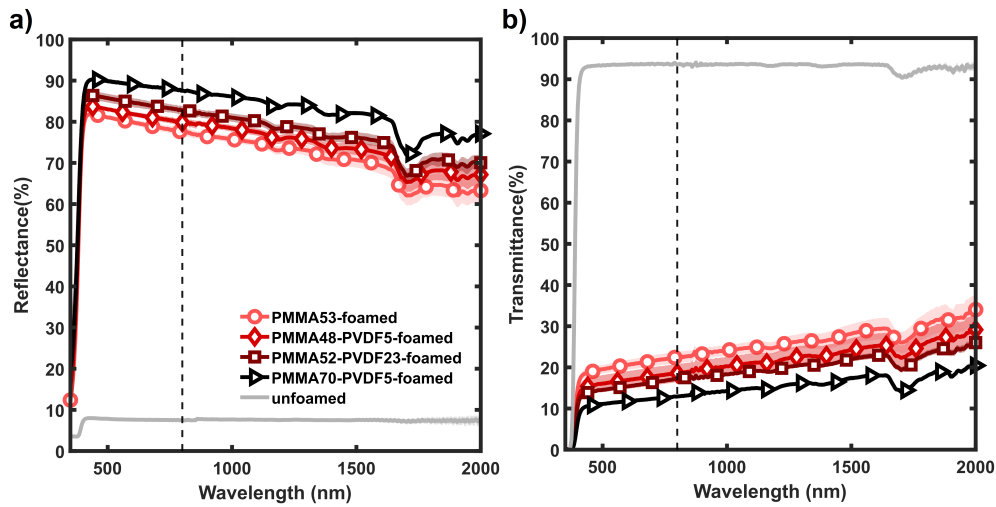
Figure 5.13: a) Reflectance spectra of different foil types, all foamed at 100°C. b) Transmittance spectra of different foil types, all foamed at 100°C. The shaded areas indicate the respective standard deviation. The dashed line indicates the end of previously measured visible wavelength range.

hardly any absorption takes place in the wavelength range investigated. The reflectance overall decreases towards longer wavelengths, in line with the trend already observed in the visible wavelength range, as also in the near infrared the refractive index of PMMA decreases further [175]. The foil with the nominal thickest PMMA layer of 70 μm and an estimated thickness of about 65 μm features the highest reflectance, as expected. The other foils have a very similar thickness compared to each other, as summarized in Table 5.3. However the magnitude of reflectance follows these small variations in thickness, the thinner the PMMA component of the foil, the lower the reflectance.

In summary, the investigated PMMA foils of 120 and 250 μm thickness tend to deform strongly at higher foaming temperatures, while the PMMA foils coextruded with PVDF are less prone to extended deformations and thereby broaden the temperature range available for foaming. Foils of greater thickness of foamable PMMA achieve higher reflectance in the visible range. Thus of the coextruded PMMA-PVDF films investigated here, the one with the nominal 70 μm thick PMMA layer is found the most suitable for passive radiative cooling. Conversely, the transmittance is also lowest for this sample, which is significant because light transmitted through the sample can be absorbed by underlying objects and would thereby result in additional heat gain in a practical implementation of a cooling setup. Therefore, a transmittance of zero would be optimal, which could be easiest achieved by increasing the layer thickness of the scatter-

Table 5.3: Average layer thickness of the PMMA foil and the co-extruded PMMA-PVDF foils and the respective component, estimated from SEM micrographs on unfoamed foil cross-sections.

	Total	nominal	PVDF	nominal	PMMA	nominal
			Thickness			
Foil type			μm			
PMMA53	51.5	53	-	-	51.5	53
PMMA48-PVDF5	57.4	53	5.2	5	52.2	48
PMMA70-PVDF-5	76.1	75	11.3	5	64.8	70
PMMA52-PVDF23	75.9	75	23.1	23	52.8	52

ing layer. Moreover the reflectance and transmittance spectra show that in the investigated spectral range hardly any absorption takes place in the material itself. Exceptions are a slight absorption in the range between 1.6 and 1.8 µm and additionally the absorption in the UV range. In the infrared more pronounced and even required absorption and thereby emission of various spectral ranges are to be expected, especially in the area of the atmospheric window. Additionally the question arises whether the differences in thickness foils and of the respective PVDF components lead to differences in the spectrum in this wavelength range. Therefore, in the following, the optical properties will be investigated in the wavelength range from 2 to 14 µm.

5.4.2 FTIR measurements

For the estimation of the emission in the wavelength range from 2 µm on and especially in the range of the atmospheric window, FTIR measurements were performed on both, foamed and unfoamed foils. Some authors assume for their estimation of the emission that the examined material is opaque in the examined wavelength range, i.e. the transmission equals 0. Under this assumption the reflectance can be used to directly deduce the emittance [21] as Kirchhoff's law states for any object at thermal equilibrium, absorptivity and emissivity are equal [176, 177]. However, the foils used here are assumed to be not perfectly opaque. Thus the transmittance is measured here in addition to the reflectance, in order to get a more realistic assessment of the emission to be expected. First of all, the unfoamed foils are to be considered to get an estimation of the changes in optical properties introduced by the foaming. As shown in Figure 5.14 the reflectance of all unfoamed foils is about 8% over the whole examined wavelength range, which is due to the reflections occurring on the smooth, plain front and
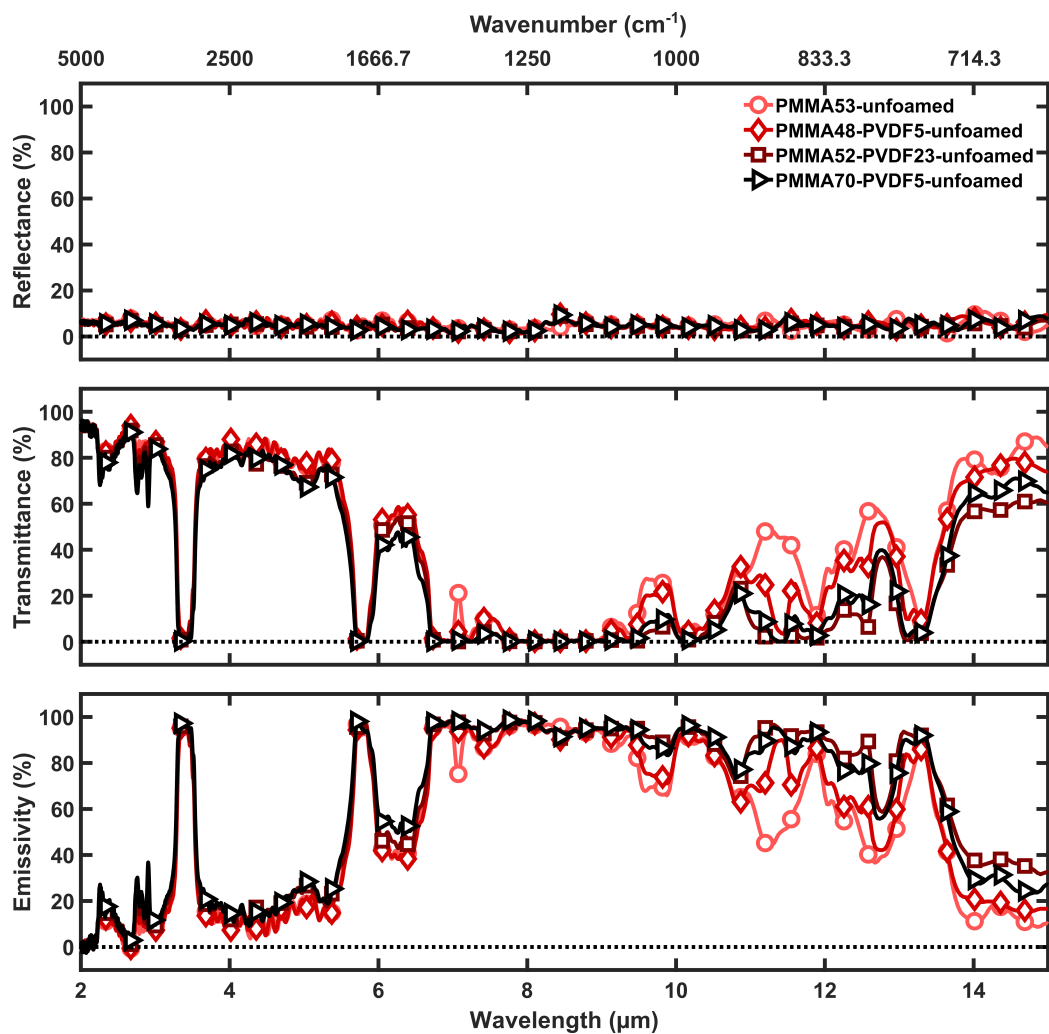
Figure 5.14: Reflectance and transmittance measured with FTIR spectroscopy for different unfoamed foils with accordingly calculated emissivity.

back surfaces of the foils. The corresponding transmittance from 2 to 14 µm is shown in the middle panel of Figure 5.14. In contrast to the most wavelengths in the visible range, were absorption was barely present, the transmittance and reflectance do not add up completely here. The parts of the incoming light that are neither reflected nor transmitted are absorbed and thus contribute to the emission of these wavelengths. The accordingly calculated emissivity of the unfoamed foils is shown in Figure 5.14 in the bottom panel. As intended, a high emissivity is reached matching the wavelength range of the atmospheric window at 8 to 13 µm. Between 5 and 6 µm there is an additional peak and a second around 3.3 -3.5 µm. A comparison with the transmission of the atmosphere (see Figure 5.2) shows that in this wavelength range there is another atmospheric transmission window, thus this additional peak in emissivity can be expected to contribute advantageously to the cooling performance.

Similarly to the observations in the visible spectrum the introduction of pores by foaming caused a modified reflectance compared to the unfoamed foils in the wavelength range from 2 to 6 µm, as shown in the upper panel of Figure 5.15. Again, the film with the thickest PMMA layer of 70 µm is the one with the highest reflectance. Overall for all foils the reflectance is roughly around 60% at 2 µm and decreases towards longer wavelengths, until from 6 µm on it is as low as for the unfoamed foils. Thus, in the range of the atmospheric window the reflectance does not change compared to the unfoamed foils and the resulting estimated emissivity is just as good. As a result of the increased reflectance modified by foaming, the transmittance is reduced accordingly (see Figure 5.15). Here too, the foil with the thickest foamable PMMA layer of 70 µm produces the highest reflectance and lowest transmittance. Since reflectance and transmittance do not add up perfectly, the calculated emissivity shows an increase in the wavelength range until 6 µm, compared to the emissivity calculated for the unfoamed foils (compare bottom panel Figure 5.15 and 5.14). For wavelengths above 6 µm however as mentioned the emissivity remains unchanged. The suitability for passive radiation cooling due to the high emission in the atmospheric window wavelength range is thus not expected to be impaired by the introduction of pores. In the range above 9 µm the thicker foils PMMA70-PVDF5 and PMMA52-PVDF23 have a higher emissivity than the thinner foils PMMA53 and PMMA48-PVDF5. The PVDF layer of the PMMA52-PVDF23 samples has an estimated thickness above 20 µm (see Table 5.3). Thus compared to the other PVDF layers it is roughly two respectively four times thicker, however this results only a slight influence on the emissivity in terms of an enhancement above 14 µm. So, in summary, foamed and unfoamed foils both show suitable emissivity in the wavelength range of the atmospheric window needed for radiative cooling applications. In the wavelength range from 2 to approx. 6 µm, the foaming of the PMMA layer increases the reflectance or respectively lowered transmittance.
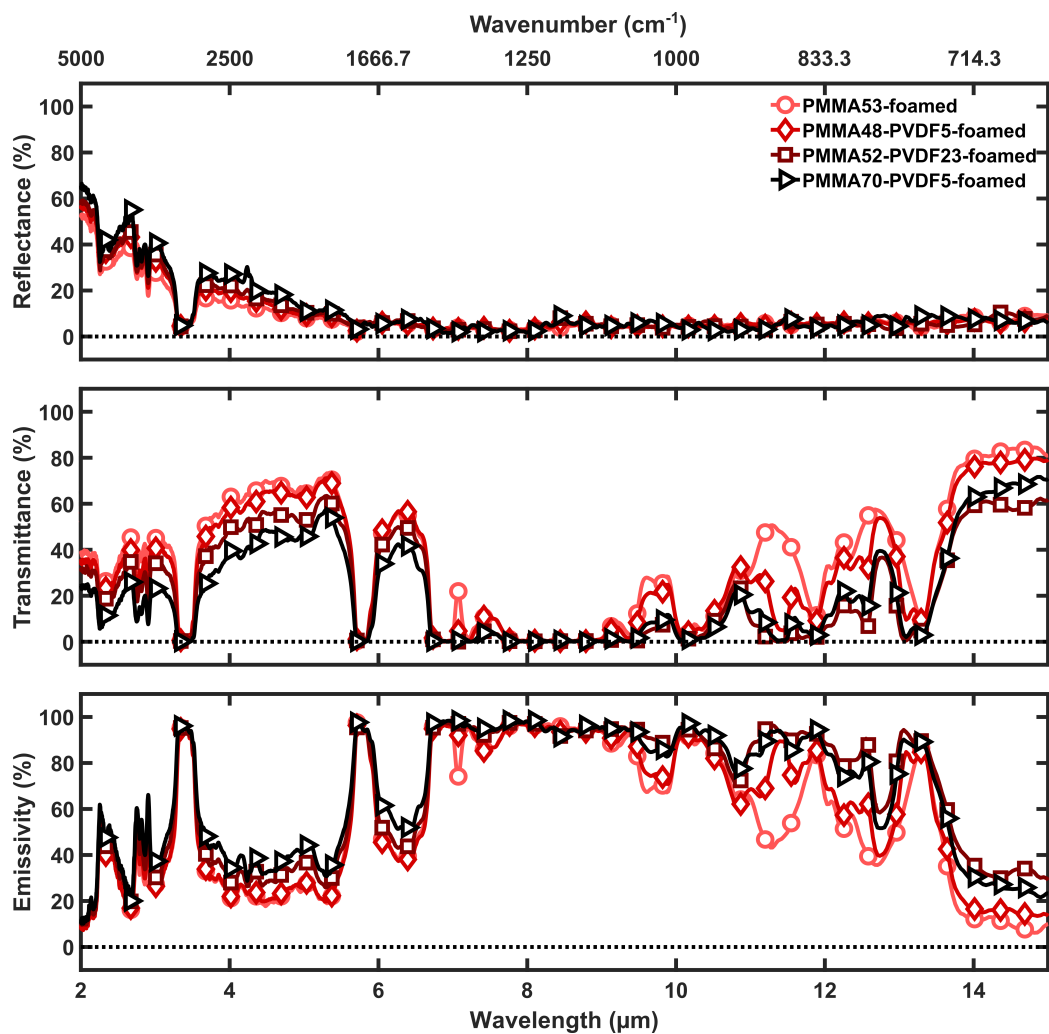
Figure 5.15: Reflectance and transmittance measured with FTIR spectroscopy for different foils foamed at 100°C with accordingly calculated emissivity.

The lower the transmittance the less light can be absorbed by structures underneath, which at least in the range of solar radiation up to 2.5 µm is desirable. A higher thickness of the foamable PMMA layer thus is advantageous.

5.5 Conclusion and Outlook

The selected foils were successfully foamed with supercritical CO_2, with temperatures above 70°C giving the best results in terms of high reflectance. The maximum average reflectance of about 87% for 400-800 nm wavelength was achieved by the foil with the highest PMMA component thickness of about 65 µm. The pore sizes are increasing with higher foaming temperatures. The results are in agreement with the corresponding reflectance spectra in the visible and near infrared. In the mid-wavelength infrared, increases in reflectance due to the introduction of pores can still be observed up to 6 µm. Beyond this, and especially in the atmospheric window region, the reflectance and transmittance and the emission properties derived from this stay the same. As a material property based on the polymers molecular composition and the thickness of the material the emissivity remains the same for foamed and unfoamed foils in this range. Due to the high emission in the atmospheric window of both foil components PMMA and PVDF and the expected suitability for outdoor applications the polymer foils were identified as particularly suitable base materials for passive radiative cooling. The necessary high reflection in the visible wavelength range was successfully achieved by introducing air cavities via supercritical CO_2 foaming.

However, passive radiative daytime cooling materials for now will not make an active air conditioning system obsolete in many cases, but could provide a supportive cooling effect to lower the demand. For a major impact addressing the increasing environmental impact, caused by enhanced demand for air conditioning, major policy actions are needed to phase-out refrigerants with high global warming potential, to ensure higher efficiency standards for air-conditioning devices and to accelerate the transition to renewable energy sources for the operation of cooling systems [127]. There has already been a very successful political intervention on former refrigerants based on hydrochlorofluorocarbons (HCFCs) and chlorofluorocarbons (CFCs), which were found responsible for the Antarctic ozone hole [178, 179]. The Montreal Protocol signed in 1987 and its enforcement's in the following years showed measurable positive effects on the ozone layer [178] and global warming mitigation [179]. It is therefore to be hoped that political actions will be taken to accelerate the development of technical improvements in the near future. A combination of new, improved active cooling systems with supporting passive cooling systems, such as urban green roofs and passive radiative cooling surfaces, could than be a promising, sustainable heat mitigation

approach. Another appealing approach is to combine the passive radiative cooling strategy with solar cell systems, where lowering the operating temperature is intended to enhance efficiency of the solar cell [180, 181].

Also with the special focus on porous polymer based radiative coolers, there are numerous promising research directions. In climatic conditions, that occasionally make heating necessary as well, e.g. in winter time, passive radiative cooling could cause higher heating costs due to unwanted cooling. In this case adaptive passive radiative cooling systems and switchable coatings can be an interesting approach [166, 182]. The main idea here is to alter the reflectance propeties in the solar wavelength range if no cooling is desired. The coating is turned from white to transparent by collapsing the pore structure or infiltrating it with a refractive index matching fluid. Heat can thus be absorbed during the day as the incident solar radiation is absorbed by a dark surface on the backside. However, one has to consider that the passive cooling effect would reoccur at night, because the high emissivity is a material property.

In a slightly different strategy utilizing porous polymers the porosity of the polymer is also responsible for high light scattering in the solar spectrum, but the polymer material itself is transparent to infrared radiation [20, 23, 24, 183]. As a result, another structure is required underneath the polymer, which is responsible for the emission of thermal radiation. This variation is particularly suitable for textile applications where the skin directly underneath acts as a thermally emitting radiator [20, 23] or for everyday objects such as canopies, sunshades or tents, which enable the person to emit excess heat in the atmospheric window [24].

Furthermore of interest may be the manipulation of the reflection properties with micro and nano-structures, which will indirectly influence the transmission and absorption properties. Depending on the size of the structures and their refractive index, the wavelength range in which this manipulation is effective can be extended from the visible [184] towards the long-wave-infrared [185]. The capability of foaming and simultaneously structuring polymers with micro- and nanostructures is discussed in more detail in the following chapter.

Chapter 6

Combined foaming and surface structuring of polymers with supercritical CO$_2$

White surfaces, especially when dedicated for outdoor applications, be it for aesthetic or functional reasons, could greatly benefit from dirt-repellent or self-cleaning surface properties. Especially for the previously introduced light scattering white foils for passive radiative daytime cooling, contamination of the surface with dust would impair the functionality by decreasing the reflectance of the white surface. A superhydrophobic, self-cleaning surface structure could prevent and limit contamination and help maintaining the functionality. Such surface structures are widespread in nature and offer an almost inexhaustible source of inspiration for a possible functional structuring of technical surfaces. Suitable functional surface structures in the micro- and nano-size range are discussed and supercritical CO$_2$ foaming is utilized to transfer these into polymers and to simultaneously create a white color impression due to the light scattering pores.

6.1   CO$_2$ assisted embossing strategies

As already highlighted in previous chapters, during the foaming process with supercritical CO$_2$ the polymer becomes soft and deformable due to the absorption of CO$_2$ under elevated pressures. This plasticizing effect already occurs at temperatures far below the usual glass transition temperature of the polymer. The plasticity of the polymer under the chosen temperature and pressure conditions is the basic prerequisite for the pores to expand after nucleation. Precisely this plasticizing effect can be used to mold a functional surface structure

into the polymer under exposure to supercritical CO_2 at low temperatures. CO_2 assisted embossing strategies utilize a reduced operation temperature than, for instance, hot embossing, where the polymer is heated over its glass transition temperature T_g [186]. Therefore, CO_2 assisted embossing is a promising low-temperature alternative especially for thermally degradable polymers [187]. Another embossing approach avoiding high temperatures is to soften the polymer with a conventional solvent. However, thereby the degree of plasticization is, if at all, challenging to control and additionally it is difficult to remove the absorbed solvent from the polymer [187]. CO_2 assisted embossing in contrast leaves no trace of solvent behind in the polymer and due to the easy detachment of the mold, additional chemical release agents can be omitted as well [187]. To exploit these advantages, several supercritical CO_2 assisted embossing strategies have been experimentally tested to date, the following overview is limited to batch processes, as this setup type is used in this study.

Wang et al. used a process in which the sample was exposed to pressurized CO_2, while a weight of $200\,g$ pressed the respective mold into the sample [187]. They structured solvent cast PMMA and PS films by using nylon fabric and anode aluminum oxide porous membranes as mold. Keeping the applied load constant they found that the imprint of the mold into the material became more pronounced with increasing CO_2 pressure, due to the enhanced plasticization of the polymer. In the study carried out by Nozaki and Oshima, PMMA and PC sheets were structured with a more sophisticated experimental setup, where stamping of the mold was performed simultaneously with depressurization of CO_2 [188]. The polymer sample is first exposed to pressurized CO_2 in an upper chamber. The subsequent pressure release into a lower chamber lifts a pedestal, which presses the metallic mold into the polymer. The applied force was controlled by manipulating pressure difference between both chamber parts. Choi et al. used a mold made of a fluoropolymer (Teflon) featuring diffraction gratings and a 2D colloidal crystal pattern as imprinting structures [189]. A spincoated PMMA sample layer was held in contact with the mold by clamps during the exposition to CO_2, which was sufficient to transfer the structural features to the sample. A PET seal film to separate a pressure chamber into an upper and a lower part was used in the study of Yang et al. [190]. The sample with a nickel mold on top was placed into the lower part for CO_2 exposition, while the pressure in both chambers was kept the same. The subsequent pressure release in the lower part, while the upper part is still pressurized, causes the PET film to press the mold into the polymer. To my best knowledge CO_2 assisted embossing approaches have not targeted an additionally foaming of the polymer so far, they even actively omitted it [188].

6.2 Biological examples of self-cleaning

White surfaces, especially when used outdoors could highly benefit from dirt repellent or self-cleaning surface characteristics, as the contamination of the white surface with dust and dirt would greatly impair the reflectance and optical appearance. A superhydrophobic, self-cleaning surface structure could hinder and limit contamination and contribute to the preservation of functionality. Such surface structures are widespread in nature and offer an almost inexhaustible source of inspiration for possible functional structuring of technical surfaces. There are numerous adverse effects to plants arising from contamination with dust particles, such as reduced photosynthesis, vegetative growth and seed set [191], thus a self- cleaning and thereby contamination limiting surface can provide a crucial advantage. The phenomenon of water repellent and self-cleaning properties of many plant surfaces in interconnection with their rough surface structure is well-known as the "lotus effect", with the leaf of the lotus plant (*Nelumbo nucifera*) as a particularly prestigious representative [192]. Dust particles accumulating on the surface of a plant can be carried away by water, but for smooth plant surfaces the particles are thereby rather redistributed. Micro- and nanostructured plant surfaces in contrast can decrease the wettability of the surface, causing the water to form droplets, which remove particles when rolling off the surface, as depicted in Figure 6.1 c) [192].
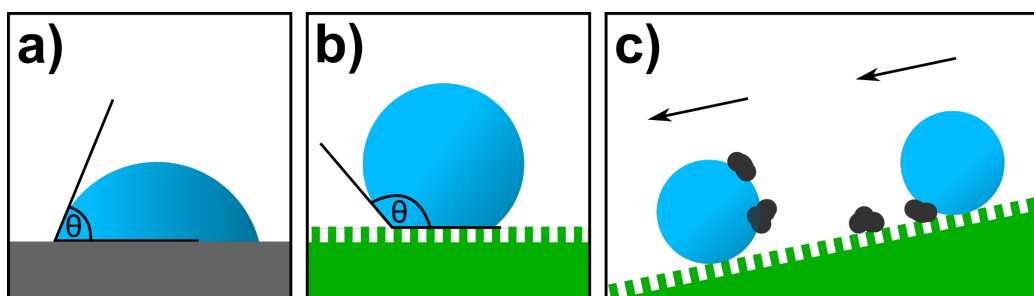
Figure 6.1: The contact angle (θ) is widely used to measure the wettability of a surface. The surface can be classified into hydrophilic for an angle with $0° \leq \theta \leq 90°$ as depicted for a smooth surface in a) or hydrophobic for $90° \leq \theta \leq 180°$ as depicted in b) for a structured surface. Large contact angles with $\theta \geq 150°$ are referred to as superhydrophobic. c) When such drops roll-off from a slightly tilted superhydrophobic surface, self-cleaning properties can be expected.

Analogous studies on insects have shown that the effect of reduced wettability and resulting self-cleaning properties can also be found in the animal kingdom. In particular, this effect has been observed in insects with long flight time and wing areas too large to be cleaned independently, e.g. for moths and but-

terflies [193]. The advantage of self-cleaning surface structures is to keep crucial body parts such as wings free of contamination and avoid the accumulation of dust and the resulting impairment of the flight [193]. The planthopper *Desudaba danae* is an in particular interesting example, exhibiting structures on its wings of very close resemblance to those found on the lotus leaf [194]. Both species inhabit a similar environment, suggesting both have to cope with similar challenges. The convergent adaptation developed by the planthopper indicates the effectiveness of this coping strategy and its structural implementation [194].

Another natural structure found on the compound eye surface of some moth species initially attracted attention because of its anti-reflection properties, known as the moth-eye effect [184, 195]. Thereby, the reduction of surface reflections is caused by nipple-like surface structures, which are smaller than the wavelength of light. These create a gradient in refractive index between the surface and the surrounding medium [195]. As many surfaces in nature tend to be multifunctional, this anti-reflection structure was also found in conjunction with superhydrophobicity and resulting self-cleaning, anti-fogging and anti-adhesive properties [195]. The nipple array covered compound eyes of the mosquito species *C. pipiens* exhibit superhydrophobic properties, which prevent the condensation of view obstructing mist droplets on the eye surface [196]. Similar anti-fogging properties emerging from superhydrophobicity have been found for the compound eye structures of the green bottle fly *Lucilia sericata* [197]. The wing surfaces of several cicada species for example are covered with similar nipple arrays, which are known to achieve anti-reflective properties [198], can influence the surface wettability towards superhydrophobicity [199] or lead to the joint appearance of both features [200, 201]. In their study on the grey cicada *Cicada orni* Dellieu et al. examined the details of this bi-functionality of the wing based on geometrical features of the surface structures [201]. It was concluded that the hemispherical top of the protrusions of this species contributes to the superhydrophobicity of the wing, while being optically not relevant. The truncated cone shape of the protrusions on the other hand was irrelevant for the observed hydrophobic behavior, while being of high significance for the anti-reflection property of the wings [201].

These biological examples of superhydrophobicity and self-cleaning offer a great inspiration for micro- and nano-scaled functional structures to be imprinted during the supercritical CO_2 foaming process. By combining the foaming of initially transparent polymers with simultaneous surface structuring the production of pigment-free white polymers with bio-inspired functional surface structures tuned towards self-cleaning properties is targeted.

6.3 Materials and Methods

6.3.1 Foaming setup

For the combination of the foaming process with imprinting of structures the setup was extended with structured molds, that are pressed into the polymer during the foaming process. As rather uncomplicated extensions of a batch process setup a weight on top of the mold with a polymer sample underneath can be used [187] or clamps to keep mold and sample in close contact [189]. In this study, neodymium magnets (*Type NdFeB N45*) of different strengths purchased from *EarthMag GmbH* were utilized to press the mold onto polymer samples. The nominal adhesive strength specified by the manufacturer were 5 and 8.5 kg. The sample and mold are clamped in between the magnets during the foaming procedure to assure a close contact of sample and mold. Thereby magnet and mold simultaneously act as a diffusion barrier. This limits the diffusion of CO_2 into the sample to occur from the sides only. Thus in a variation of the setup a metallic wire mesh was used as placeholder between sample and magnet to allow facilitated CO_2 diffusion from the bottom of the sheet, as depicted in Fig 6.2.

Wang et al. observed that increasing the CO_2 pressure leads to an enhanced imprint of the mold into the polymer [187]. Therefore, the highest possible pressure of 50 MPa was applied in this study. The exposure time was 30 min and the foaming temperatures were 40, 60 and 80°C. The latter temperature was the magnets maximum operating temperature specified by the manufacturer.

6.3.2 Molds and polymer materials

For imprinting metallic molds were utilized, since polymeric molds might interact with the CO_2 and ceramic molds might break under the strong temperature changes during pressure release. The nickel mold *Type HT-AR-02XS* from *temicon GmbH* is an imprint mold for polymers to reduce the reflectivity to below 0.2% for normal angle of incidence [202]. The purchased mold of this type had an active area of 20x20 mm with structures arranged in a hexagonal array. The nominal average depth (vertical distance from peak to adjacent valley) is >350 nm and the nominal peak-to-peak distance is 290 nm. A copy of the mold was fabricated for customization to the autoclave dimensions. The original nano-pattern was transfered to PMMA by means of hot embossing, with an embossing temperature and pressure of 155°C and 30 kN, respectively. The PMMA negative of the mold was subsequently electroplated with nickel resulting in a positive copy of the original mold. The current density was increased stepwise with 0.1, 0.25, 0.5 and 1.0 A/dm^2 applied for exposure times of 60, 66, 2 and 24 hours, respectively. The final copy features an average stucture depth of about 310 nm.
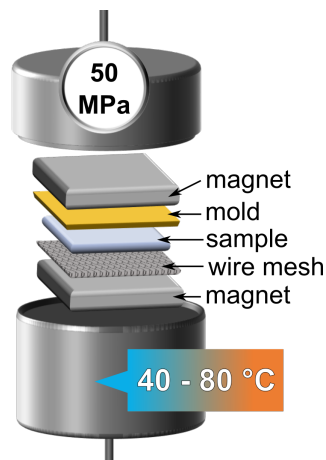
Figure 6.2: In the setup for supercritical CO_2 foaming and simultaneous patterning the sample is placed between the mold and a diffusion promoting metal wire mesh and clamped together with two neodym magnets. With the wire mesh the diffusion of CO_2 into the sample is facilitated, without it the magnets act as diffusion barrier and hinder the uptake of CO_2.

A shim featuring micro-scaled structures was kindly provided by Dr. Benedikt Bläsi from the Fraunhofer Institute for Solar Energy Systems ISE in Freiburg, Germany. The microbumps have a square arrangement and feature an average peak-to-peak distance of about 3.22 µm and an average depth of about 2.42 µm. A surface height map of both mold structures based on AFM measurements is shown in Figure 6.5 a) and b). As sample material PMMA from *UPAG*, with a nominal sheet thickness of 1 mm was used and trimmed to squares of 1.5 x 1.5 cm^2.

6.3.3 Analytical methods

Microscopy

For the assessment of the surface and the porous inner structure, optical as well as scanning electron microscopy (SEM) examinations were carried out. For this purpose, the *Axioscope 5/7/Vario* and the *Zeiss SUPRA 60 VP* was utilized, respectively. The image processing package *Fiji* was used for the evaluation of the micrographs [55]. Based on SEM micrographs the cell density N_0 in different sections of the samples was calculated as [81]:

$$N_0 = \frac{N_f}{1 - V_f} \qquad (6.1)$$

Here N_f is the number of pores per μm^3 of foamed polymer calculated by $N_f = \left(\frac{n}{A}\right)^{\frac{3}{2}}$ with n as the number of pores in the area A (μm^2) occupied by pores. V_f is the volume occupied by the pores per μm^3, estimated by [81]:

$$V_f = \frac{\pi}{6}D^3 \times N_f \tag{6.2}$$

with the average pore diameter D and assuming spherical pores.

Surface topography and optical characteristics

The surface height profiles of the embossed micro- and nano-structures and the associated molds were examined by means of atomic force microscopy (AFM). The measurements have been performed with *All-in-One* cantilevers from *Budget Sensors* and the *Dimension Icon®* from *Bruker*. The software *Gwyddion* [57] was used for the evaluation of the surface height maps. To estimate the influence of the imprinted structures on the wettability of the surface, the contact angle meter *Dataphysics OCA 40 micro* was used for static contact angle measurements. The automatic dispenser was set to a liquid dosing of $1\,\mu L$ droplet volume and a dosing rate of $1\,\mu L/s$. The optical properties of the samples were examined via reflectance measurements by means of a UV-Vis-NIR Spectrophotometer *Perkin Elmer Lambda 950* equipped with an integrating sphere. All measurements were normalized with a diffuse reflectance standard *Spectralon®* from *Labsphere*.

6.4   Results

6.4.1   Incomplete saturation avoids surface deformations

Initial tests showed that foaming with a mold pressed on the surface leads to severe deformations on the surface of the imprinted polymer, as shown exemplary in Figure 6.3. This is in good agreement to the observations in Chapter 4, where the use of a diffusion barrier led to the imprint of gas voids on the surface. As a strategy to structure and foam simultaneously an incomplete saturation of the polymer was targeted. That means the polymer is foamed after an exposure time insufficient to saturate the polymer completely throughout the thickness of the material. Based on the diffusion coefficients from literature for CO_2 and PMMA at 38°C and 25 MPa [80], a PMMA sheet of 1 mm thickness with unhindered diffusion would have an estimated saturation time of about 25 to about 260 min depending on the molecular weight. Here however the molecular weight of the material is unknown, thus the shortest saturation time is assumed. Additionally, the saturation time is prolonged as diffusion only takes place from the sides of
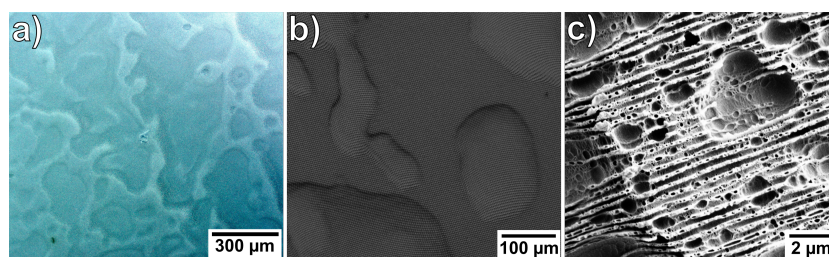
Figure 6.3: Examples of macro- and microscopic deformed surface structures obtained by simultaneous supercritical CO_2 foaming and structuring. a) Optical and b) SEM micrographs of microstructured surfaces with large deformations. c) SEM micrograph of imprinted diffraction grating with micro-scale surface deformations.

the polymer, or, for the wire mesh configuration, additionally from the bottom. Thus an exposure time of 30 min was estimated to ensure an incomplete CO_2 uptake throughout the sample in both foaming variations. Samples clamped between magnets without a wire mesh (hindered diffusion) stayed transparent after foaming at different temperatures, as shown on the left of Figure 6.4 a). Only a foamed, white edge indicates the diffusion taking place from the sides. The noticeable extension of the edge with increasing foaming temperature is due to the faster diffusion at higher temperatures [80, 81]. The colorful pattern observable by the naked eye already indicates the successful transfer of structures, which act as a diffraction grating.

Samples foamed with a wire mesh on the bottom side (facilitated diffusion) are overall white in appearance after foaming under the same conditions, as shown on the right of Figure 6.4 a). The corresponding cross-sections of the white samples in Figure 6.4 b), show a transparent layer at the side of the mold. Towards the wire mesh side a white, foamed layer is created, which increases in thickness with foaming temperature. For samples foamed at 40, 60 and 80°C the foamed layer is about 400, 1000 and 1400 µm thick, respectively. At higher foaming temperatures the diffusion coefficient increases [80, 81], thus CO_2 can diffuse deeper into the polymer. Additionally, the pore sizes are expected to increase with rising temperature [68], thus further contributing to the extend of the foamed layer. From the optical micrographs it can be concluded that the formation of pores near the surface, to be structured, was avoided by incomplete saturation for the applied foaming conditions.
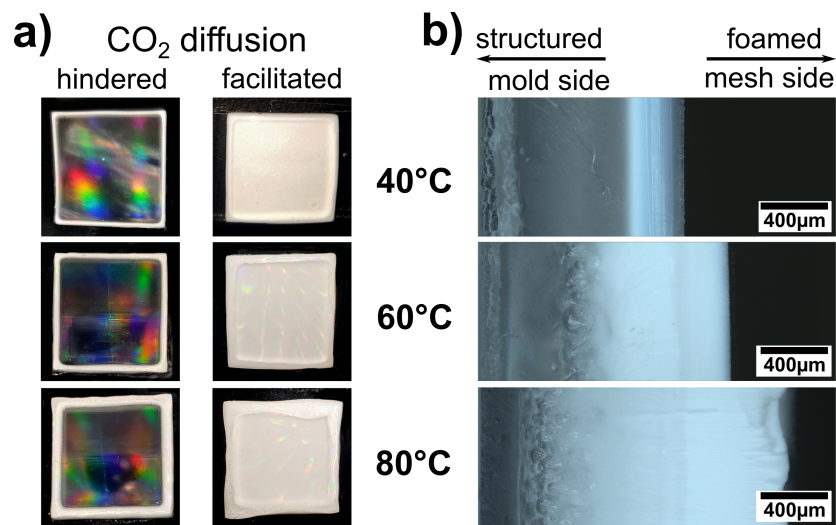
Figure 6.4: a) Photographs of samples foamed at different temperatures with either hindered or facilitated, one-sided diffusion. The former are transparent and show colorful diffraction patterns indicating a structure transfer and the latter are white in appearance. b) Optical micrographs of the cross-section corresponding to the white, foamed samples. The thickness of the foamed layer increases with increasing foaming temperature.

6.4.2 Analysis of the surface structure

AFM measurements were performed in order to evaluate the successful transfer of the structures and to estimate the effect of different foaming temperatures and magnet strengths. Figure 6.5 shows the surface height maps of the micro- and nano-structured molds along with corresponding representative replicas in PMMA. The height of the structure obtained at different foaming parameters is considered in terms of the vertical distance between peak and adjacent valley of the structure. The results of the height measurements are shown in Figure 6.6 for micro- and nano-structured samples, produced at different foaming temperatures, with different nominal magnet strengths applied and in different diffusion configurations. The height was determined from multiple height profiles measured at two to three different locations on each sample. The corresponding mold was measured analogously and is shown for comparison. The achieved heights of the microstructured replicas correspond quite well to the structure height of the mold. There is no obvious trend in terms of foaming temperature, facilitated or reduced diffusion, or the use of magnets of different strengths. The nanostructured replicas approach the height of the mold, too. Compared to each other the nanostructured samples show similar values of heights for the different process parameters and configurations. Overall, the molding of the micro- as well as of
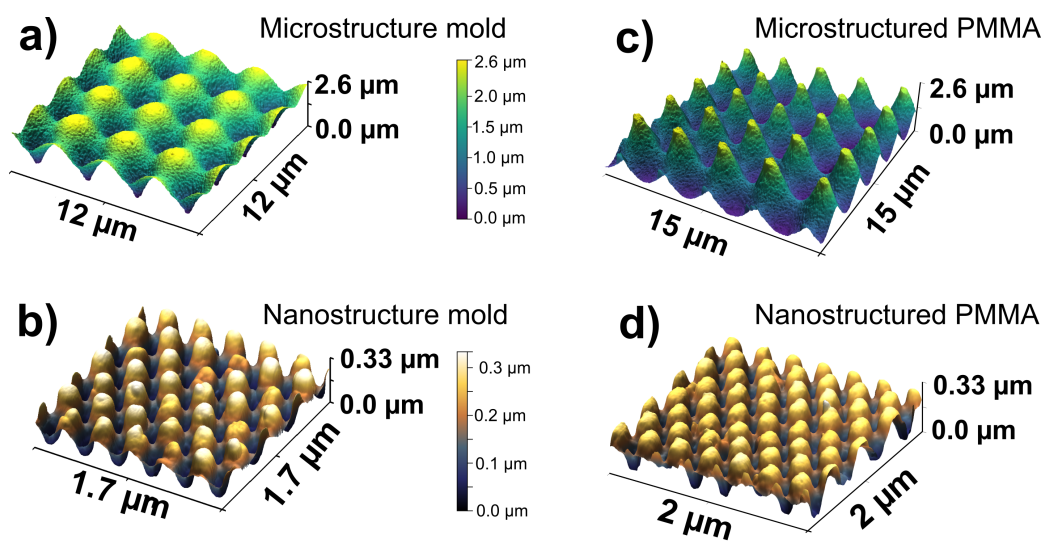
Figure 6.5: Surface height maps extracted from AFM measurements on the a) micro- and b) nanostructured molds utilizied. The surface height maps of the positive replica is shown for representative PMMA samples with c) micro- and d) nanostructured surface. Both samples were foamed at 60°C, clamped between magnets of 8.5 kg nominal strength in the diffusion facilitating wire mesh configuration.

nano-structures can be considered as successful for transparent (hindered diffusion) and for foamed, white samples (facilitated diffusion) for the investigated process parameters. The results indicate that also the difference in the pressure
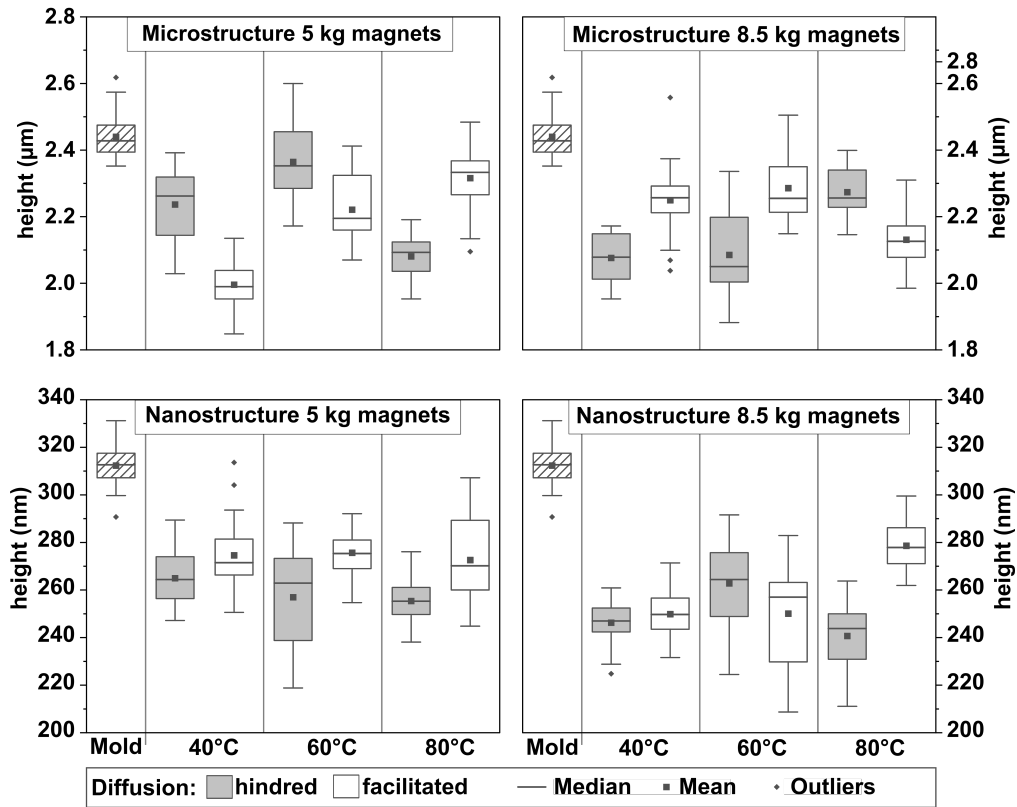
Figure 6.6: Comparison in height of micro- and nanostructured samples processed at 40, 60 and 80°C foaming temperature in different foaming configurations and with nominal magnet strengths of 5 and 8.5 kg applied. The height of the respective sample and the utilized mold was determined by multiple profile measurements at three points on the sample.

applied here by means of magnets of different strength does not influence the height of the replica structures significantly, neither for micro- nor for nanostructuring. It is possible that much lower contact pressures are sufficient, as e.g. in the experimental setup of Wang et al. only a weight block of 200 g was used to apply pressure on the mold [187]. This was sufficient for the imprinting of structures in the micro and nanometer range into PMMA, even at a temperature of only 35°C and pressures of 4 to 19 MPa applied. However, the different magnets may have an influence on pore size and density, which will be discussed later.

The differences in the heights achieved can be influenced by factors other than the process parameters. For example, the detachment of the mold from the sample is a critical point at which the structures could be inadvertently deformed. That the replicas in both cases do not completely reproduce the height of the molds may be due to the fact that the material undergoes swelling and subsequent shrinkage in the process. The absorption of CO_2 causes the polymer to swell and become deformable, thus it is pressed into the mold in a swollen state. After the pressure drop, the CO_2 is released to the surrounding and the polymer shrinks again. After successful imprinting of structures, it has to be clarified, if structuring results in noticeable changes in terms of surface functionalization. In order to determine whether a water-repellent or even self-cleaning surface could be created with the molded micro- or nanostructures, the surface was analyzed by means of contact angle measurements.

6.4.3   Contact angle measurements

The contact angle (θ) is commonly utilized to estimate the wettability of a surface. Hereby water is often assumed to be the wetting medium, especially in the context of self-cleaning properties. In this case the angle θ between the solid and liquid surfaces can be classified into hydrophilic for $0° \leq \theta \leq 90°$ or hydrophobic for $90° \leq \theta \leq 180°$ [203]. When large contact angles with $\theta \geq 150°$ are achieved this is referred to as superhydrophobic [203]. To evaluate the change expected due to the introduced micro- or nano-scale structure, multiple static contact angle measurements were performed on different spots on structured samples. For reference a non-processed, flat PMMA sample was measured, too. In Figure 6.7 the average static contact angles measured for micro- and nanostructured samples are shown. Structures produced with the same process parameters and magnet strengths, differing only in the diffusion management (facilitated or hindered), were evaluated together. Compared to the unstructured, flat reference material, a significant increase in the contact angle is achieved by structuring in the micro- as well as the nanosize range. The measurement results are in the range of 100 to 135°, whereby the whiskers represent the maximum and minimum value achieved by the respective samples. Again, the strength of the applied magnets does not produce a clear trend. On average, the nanostructures achieve a slightly higher contact angle, while on the other hand the highest contact angle was measured on a microstructure. With an average contact angle of around 80°, the smooth, untreated PMMA surface is classified as hydrophilic. After molding surface structures in the mirco- and nanosize range, the region classified as hydrophobic is reached. According to the model developed by Wenzel [204] the introduction of roughness should result in the increase of the contact angle for an initially hydrophobic surface and in turn to its de-
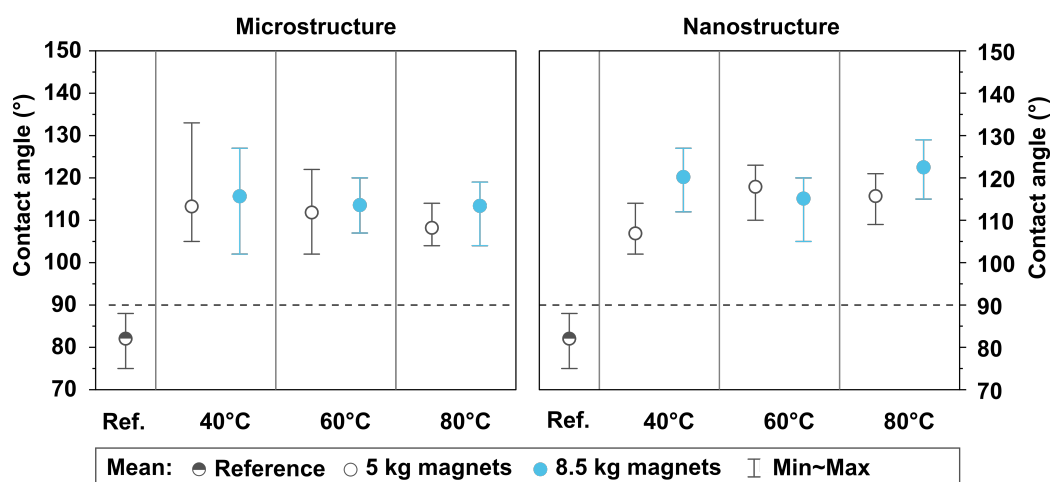
Figure 6.7: Comparison of average static contact angles of micro- and nanostructured samples processed at 40, 60 and 80°C foaming temperature with nominal magnet strengths of 5 and 8.5 kg applied. The whiskers indicate the maximum and minimum static contact angles achieved. The dashed line marks the transition between surfaces being classified as hydrophobic or hydrophilic, the upper limit of the scale represents the border to the classification as superhydrophobic.

crease for an initially hydrophilic surface. The presented outcome is however comparable to the observation of Fritz et al., achieving a static contact angle of 121.0 ± 6.0 on patterned PMMA, whereby the flat PMMA exhibits a contact angle of 72.2 ± 2.0 [205]. Ma et al. reported to achieve superhydrophobic surfaces based on hydrophilic PMMA [206]. This is reached by a combination of micro- to nanoscale surface porosity and the reorientation of the hydrophobic and hydrophilic groups in the polymer chains. The authors attribute this reorientation to the treatment in heated cyclohexane during the utilized phase-separation process. The self-adapted reorientation of the polymer chains is favoured as it lowers its surface free energy [206]. Further examples of hydrophilic polymers, such as polyethylene glycol (PEG) and PVA, exhibiting hydrophobicity after patterning are reported in literature [207].

In summary the static contact angle was enhanced for both types of surface structures imprinted, resulting in hydrophobic, but not superhydrophobic surfaces. Thus, no self-cleaning property was achieved and water drops dispensed on the structures are not able to roll off at low tilting angles, which is essential for wet self-cleaning [192]. Some general prerequisites for superhydrophobic surfaces are a high aspect ratio of the surface structures, which should be small compared to the typical droplet size [208]. Also the structures should be tightly packed and sharp edges should be avoided [208]. In the case of hydrophilic sur-

face a hydrophobic coating is needed [208]. Thus, as a straight-forward approach to enhance the contact angle further the structured samples could be coated with a hydrophobic film [208] or otherwise treated [206] to reduce the surface energy. For the improvement of the microstructure mold utilized here, the conical pillars could be packed in a hexagonal instead of a square pattern, to achieve higher packing density. A hierarchical composition with several scale sizes from micro- to nanometer range are advised for optimization [203], as similarly observed in biological superhydrophobic surfaces. However, hierarchical structured molds are very challenging to manufacture as well as to emboss and were therefore considered behind the scope of this study.

6.4.4 Reflectance

Supercritical CO_2 foaming with facilitated diffusion in the wire mesh configuration rendered all samples white to the naked eye. However the samples might differ in terms of effectiveness, thus reflectance measurements were performed. The magnet strength applied did not influence the reflectance, reaching similar values for nominal magnet strengths of 5 and 8.5 kg applied on micro- as well as on nanostructured samples, as shown in Figure 6.8 a) and b). Micro and nanostructured samples both are very similar in reflectance and comparable to smooth reference samples, foamed with a glass slide instead of a mold, as shown in Figure 6.8 c). The similar reflectance values achieved suggests that the surface structuring does not impair the desired high reflectance for the white samples.

However, the nano-structured mold is originally intended to achieve surfaces with reduced reflections, even though it is utilized here to modify the surface wetting properties. Indeed the anti-reflection effect induced by the nano-structure is noticeable for transparent samples created with the hindered diffusion configuration, as shown in Figure 6.8 d). Here the reflectance measured is determined by surface reflections only, which are minimized by the moth-eye-effect of the nanostructure. However, the reduction of the surface reflection is apparently negligible for the highly scatting white samples, here the main factor influencing the reflectance appears to be the foaming temperature. For all samples foamed in the wire-mesh configuration (Fig.6.8 a)-c)), the reflectance is lowest at 40°C foaming temperature and additionally decreases strongly towards longer wavelength range. This could be due to a smaller pore size expected at lower foaming temperatures and the overall lower thickness of the foamed layer (about 400 µm). At 60 and 80°C foaming temperature, however, a reflectance of about 100% is achieved in the visible spectrum of light, which means that the sample reflects as well as the white reference standard in this range. The low reflectance of all samples observable for the short wavelength range can be associated with the UV-absorbing properties of PMMA reported in literature [169]. Since the optical
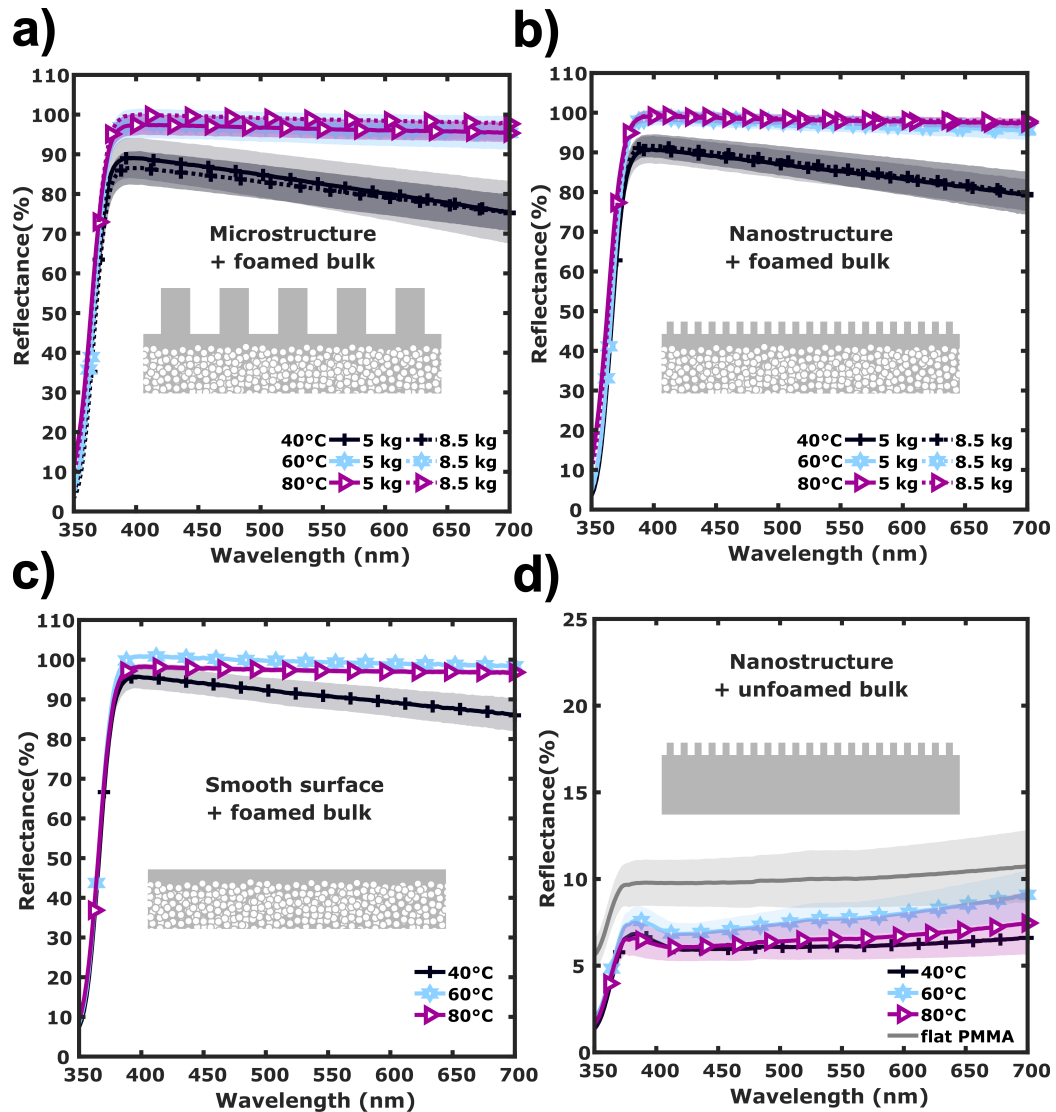
Figure 6.8: Reflectance spectra of foamed, white PMMA samples processed at different temperatures and embossed with a) a micro-structure, b) a nano-structure and c) a flat, featureless surface. While the reflection reducing effect of the nanostructure does not noticeably impair the reflectance for the highly scattering white samples a)-c), this effect can be observed for transparent, nano-structured samples shown in d). Each reflectance spectrum is averaged from 3 measurements and the shaded areas indicate the respective standard deviations. Please note the different scaling in d).

properties are related to the pore size and density, these will be considered in more detail in the following.

6.4.5 Pore size and density

The previous optical microscopy analysis of sample cross-sections already indicated that samples created with a facilitated diffusion due to a wire mesh have a white, foamed side and a transparent, non-porous side (see Figure 6.4 b)). This observation is confirmed by SEM examination, as shown in the cross-sectional overview in Figure 6.9. The transparent side facing the mold, is indeed non-porous with an imprinted surface structure. The wire mesh facing side is porous with large macropores in a transition zone between bulky and porous polymer. The porous side shows a distinct size gradient with small pores close to the surface open for diffusion and with larger pores towards the transition zone. For samples foamed at 40°C however no macropores are observed and the pore diameters are in the order of $< 100\,\text{nm}$. In this size range Rayleigh scattering can be considered, which is less efficient for light for longer wavelengths, which could explain the distinct decrease in reflectance towards the longer wavelength range observed in these samples (see Figure 6.8 a)-c)). The observation of a distinct pore size gradient throughout the thickness of the sample is in good agreement with other studies on graded foams created via supercritical CO_2 foaming [118, 209, 210]. Either incomplete saturation [209], as in this study, or a temperature gradient [210], or a combination of both [118], are reported to be the cause of a pore gradient.

The pore size gradient achieved by incomplete saturation can be explained by the gradient in CO_2 absorbed throughout the thickness of the polymer [209]. Towards the surface, through which CO_2 penetrates, a higher saturation with CO_2 is reached compared to deeper located regions in the polymer sheet. This is due to the limited exposure time, which did not allow to establish a homogeneous saturation through the whole sample. After the pressure quench the polymer becomes supersaturated, the higher the supersaturation, the lower is the activation energy to be overcome for nucleation [70]. Thus more nuclei can be formed on the side from which the CO_2 diffuses in, because this region is impregnated with CO_2 to a greater extend. A higher nucleation is accompanied by smaller pore sizes [209], due to the competition between pore growth and nucleation [73]. Increasingly large pores are in turn formed in the areas of decreasing CO_2 concentration, where the degree of supersaturation is lower and less nucleation takes place. In the transition zone only few nuclei are formed finally, the surrounding CO_2 contributes to the growth of these few pores, while in the non-porous region the CO_2 concentration is to low for the formation of pores. The samples obtained at 60 and 80°C process temperature were analyzed in terms
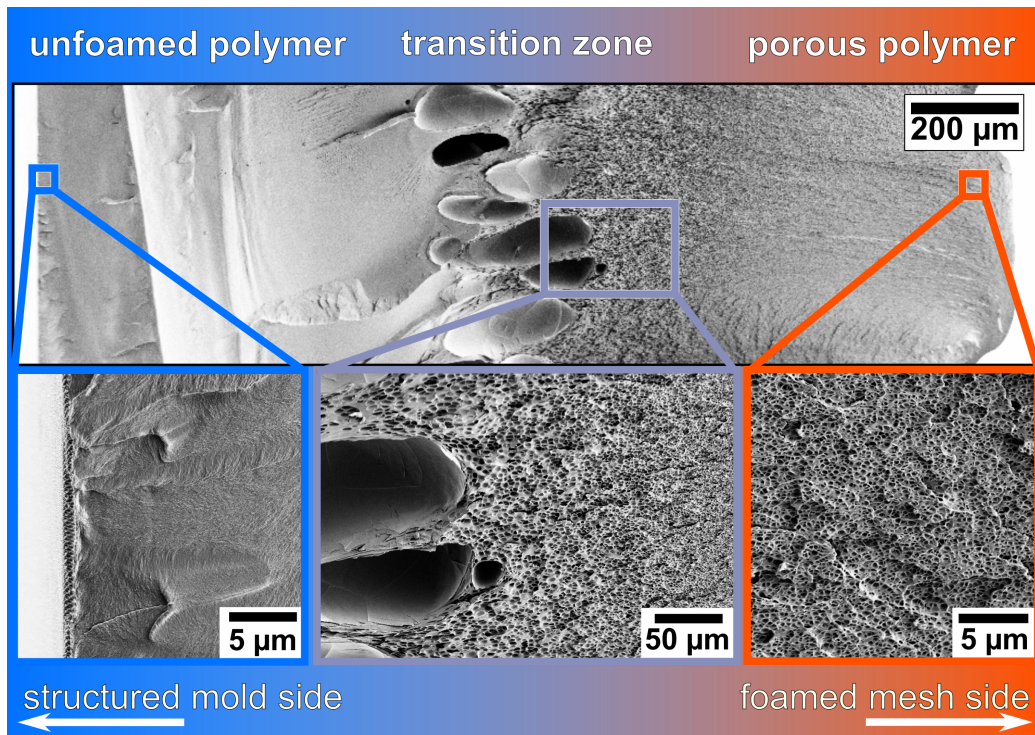
Figure 6.9: SEM micrograph of the cross-section of a foamed polymer, which was exposed to CO_2 diffusion from on side (mesh side) resulting in a pore size gradient. The side facing the mold is non-porous with a structured surface. Between the non-porous and the porous side a transition zone with large pores is formed. Pores closer to the mesh side are smaller than pores towards the transition zone.

of pore size and density in relation to distance from the diffusion surface of the sample, as summarized in Figure 6.10. The depth zero corresponds to the wire mesh side of the sample from where the diffusion takes place, the whiskers indicate the standard deviation of the average. The average pore radius increases clearly with increasing distance from the surface of facilitated diffusion, here fitted with an exponential function. The pores sizes are throughout more homogeneous toward the surface exposed to CO_2, as indicated by the lower standard deviation. This gradual change in pore size along the thickness direction depends on the foaming temperature and seems to be influenced by the magnet strength applied as well. In general, as expected, the porous layer is extended deeper for increasing temperature, because the diffusion rate of CO_2 is polymer is increased at higher temperatures [80]. At lower magnet strengths, the large pores appear to form in a deeper region of the polymer. The pressure exerted by the magnets
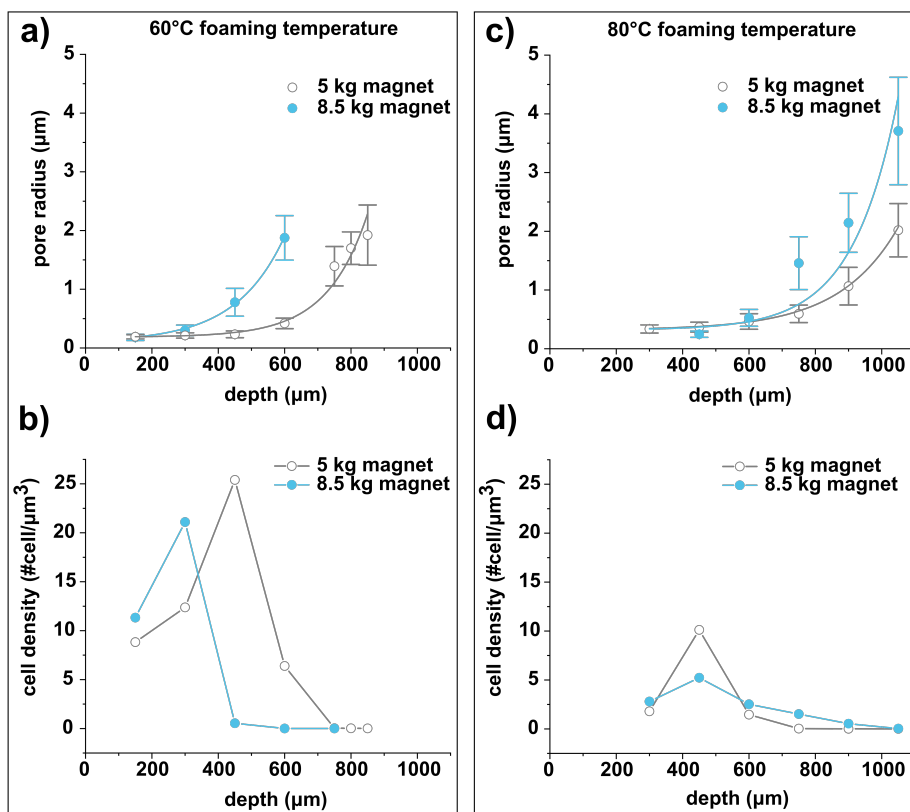
Figure 6.10: Comparison of the average pore radius a) and c) and the pore densities b) and d) of samples foamed at 60 and 80°C with different magnet strengths applied. The whiskers indicate the standard deviation of the average.

might hinder the swelling of the polymer as it absorbs CO_2 during the exposure time. This aspect could be clarified with an autoclave equipped with observation window, as this would allow observation of the propagation of the CO_2 diffusion front [81, 80]. Overall, comparable pore sizes are achieved with the same process parameters, but in different depths of the sample. For supercritical CO_2 foaming its is well established, that the pore size increases with rising temperature, while the pore density decreases [68]. Comparing the porous structures obtained at 60°C and 80°C these are in good agreement to this, with larger pores achieved at 80°C but with a generally lower pore density (see Figure 6.10). The highest pore densities are observed for small pores located in considerable distance from the surface, as CO_2 in proximity to the surface can easily escape to the surroundings an does not contribute to nucleation. The pore density then decreases again, following the trend of increasing pore sizes. Here, too, the influence of the magnetic strength can be observed as slightly higher pore densities in each case are

achieved for lower loads. However, for samples treated at 60 and 80°C the observed differences in the gradient of the pore size, as well as the achieved pore densities showed no distinct effect on the reflectance. The reflectance here is about as high as for the reference standard. For thinner foamed layers these differences however might cause more pronounced effects on the reflectance, which should be considered in this case.

6.5   Conclusion and Outlook

In this study, the combination of a simultaneous molding and foaming process using supercritical CO_2 was tested. For this purpose, a setup easy to integrate in a batch process was utilized, hereby the mold is pressed into the sample by means of magnets. The micro- and nanostructures selected for molding were inspired by biological self-cleaning structures such as those known from the lotus plant or insect compound eyes. A strategy to combine supercritical CO_2 foaming with the simultaneous imprinting of these structures was demonstrated. This is achieved by incomplete saturation of the polymer with CO_2 diffusion occurring from the side opposed to the mold. As a result, foamed white polymers with imprinted structures in the micro and nanometer range could be successfully produced. The height profile of the molded structures was evaluated by AFM measurements. The combination of foaming and structuring showed no adverse effect on the molded structures compared to exclusively patterned, transparent samples without an inner porous layer. The changes in wettability resulting from the structuring were evaluated by contact angle measurements. The initially hydrophilic polymer PMMA became hydrophobic for both micro- and nano structures, with static contact angles up to about 130°. However, superhydrophobicity required for self-cleaning and the easy roll-off of droplets at tilted angles were not achieved yet. This is attributed to the hydrophilic base material PMMA and the lack of a hierarchical composition of the replicated structures. The optical properties of the structured samples were investigated by spectrometric reflectance measurements with an integrating sphere. At process temperatures from 60°C on, a high reflectance over the entire visible spectrum was achieved, which was as high as the white reference standard. The pore size, density and the gradient in pore size resulting from the one-sided incomplete saturation was investigated by SEM.

From the point of view of material efficiency, the method presented could also be used for much thinner material layers. In this case, the exposure time would shorten further and the influence of the pore size and density might represent a higher influence factor for the reflectance achieved. A next point towards the targeted self-cleaning could be the imprinting of microstructures superim-

posed with nanoscale features and the utilization of hydrophobic materials in the process. In addition, many other structure-based surface functionalizations and resulting applications are conceivable. For the application field of passive radiative daytime cooling (see Chapter 5) the white, highly reflective polymer foam could be combined with microstructures interacting with light in the infrared wavelength range to enhance the emission properties in this range [25, 180]. Nanostructured cicada wings, exhibiting pillar structures similar to the previously described moth-eye-effect surfaces, were found to kill bacteria based on the surface structure [211, 212]. Thus these nanostructures provide a new approach for antibacterial surfaces [211, 212]. Supercritical CO_2 assisted embossing could be a suitable fabrication method for such surfaces, especially for microbial growth studies, as other influencing factors such as surface contamination with solvent residues or release agents and material oxidation at high temperatures are omitted [213].

The experimental characterisation of the samples was performed by Ester Priante in the course of her Masterthesis "Micro-nanostructuring of polymer surfaces via foaming with supercritical CO_2" [214] at the Institute of Microstructure Technology (IMT), KIT in 2022. A shortened version of this chapter is in preparation for submission as "Combined foaming and surface structuring of polymers with supercritical CO_2" by Luisa Maren Borgmann, Ester Priante, Siegbert Johnsen, Gabriele Wiegand, Markus Guttmann, Bendedikt Bläsi and Hendrik Hölscher.

Chapter 7

Summary and Outlook

This thesis focuses on the manufacture of porous polymers, their light scattering properties and their utilization in relevant application fields. In Chapter 2 theoretical aspects regarding the scattering of light and corresponding efficient strategies found in nature are presented together with an overview on the analytical methods utilized. Chapter 3 provides detailed background on supercritical CO_2 foaming, which is the method of choice throughout this work for the generation of light scattering pores in polymers. These polymers equipped with light-scattering nanopores by means of supercritical CO_2 have a wide range of applications, of which those of particular economic and scientific interest were addressed in the context of this work in particular in Chapters 4 and 5. The successful extension of the foaming process to obtain foamed and simultaneously surface-structured polymers as highlighted in Chapter 6 expands the possible fields of application even further. The main findings of the presented work and approaches for future research are summarized in the following paragraphs.

In Chapter 4 I investigated the opportunities and limits of utilizing **porous polymeric microparticles as scattering white pigments**. First the main issues concerning the conventional white pigment TiO_2 with regard to human health and the environment were discussed. As possible alternative white polymer foams created by supercritical CO_2 have previously been proposed in the shape of thin porous layers [17]. However, alternatives for currently used pigments are often desired to be effortlessly integratable into the existing process routes. Therefore the efforts in the present work were focused mainly on particle-shaped alternatives, due to the similar handling expected. Favourable parameters for equipping PMMA particles with light-scattering nanopores in a supercritical CO_2 foaming process were presented and successful foaming of the particles was confirmed. Reflectance measurements of foamed particles demonstrated their light scattering abilities, whereby the highest reflectance was achieved for a foaming

temperature of 110°C. The corresponding properties pore size and density were assessed by nano-CT and found to be in good agreement with predictions from literature for effective light scattering by air voids. In a next step the foaming process was optimized by utilizing different diffusion barriers to minimize the unfoamed layer and to enable the foaming of particles $< 60\,\mu m$. The surface deformations observable after foaming with a PVA-based diffusion barrier were associated to the formation of gas voids at the interface of particle and diffusion barrier. The process modification utilizing PVA as diffusion barrier enabled the successful foaming of particles down to $20\,\mu m$. The thereby altered optimal parameters for high reflectance were evaluated, with highest reflectance achieved for a foaming temperature of about 90°C. By using PVP as diffusion barrier material a further improvement in the reflectance properties was achieved compared to the PVA-based diffusion barrier at even lower process temperatures of only 80°C. Furthermore, it was investigated how the particles react to heating and to mechanical stress through micro compression. The introduced porosity does not compromise the mechanical properties and the opacity of the foamed particles starts to fade when heated above 115°C. A paint containing foamed particles with a distinct white color impression is presented as a first demonstration of the possible application as alternative for conventional pigments.

Next steps for a broader range of application is certainly the optimization of the process towards foaming of smaller particles $< 20\,\mu m$. Thereby further research into diffusion barriers with regard to their simplified processing, their uniform application and the most suitable material is a good starting point. In addition, the polymeric base material should also be selected carefully according to the respective application. When using polymers of artificial origin, attention should be paid to how they can be recycled or disposed after their period of use. Avoiding the use of pigment particles such as TiO_2 is certainly a good first step towards easier recycling. Hereby foaming with supercritical CO_2 offers a way to achieve a white color impression without additional pigments. When it comes to proper disposal, unfortunately a large amount of plastic enters and accumulates in the environment worldwide. In 2020 Lau et al. estimated the amount of plastic added to existing waste each year could increase from 188 million tonnes in 2016 to 380 million tonnes in 2040 [215, 216]. This plastic is in the overwhelmingly majority of cases non-degradable by biodegradation. In the environment these macroscopic plastic parts are gradually broken down into smaller pieces reaching at some point the microscopic size range, commonly referred to as microplastics. There are also microplastics (parts $\leq 5\,mm$ [217]) that are intentionally added to products, e.g. in the cosmetics sector, where they serve as exfoliation agents for removal of dead skin cells. These cannot be filtered out by current wastewater treatment systems and thus end up in the environment contributing to the microplastic pollution. Microplastics and their effect on the living organisms

were initially discussed especially in the context of marine environments [216] and the impact marine food webs [218]. Meanwhile microplastics were found in human blood [219], lung tissue [220] and placenta [221]. The estimation of possible health risks to humans caused by the ingestion and inhalation of micro and nanoplastics and their accumulation in the body are an emerging and urgent issue in research [217] and policy [222]. Recently the European Chemicals Agency (ECHA) proposed the restriction of intentionally added microplastic particles in products [222]. In 2021 the European Food Safety Authority (EFSA) held a scientific colloquium to assess human health risks of micro- and nanoplastics in food [223]. It can well be expected that, as a first step, the intentional use of microplastics, e.g. in cosmetics, will be banned in the near future, further supported through the efforts and political pressure of non-governmental organizations [224, 225]. It can be assumed that the foamed PMMA microparticles investigated in Chapter 4, could also enter the environment, depending on the respectively targeted area of application. Due to its high solubility for CO_2 PMMA was very well suited as a study model to investigate the opportunities for supercritcal foaming of mircoparticles, however it should be aimed towards more sustainable material choices in the long term. Hereby the utilization of bio-degradable polymers as base material for supercritical CO_2 foaming is a valuable first objective for further research. It has been shown, that CO_2 foaming is also applicable to bio-based and/or bio-degradable polymers such as polylactide [59, 226, 227], poly (butylene succinate) (PBS) [227], polycaprolactone [119, 226], cellulose acetate butyrate (CAB) [228] or cellulose acetate [229] to name a few. In own preliminary tests, PLA, cellulose acetate and poly(hydroxy butyrate) (PHB) have been tested and were found to be suitable materials for foaming with supercritical CO_2 in the present experimental setup. The further search for appropriate biodegradable and, at best, bio-based materials suitable for supercritical CO_2 foaming is an important next step for sustainable and versatile application of white, porous polymers as an alternative to conventional white pigments.

In Chapter 5 I discussed the possible utilization of **porous polymers for passive radiative daytime cooling**. The motivation of this project was that the demand for cooling systems is expected to increase sharply in the coming years, and the associated electricity consumption will pose a major challenge. Thus in this chapter the passive radiative daytime cooling strategy is introduced as promising method for heat mitigation without power consumption. Among the numerous approaches for materials with suitable optical properties, porous polymers in particular have attracted increasing interest due to their low price and usually facile up-scaling. The main factors to consider here are the minimum intake of solar radiation and the strong emission of radiation within the atmospheric window corresponding to the wavelength range of 8 to 13 µm. The former can be

achieved by highly reflective white surfaces and the latter is a material property of certain polymers. For this reason, polymers with advantageous emission properties were identified, which are additionally suitable for the generation of light scattering pores by means of supercritical CO_2 foaming. The chosen co-extruded PMMA-PVDF foils were successfully foamed with supercritical CO_2, whereby only the PMMA component showed a porous inner structure. The pore sizes increased with higher foaming temperatures, above 70°C the best results in terms of high reflectance are achieved. The maximum reflectance in the visible and near infrared was reached by the foil with the thickest PMMA component with about 65 μm thickness before foaming. With an average reflectance of about 87% in the wavelength range from 400 to 800 nm the foamed foil thus meets the requirement of a reflection >85% [152]. In the region up to 6 μm wavelength the reflectance is likewise enhanced due to the introduction of pores. In the atmospheric window region (8-13 μm) reflectance and transmittance remained unchanged and thus likewise the good emission properties. Due to the high reflection achievable in the visible wavelength range and the unaltered high emission of both foil components, foamed PMMA co-extruded with chemically resistant PVDF was identified as particularly suitable material for passive radiative cooling.

Although a sufficiently high reflectance was successfully achieved by introducing air cavities via supercritical CO_2 foaming in the PMMA component, the reflection should be further increased. Ideally a radiative cooling material would have a reflectance of 100% in the solar spectrum. The easiest step in this direction would be to enhance the thickness of the foamed part, i.e. the use of a foil with a larger PMMA component. Moreover, the evaluation of the suitability of the porous polymer foils under real conditions, as in an outdoor field trial, is still pending. Passive radiative daytime cooling materials on their own will for now probably not suffice to replace an active air conditioning system in most cases, but offer a supportive cooling effect to lower the electricity demand. However, especially low income housing often lacks any air conditioning in spite of need, thus urban heat waves can cause high temperature peaks [230]. Here inexpensive solutions like passively cooling surfaces could help to mitigate the heat load alternatively to expensive conventional air conditioning. Additionally a passive radiative cooling strategy could be highly beneficial in remote and rural areas, which are often not connected to the electricity grid.

In Chapter 6 I present a new approach for **combined foaming and surface structuring of polymers with supercritical CO_2**. While the previous chapters focused exclusively on the inner porous structures obtained by foaming, this chapter was devoted to additional surface structuring. The main approach here was to foam and to structure a polymer in one step. The former targets a high reflection all over the visible range, as required, e.g., in passive radiative day cool-

ing, the latter is intended to add beneficial surface properties. In particular the functionalization with a self-cleaning, dirt-repellent structure is of high interest. Thus the combination of a simultaneous molding and foaming process using supercritical CO_2 was investigated. In nature many self-cleaning surfaces have been described and thus provided a source of inspiration for suitable micro- and nanostructures for molding. The utilized mold in the microstructure range mimics the famous lotus effect. The nano-structured mold is intended to reproduce the multi functional moth-eye-effect. Due to the limitations given by the current batch process setup, an easy to integrate approach was implemented. Thereby magnets press a metallic mold onto the polymer during foaming. The structure is imprinted as the polymer becomes soft and deformable during CO_2 uptake, while foaming is initiated as previously by a rapid pressure release. However, the combination of supercritical CO_2 foaming with simultaneous imprinting of structures faced some issues. Main obstacle was the deformation of the imprinted structures taking place if foaming occurs in close proximity to the mold. An incomplete saturation of the polymer with CO_2 was found to be a suitable method to avoid this issue. Thereby the diffusion occurs only from the side opposed to the mold. The saturation time is chosen sufficiently short to avoid foaming close to the imprinted structures. With this strategy it was possible to create white polymers with imprinted surface structures. The comparison of height profiles of molded structures and the corresponding mold showed good agreement. Static contact angle measurements accessed the changes in wettability arising from the patterning. A flat PMMA surface has a low contact angle, as PMMA is hydrophilic. The structured polymers in contrast became hydrophobic for both micro- and nano patterns, with static contact angles up to about 130°. This however was not sufficient to achieve superhydrophobicity and self-cleaning properties yet. This can be attributed to the initially hydrophilic base material and the lack of a hierarchical composition of the investigated structures. Thus this would be two promising starting points for further improvement. The reflectance of the samples was investigated, showing that at process temperatures from 60°C on, a reflectance as high as the white reference standard could be achieved over the entire visible spectrum. The pore size and density as well as a gradient in pore size resulting from the incomplete saturation was investigated and corresponded well with the expectations for foaming of an incompletely CO_2 saturated polymer.

Based on the successful implementation of simultaneous, one-step supercritical CO_2 foaming and embossing, further aspects could be investigated in the future. In particular, a connection with the topic of passive radiative cooling is of high interest. Here, a self-cleaning surface is of great advantage, as dust accumulation would impair the scattering of the surface and thus the cooling performance. Since passive radiative cooling is particularly effective in dry,

hot climates, which in turn often lack sufficient rain available for self-cleaning surfaces, dry-cleaning surfaces would be beneficial here. Approaches utilizing bio-inspired surface structures for dry-self-cleaning are currently under development [231, 232], especially for the use in photovoltaics, but could also be of interest for surface modifications in passive radiative daytime cooling. Another approach to utilize combined foaming and surface structuring in the context of passive radiative cooling is to imprint structures to manipulate the optical properties towards higher absorption in the wavelength range of 8 to 13 µm. Thereby the mid-infra-red reflection is reduced by the gradual change in refractive index created by the structures, as with the previously described moth-eye-effect. This can be achieved with simple structures in the micrometer size range, as it has been demonstrated e.g. for pyramidal structures [180] or triangular ridges [233].

Acknowledgements

The work of the last four years and finally this thesis would not have been possible without the constant help and valuable support of a large number of dear colleagues and friends, whom I would like to thank most sincerely in the following.

First of all, I would like to express my gratitude to my supervisor Prof. Dr. Hendrik Hölscher, who gave me the opportunity for a master thesis and then to do my PhD in his research group. I am especially grateful for your attentive listening and receptive ear to all my questions, concerns and worries. The free room you created for individual ideas along with your gentle guidance and scientific advice, have made you an excellent mentor to me. Thank you also so much for facilitating such a pleasant working atmosphere. I really appreciated the calm attitude with which you guided me through this exciting time.

In addition, I would like to thank sincerely Prof. Dr. Christian Greiner and Prof. Dr. Cordt Zollfrank sincerly for taking the effort to be my co-referees.

I owe a very big thank-you to my colleagues Dr. Gabriele Wiegand and Siegbert Johnsen from the IKFT, for sharing not only their expertise in supercritical CO_2 foaming, but also their lab and devices with me. Special thanks go to Siegbert for his endless, hands-on help throughout my work and his continuous support in any situation.

I would like to thank Dr. Guillaume Gomard for his scientific advice and his continuous support in finding great cooperation partners for challenging research questions.

My sincere thanks to Cristine Santos de Oliveira and Dr. Juliana Martins de Souza e Silva from the Institute of Physics at the Martin-Luther-Universität Halle-Wittenberg for their great nano-CT study and the pleasant collaboration.

Many thanks also to Dr. Juan Li and Prof. Dr. Christoph Kirchlechner from the IAM for doing the micro compression experiments and their kind support during the collaboration.

I would also like to thank Dr. Benedikt Bläsi from the Fraunhofer Institute for Solar Energy Systems ISE for providing a microstructured mold and for his valuable advice.

I owe special thanks to all the organizers and participants of the DFG priority program "SPP 1839 Tailored Disorder", in the framework of which this thesis was written. It has enabled me to discover many fascinating research topics and the people behind them.

I would also like to thank Prof. Dr. Heike Beismann, whose student I was during my bachelor's degree and who later encouraged me convincingly to pursue a PhD.

Many thanks to all the members of the research group Biomimetic Surfaces and Scanning Probe Technologies for their continuous support, great collaboration and stimulating scientific and non-scientific disscusions. In particular I would like to thank Richard Thelen for his help and support in the lab, with safety questions and all big and small problems of the research everyday life.

Special thanks I owe to Ronja Meschede, Ester Priante and Pit Juhl, whose bachelor and master theses I was supervising and whose contributions in the form of experimental results, creative solutions and fruitful discussions have enriched my work and given me immense enjoyment.

Additionally, I would like to thank the whole IMT staff, especially Dr. Markus Guttmann and his team for their expertise in electroplating, Alexandra Moritz and her team for the help in the workshop, Marc Schneider for his support with hot embossing and Birgit Hübner for her constant help with many large and small challenges in the laboratory.

I would also like to express my sincere thanks to all the colleagues helping me with all the non-scientific tasks, that became an organizational challenge especially due to the limitations of the COVID-19 pandemic. Many thanks to Siegfried Roth, Manuel Frismann and Nina Giraud just to name a few.

I would like to express my gratitude also to my colleagues from the LTI, especially Dr. Yidenekachew Jenberu Donie, Dr. Dominik Theobald, Junchi Chen and Qiaoshuang Zhang for the joyful collaborations, valuable support and interesting discussions. I would like to express my sincere thanks to Laura Bosch and Dr. Rainer Körber from the IRM, who supported us in our search for possible cooperation partners with great enthusiasm for the topic.

A special thanks goes to all who shared with me all the ups and downs of being a PhD student and made this stage of my life a special and joyful one: Laura, David, Lena, Leona, Pouria, Josephine, Gowtham and many more, thank you all so much for your sympathetic ear and the patient, continous encouragement. Additionally I owe many thanks especially to Laura for the careful proofreading of my thesis and Gowtham for his valuable advice for everything related to the SEM.

Difficult to put into words is my profound gratitude for my partner Matthias, who has been by my side since many years and has lovingly supported me during our time together as students, throughout my PhD and through ups and downs in life quite generally. Thank you a lot also for listening to me in all the little details, which often kept me busy even after work, no matter if you understood what I was talking about or not.

Finally I would like to thank my and also Matthias family for everything they have done for me, all their generous support. I especially appreciate and thank my parents for encouraging my interest in science, all the stimulating conversations over coffee and cake and the continued curiosity for my work.

List of Publications

Articles

1. Andrés Dolinko, **Luisa Borgmann**, Christian Lutz, Ernest Ronald Curticean, Irene Wacker, María Sol Vidal, Candela Szischik, Yidenekachew Donie, Marina Inchaussandague, Diana Skigin, Hendrik Hölscher, Pablo Tubaro, Ana Barreira *Analysis of the optical properties of the silvery spots on the wings of the Gulf Fritillary, Dione vanillae*, Scientific Reports, **11**, 19341, (2021).

2. Dominik Theobald, Dominik Beutel, **Luisa Borgmann**, Henning Mescher, Guillaume Gomard, Carsten Rockstuhl, Uli Lemmer, *Simulation of light scattering in large, disordered nanostructures using a periodic T-matrix method*, Journal of Quantitative Spectroscopy and Radiative Transfer, **272**, 107802, (2021).

3. **Luisa Maren Borgmann**, Siegbert Johnsen, Cristine Santos de Oliveira, Juliana Martins de Souza e Silva, Juan Li, Christoph Kirchlechner, Guillaume Gomard, Gabriele Wiegand, Hendrik Hölscher *Porous polymeric microparticles foamed with supercritical CO_2 as scattering white pigments* Bioinspiration & Biomimetics , **18**, 026011 (2023).

Conference Contributions

10.-11.12.2019 **Luisa Borgmann**, Siegbert Johnsen, Gabriele Wiegand, Uli Lemmer , Guillaume Gomard, Hendrik Hölscher *Bio-inspired porous polymer films with tunable light scattering properties for optical applications*, Poster presentation, Symposium Nano-BW 2019, Bad Herrenalb, Germany.

20.-22.07.2020 **Luisa Borgmann**, Andrés Dolinko, Christian Lutz, Ernest Ronald Curticean, Irene Wacker, María Sol Vidal, Candela Szischik, Marina Inchaussandague, Diana Skigin, Hendrik Hölscher, Pablo Tubaro, Ana Barreira, *Analysis of the optical properties of the silver spots on the wings of the Gulf Fritillary, Dione vanillae*, Poster presentation, Biological and bio-inspired optics Faraday Discussion - Living Light edition, online.

22.-23.09.2021 **Luisa Borgmann**, Cristine Santos de Oliveira, Siegbert Johnsen, Gabriele Wiegand, Guillaume Gomard, Hendrik Hölscher, *Bio-inspired Highly Scattering White Polymer Materials Fabricated by Foaming with Supercritical CO_2 as Replacement for TiO_2*, Poster presentation, Early Career Researcher Living Light 2021, online.

30.06.2021   **Luisa Borgmann**, Julia Syurik und Hendrik Hölscher, *White surfaces without Titanium dioxide - Porous nanostructures as replacement for white pigments*, Poster presentation, Neuland-Innovationstag-2021, online.

21.-24.03.2022   **Luisa Borgmann**, Siegbert Johnsen, Gabriele Wiegand, Guillaume Gomard, Uli Lemmer, Hendrik Hölscher, *Porous Polymeric Microparticles Foamed with Supercritical CO_2 as Scattering White Pigments*, Poster presentation, Bioinspired Materials 2022, Kostenz, Germany.

27.11-2.12.2022   **Luisa Maren Borgmann**, Siegbert Johnsen, Gabriele Wiegand, Hendrik Hölscher, *Easily recyclable white polymer films as replacement for TiO_2 pigments*, Poster presentation, Materials Research Society Fall Meeting & Exhibit 2022, Boston, United States.

19.-21.06.2023   **Luisa Maren Borgmann**, S. Johnsen, G. Wiegand, H. Hölscher, *Extension of supercritical CO_2 foaming process for downsized porous microparticles as alternative polymeric white pigments*, Poster presentation, awarded with the 1st poster prize, 2nd International School and Conference on Disorder in Materials Science 2023, Plankstetten, Germany.

Bibliography

[1] Gustav Mie. Beiträge zur Optik trüber Medien, speziell kolloidaler Metallösungen. *Annalen der Physik*, 330(3):377–445, 1908. doi: 10.1002/andp. 19083300302.

[2] Michael P. Diebold. *Application of Light Scattering to Coatings*. Springer International Publishing, Cham, 2014. doi: 10.1007/978-3-319-12015-7.

[3] Hans Christian Winkler, Tina Notter, Urs Meyer, and Hanspeter Naegeli. Critical review of the safety assessment of titanium dioxide additives in food. *Journal of Nanobiotechnology*, 16(1):51, 2018. doi: 10.1186/ s12951-018-0376-8.

[4] International Agency for Research on Cancer. *IARC Monographs on the Evaluation of Carcinogenic Risks to Humans: Carbon Black, Titanium Dioxide, and Talc*, volume 93. World Health Organization (WHO), Lyon, 2010. ISBN 9283212932.

[5] EFSA Panel on Food Additives and Nutrient Sources added to Food (ANS). Re-evaluation of titanium dioxide (E171) as a food additive. *EFSA Journal*, 14(9):4545, 2016. doi: 10.2903/j.efsa.2016.4545.

[6] National Research Institute for Agriculture, Food and the Environment INRAE. Food additive E171: first findings of oral exposure to titanium dioxide nanoparticles. https://www.inrae.fr/en/news/food-additive-e171-first-findings-oral-exposure, 2017. Accessed: 2020-03-27.

[7] EFSA Panel on Food Additives and Nutrient Sources added to Food (ANS). Evaluation of four new studies on the potential toxicity of titanium dioxide used as a food additive (E 171). *EFSA Journal*, 16(7):5366, 2018. doi: 10.2903/ j.efsa.2018.5366.

[8] l'Agence nationale de sécurité sanitaire de l'alimentation, de l'environnement et du travail ANSES. Food additive E171: ANSES reiterates its recommendations for consumer safety.

https://www.anses.fr/en/content/food-additive-e171-anses-reiterates-its-recommendations-consumer-safety, 2019. Accessed: 2020-03-27.

[9] EFSA Panel on Food Additives and Flavourings (FAF). Scientific opinion on the proposed amendment of the EU specifications for titanium dioxide (E 171) with respect to the inclusion of additional parameters related to its particle size distribution. *EFSA Journal*, 17(7):5760, 2019. doi: 10.2903/j. efsa.2019.5760.

[10] Bruno Le Maire, ministre de l'économie et des finances et François de Rugy, ministre d'Etat, ministre de la transition écologique et solidaire. Arrêté du 17 avril 2019 portant suspension de la mise sur le marché des denrées contenant l'additif E 171 (dioxyde de titane - TiO$_2$). https://www.legifrance.gouv.fr/eli/arrete/2019/4/17/ECOC1911549A/jo/texte, 2019. Accessed: 2020-03-27.

[11] Official Journal of the European Union. Commission Regulation (EU) 2022/63 of 14 January 2022 amending Annexes II and III to Regulation (EC) No 1333/2008 of the European Parliament and of the Council as regards the food additive titanium dioxide (E 171) (Text with EEA relevance). http://data.europa.eu/eli/reg/2022/63/oj, 2022. Accessed: 2022-02-28.

[12] Manuel Jesús Gázquez, Juan Pedro Bolívar, Rafael Garcia-Tenorio, and Federico Vaca. A review of the production cycle of titanium dioxide pigment. *Materials Sciences and Applications*, 05(07):441–458, 2014. doi: 10.4236/msa.2014.57048.

[13] M. J. A. Ruszala, , N. A. Rowson, L. M. Grover, and R. A. Choudhery. Low carbon footprint TiO$_2$ substitutes in paint: A review. *International Journal of Chemical Engineering and Applications*, 6(5):331–340, 2015. doi: 10.7763/ ijcea.2015.v6.505.

[14] David Lee. *Nature's Palette.* University of Chicago Press, Chicago, 2007. ISBN 978-0-226-47105-1. doi: 10.7208/chicago/9780226471051.001.0001.

[15] Stephen M. Luke, Benny T. Hallam, and Peter Vukusic. Structural optimization for broadband scattering in several ultra-thin white beetle scales. *Applied Optics*, 49(22):4246–4254, 2010. doi: 10.1364/ao.49.004246.

[16] Andrew J. Parnell, Adam L. Washington, Oleksandr O. Mykhaylyk, Christopher J. Hill, Antonino Bianco, Stephanie L. Burg, Andrew J. C. Dennison, Mary Snape, Ashley J. Cadby, Andrew Smith, Sylvain Prevost, David M. Whittaker, Richard A. L. Jones, J. Patrick. A. Fairclough, and

Andrew R. Parker. Spatially modulated structural colour in bird feathers. *Scientific Reports*, 5(1):18317, 2015. doi: 10.1038/srep18317.

[17] Julia Syurik, Radwanul Hasan Siddique, Antje Dollmann, Guillaume Gomard, Marc Schneider, Matthias Worgull, Gabriele Wiegand, and Hendrik Hölscher. Bio-inspired, large scale, highly-scattering films for nanoparticle-alternative white surfaces. *Scientific Reports*, 7(1), 2017. doi: 10.1038/srep46637.

[18] Ronnen Levinson, Heng Pan, George Ban-Weiss, Pablo Rosado, Riccardo Paolini, and Hashem Akbari. Potential benefits of solar reflective car shells: Cooler cabins, fuel savings and emission reductions. *Applied Energy*, 88 (12):4343–4357, 2011. doi: 10.1016/j.apenergy.2011.05.006.

[19] M. Santamouris. On the energy impact of urban heat island and global warming on buildings. *Energy and Buildings*, 82:100–113, 2014. doi: 10.1016/j.enbuild.2014.07.022.

[20] Po-Chun Hsu, Alex Y. Song, Peter B. Catrysse, Chong Liu, Yucan Peng, Jin Xie, Shanhui Fan, and Yi Cui. Radiative human body cooling by nanoporous polyethylene textile. *Science*, 353(6303):1019–1023, 2016. doi: 10.1126/science.aaf5471.

[21] Jyotirmoy Mandal, Yanke Fu, Adam C. Overvig, Mingxin Jia, Kerui Sun, Norman N. Shi, Hua Zhou, Xianghui Xiao, Nanfang Yu, and Yuan Yang. Hierarchically porous polymer coatings for highly efficient passive daytime radiative cooling. *Science*, 362(6412):315–319, 2018. doi: 10.1126/science.aat9513.

[22] Norman Nan Shi, Cheng-Chia Tsai, Michael J. Carter, Jyotirmoy Mandal, Adam C. Overvig, Matthew Y. Sfeir, Ming Lu, Catherine L. Craig, Gary D. Bernard, Yuan Yang, and Nanfang Yu. Nanostructured fibers as a versatile photonic platform: radiative cooling and waveguiding through transverse anderson localization. *Light: Science & Applications*, 7(1), 2018. doi: 10.1038/s41377-018-0033-x.

[23] A. Leroy, B. Bhatia, C. C. Kelsall, A. Castillejo-Cuberos, M. Di Capua H., L. Zhao, L. Zhang, A. M. Guzman, and E. N. Wang. High-performance subambient radiative cooling enabled by optically selective and thermally insulating polyethylene aerogel. *Science Advances*, 5(10):eaat9480, 2019. doi: 10.1126/sciadv.aat9480.

[24] Erik Torgerson and Josh Hellhake. Polymer solar filter for enabling direct daytime radiative cooling. *Solar Energy Materials and Solar Cells*, 206: 110319, 2020. doi: 10.1016/j.solmat.2019.110319.

[25] Tong Wang, Yi Wu, Lan Shi, Xinhua Hu, Min Chen, and Limin Wu. A structural polymer for highly efficient all-day passive radiative cooling. *Nature Communications*, 12(1), 2021. doi: 10.1038/s41467-020-20646-7.

[26] Dongliang Zhao, Ablimit Aili, Yao Zhai, Shaoyu Xu, Gang Tan, Xiaobo Yin, and Ronggui Yang. Radiative sky cooling: Fundamental principles, materials, and applications. *Applied Physics Reviews*, 6(2):021306, 2019. doi: 10.1063/1.5087281.

[27] Craig F. Bohren and Donald R. Huffman. *Absorption and Scattering of Light by Small Particles*. Wiley-VCH, Weinheim, 1998. ISBN 978-0-471-29340-8.

[28] Dieter Meschede. *Gerthsen Physik*. Springer Spektrum Berlin, Heidelberg, 2015. doi: 10.1007/978-3-662-45977-5.

[29] Eugene Hecht. *Optik*. De Gruyter, Berlin, Boston, 2018. doi: 10.1515/9783110526653.

[30] Shuichi Kinoshita and Shinya Yoshioka. Structural colors in nature: The role of regularity and irregularity in the structure. *ChemPhysChem*, 6(8): 1442–1459, 2005. ISSN 1439-4235. doi: 10.1002/cphc.200500007.

[31] Davide Comoretto, editor. *Organic and Hybrid Photonic Crystals*. Springer International Publishing, Cham, 2015. doi: 10.1007/978-3-319-16580-6.

[32] Andrew Richard Parker. 515 million years of structural colour. *Journal of Optics A: Pure and Applied Optics*, 2(6):R15–R28, 2000. doi: 10.1088/1464-4258/2/6/201.

[33] A.C. Neville. Metallic gold and silver colours in some insect cuticles. *Journal of Insect Physiology*, 23(10):1267–1274, 1977. doi: 10.1016/0022-1910(77)90069-5.

[34] Lord Rayleigh. XXXIV. On the transmission of light through an atmosphere containing small particles in suspension, and on the origin of the blue of the sky. *The London, Edinburgh, and Dublin Philosophical Magazine and Journal of Science*, 47(287):375–384, 1899. doi: 10.1080/14786449908621276.

[35] Philip Laven. MiePlot v.4.6.18. http://philiplaven.com/mieplot.htm, 2020. Accessed: 2023-02-28.

[36] Scatterlib. Light scattering codes library. http://scatterlib.wikidot.com/mie. Accessed: 2023-02-28.

[37] Jochen Winkler. *Titanium Dioxide : production, properties and effective usage.* European coatings tech files. Vincentz Network, Hanover, 2., rev. ed. edition, 2013. ISBN 9783866308121.

[38] W. L. Bond. Measurement of the refractive indices of several crystals. *Journal of Applied Physics*, 36(5):1674–1677, 1965. doi: 10.1063/1.1703106.

[39] N. Sultanova, S. Kasarova, and I. Nikolov. Dispersion properties of optical polymers. *Acta Physica Polonica A*, 116(4):585–587, 2009. doi: 10.12693/aphyspola.116.585.

[40] Hein L. Leertouwer, Bodo D. Wilts, and Doekele G. Stavenga. Refractive index and dispersion of butterfly chitin and bird keratin measured by polarizing interference microscopy. *Optics Express*, 19(24):24061, 2011. doi: 10.1364/oe.19.024061.

[41] D. G. Stavenga, S. Stowe, K. Siebke, J. Zeil, and K. Arikawa. Butterfly wing colours: scale beads make white pierid wings brighter. *Proceedings of the Royal Society of London. Series B: Biological Sciences*, 271(1548):1577–1584, 2004. doi: 10.1098/rspb.2004.2781.

[42] Bodo D. Wilts, Bas Wijnen, Hein L. Leertouwer, Ullrich Steiner, and Doekele G. Stavenga. Extreme refractive index wing scale beads containing dense pterin pigments cause the bright colors of pierid butterflies. *Advanced Optical Materials*, 5(3):1600879, 2016. doi: 10.1002/adom.201600879.

[43] J. Lafait, C. Andraud, S. Berthier, J. Boulenguez, P. Callet, S. Dumazet, M. Rassart, and J.-P. Vigneron. Modeling the vivid white color of the beetle calothyrza margaritifera. *Materials Science and Engineering: B*, 169(1-3):16–22, 2010. doi: 10.1016/j.mseb.2009.12.026.

[44] Matteo Burresi, Lorenzo Cortese, Lorenzo Pattelli, Mathias Kolle, Peter Vukusic, Diederik S. Wiersma, Ullrich Steiner, and Silvia Vignolini. Bright-white beetle scales optimise multiple scattering of light. *Scientific Reports*, 4(1):6075, 2014. doi: 10.1038/srep06075.

[45] Lisandro T. Bazzano, Lucas R. Mendicino, Marina E. Inchaussandague, Diana C. Skigin, Natalia C. García, Pablo L. Tubaro, and Ana S. Barreira. Mechanisms involved in the production of differently colored feathers in

the structurally colored swallow tanager (Tersina viridis; Aves: Thraupidae). *Journal of Experimental Zoology Part B: Molecular and Developmental Evolution*, 336(5):404–416, 2021. doi: 10.1002/jez.b.23043.

[46] Helen Ghiradella. Insect cuticular surface modifications. In *Advances in Insect Physiology: Insect Integument and Colour*, pages 135–180. Elsevier, 2010. doi: 10.1016/s0065-2806(10)38006-4.

[47] P. Vukusic, B. Hallam, and J. Noyes. Brilliant whiteness in ultrathin beetle scales. *Science*, 315(5810):348–348, 2007. doi: 10.1126/science.1134666.

[48] Lorenzo Cortese, Lorenzo Pattelli, Francesco Utel, Silvia Vignolini, Matteo Burresi, and Diederik S. Wiersma. Anisotropic light transport in white beetle scales. *Advanced Optical Materials*, 3(10):1337–1341, 2015. doi: 10. 1002/adom.201500173.

[49] Benny T. Hallam, Anthony G. Hiorns, and Peter Vukusic. Developing optical efficiency through optimized coating structure: biomimetic inspiration from white beetles. *Applied Optics*, 48(17):3243, 2009. doi: 10.1364/ao.48.003243.

[50] Bodo D. Wilts, Xiaoyuan Sheng, Mirko Holler, Ana Diaz, Manuel Guizar-Sicairos, Jörg Raabe, Robert Hoppe, Shu-Hao Liu, Richard Langford, Olimpia D. Onelli, Duyu Chen, Salvatore Torquato, Ullrich Steiner, Christian G. Schroer, Silvia Vignolini, and Alessandro Sepe. Evolutionary-optimized photonic network structure in white beetle wing scales. *Advanced Materials*, 30(19):1702057, 2017. doi: 10.1002/adma.201702057.

[51] C. W. Mason. Structural colors in feathers. *The Journal of Physical Chemistry*, 27(3):201–251, 1923. doi: 10.1021/j150228a001.

[52] Branislav Igic, Liliana D'Alba, and Matthew D. Shawkey. Fifty shades of white: how white feather brightness differs among species. *The Science of Nature*, 105(3-4), 2018. doi: 10.1007/s00114-018-1543-3.

[53] W. L N. Tickell. White plumage. *Waterbirds*, 26(1):1–12, 2003. doi: 10. 1675/1524-4695(2003)026[0001:wp]2.0.co;2.

[54] Peter W. Hawkes and John C. H. Spence, editors. *Springer Handbook of Microscopy*. Springer International Publishing, Cham, 2019. doi: 10.1007/ 978-3-030-00069-1.

[55] Johannes Schindelin, Ignacio Arganda-Carreras, Erwin Frise, Verena Kaynig, Mark Longair, Tobias Pietzsch, Stephan Preibisch, Curtis Rueden, Stephan Saalfeld, Benjamin Schmid, Jean-Yves Tinevez, Daniel James White, Volker Hartenstein, Kevin Eliceiri, Pavel Tomancak, and Albert Cardona. Fiji: an open-source platform for biological-image analysis. *Nature Methods*, 9(7):676–682, 2012. doi: 10.1038/nmeth.2019.

[56] Shannon L. Storm, Art Springsteen, and Trudy M. Ricker. Labsphere Application Note: The Use of Center Mount Sample Holders in Reflectance Spectroscopy. Technical Report 02, Labsphere Inc., 1998.

[57] D. Nečas and P. Klapetek. Gwyddion modular program for scanning probe microscopy data visualization and analysis. http://gwyddion.net/, 2022. Accessed:2023-06-27.

[58] B. Notario, J. Pinto, and M.A. Rodriguez-Perez. Nanoporous polymeric materials: A new class of materials with enhanced properties. *Progress in Materials Science*, 78-79:93–139, 2016. doi: 10.1016/j.pmatsci.2016.02.002.

[59] H.-P Hentze and M Antonietti. Porous polymers and resins for biotechnological and biomedical applications. *Reviews in Molecular Biotechnology*, 90(1):27–53, 2002. doi: 10.1016/s1389-0352(01)00046-0.

[60] Jane E. Martini-Vvedensky, Nam P. Suh, and Francis A. Waldman. Microcellular closed cell foams and their method of manufacture - US Patent 4,473,665, 1984.

[61] Stéphane Costeux. CO_2-blown nanocellular foams. *Journal of Applied Polymer Science*, 131(23):41239, 2014. doi: 10.1002/app.41293.

[62] Chimezie Okolieocha, Daniel Raps, Kalaivani Subramaniam, and Volker Altstädt. Microcellular to nanocellular polymer foams: Progress (2004–2015) and future directions - A review. *European Polymer Journal*, 73:500–519, 2015. doi: 10.1016/j.eurpolymj.2015.11.001.

[63] Sameer P. Nalawade, Francesco Picchioni, and L.P.B.M. Janssen. Supercritical carbon dioxide as a green solvent for processing polymer melts: Processing aspects and applications. *Progress in Polymer Science*, 31(1): 19–43, 2006. doi: 10.1016/j.progpolymsci.2005.08.002.

[64] J. S. Chiou, J. W. Barlow, and D. R. Paul. Plasticization of glassy polymers by CO_2. *Journal of Applied Polymer Science*, 30(6):2633–2642, 1985. doi: 10.1002/app.1985.070300626.

[65] Yeong-Tarng Shieh, Jan-Hon Su, Gurusamy Manivannan, Paul H. C. Lee, Samuel P. Sawan, and W. Dale Spall. Interaction of supercritical carbon dioxide with polymers. II. amorphous polymers. *Journal of Applied Polymer Science*, 59(4):707–717, 1996. doi: 10.1002/(SICI)1097-4628(19960124) 59:4⟨707::AID-APP16⟩3.0.CO;2-M.

[66] T. S. Chow. Glass transition temperature of polymer-diluent systems. *Ferroelectrics*, 30(1):139–145, 1980. doi: 10.1080/00150198008209505.

[67] Yeong-Tarng Shieh, Jan-Hon Su, Gurusamy Manivannan, Paul H. C. Lee, Samuel P. Sawan, and W. Dale Spall. Interaction of supercritical carbon dioxide with polymers. I. crystalline polymers. *Journal of Applied Polymer Science*, 59(4):695–705, 1996. doi: 10.1002/(SICI)1097-4628(19960124)59: 4⟨695::AID-APP15⟩3.0.CO;2-P.

[68] Satish K. Goel and Eric J. Beckman. Generation of microcellular polymeric foams using supercritical carbon dioxide. I: Effect of pressure and temperature on nucleation. *Polymer Engineering and Science*, 34(14):1137–1147, 1994. doi: 10.1002/pen.760341407.

[69] Luisa Maren Borgmann, Siegbert Johnsen, Cristine Santos de Oliveira, Juliana Martins de Souza e Silva, Juan Li, Christoph Kirchlechner, Guillaume Gomard, Gabriele Wiegand, and Hendrik Hölscher. Porous polymeric microparticles foamed with supercritical CO_2 as scattering white pigments. *Bioinspiration & Biomimetics*, 18(2):026011, 2023. doi: 10.1088/1748-3190/ acb899.

[70] David L. Tomasko, Hongbo Li, Dehua Liu, Xiangmin Han, Maxwell J. Wingert, L. James Lee, and Kurt W. Koelling. A review of CO_2 applications in the processing of polymers. *Industrial & Engineering Chemistry Research*, 42(25):6431–6456, 2003. doi: 10.1021/ie030199z.

[71] Satish K. Goel and Eric J. Beckman. Nucleation and growth in microcellular materials: Supercritical CO_2 as foaming agent. *AIChE Journal*, 41(2):357–367, 1995. doi: 10.1002/aic.690410217.

[72] Satish K. Goel and Eric J. Beckman. Generation of microcellular polymeric foams using supercritical carbon dioxide. II: Cell growth and skin formation. *Polymer Engineering and Science*, 34(14):1148–1156, 1994. doi: 10.1002/pen.760341408.

[73] Chul B. Park, Daniel F. Baldwin, and Nam P. Suh. Effect of the pressure drop rate on cell nucleation in continuous processing of microcel-

lular polymers. *Polymer Engineering and Science*, 35(5):432–440, 1995. doi: 10.1002/pen.760350509.

[74] A. R. Berens and G. S. Huvard. Interaction of polymers with near-critical carbon dioxide. In *ACS Symposium Series*, pages 207–223. American Chemical Society, 1989. doi: 10.1021/bk-1989-0406.ch014.

[75] John Crank. *The Mathematics of Diffusion.* Clarendon Press, Oxford, 1975. ISBN 0198533446.

[76] C. M. Balik. On the extraction of diffusion coefficients from gravimetric data for sorption of small molecules by polymer thin films. *Macromolecules*, 29(8):3025–3029, 1996. doi: 10.1021/ma9509467.

[77] Kimberly F Webb and Amyn S Teja. Solubility and diffusion of carbon dioxide in polymers. *Fluid Phase Equilibria*, 158-160:1029–1034, 1999. doi: 10.1016/s0378-3812(99)00153-3.

[78] Silvia Orsi, Ernesto Di Maio, Salvatore Iannace, and Paolo A. Netti. Hollow micro- and nano-particles by gas foaming. *Nano Research*, 7(7):1018–1026, 2014. doi: 10.1007/s12274-014-0465-4.

[79] Vito Di Noto, Keti Vezzù, Guinevere A. Giffin, Fosca Conti, and Alberto Bertucco. Effect of high pressure CO_2 on the structure of PMMA: A FT-IR study. *The Journal of Physical Chemistry B*, 115(46):13519–13525, 2011. doi: 10.1021/jp207917n.

[80] Lev N. Nikitin, Ernest E. Said-Galiyev, Rostislav A. Vinokur, Alexei R. Khokhlov, Marat O. Gallyamov, and Kjeld Schaumburg. Poly(methyl methacrylate) and poly(butyl methacrylate) swelling in supercritical carbon dioxide. *Macromolecules*, 35(3):934–940, 2002. doi: 10.1021/ma010271+.

[81] Ruosong Li, Na Ye, Vahid Shaayegan, and Tao Fang. Experimental measurement of CO_2 diffusion in PMMA and its effect on microcellular foaming. *The Journal of Supercritical Fluids*, 135:180–187, 2018. ISSN 0896-8446. doi: https://doi.org/10.1016/j.supflu.2018.01.024.

[82] Jessica Elzea Kogel, Nikhil C Trivedi, James M Barker, and Stanley T Krukowski. *Industrial minerals & rocks: commodities, markets, and uses.* Society for Mining, Metallurgy, and Exploration (SME), Littleton, 2006. ISBN 978-0-87335-233-8.

[83] Juergen H. Braun, Andrejs Baidins, and Robert E. Marganski. TiO_2 pigment technology: a review. *Progress in Organic Coatings*, 20(2):105–138, 1992. doi: 10.1016/0033-0655(92)80001-d.

[84] Laurel G. Woodruff, George M. Bedinger, and Nadine M. Piatak. Titanium. In *Critical Mineral Resources of the United States—Economic and Environmental Geology and Prospects for Future Supply*, page T1–T23. U.S. Geological Survey, 2017. doi: 10.3133/pp1802t.

[85] Thomas C. Long, Navid Saleh, Robert D. Tilton, Gregory V. Lowry, and Bellina Veronesi. Titanium Dioxide (P25) Produces Reactive Oxygen Species in Immortalized Brain Microglia (BV2): Implications for Nanoparticle Neurotoxicity. *Environmental Science & Technology*, 40(14):4346–4352, 2006. doi: 10.1021/es060589n.

[86] A. S. Yazdi, G. Guarda, N. Riteau, S. K. Drexler, A. Tardivel, I. Couillin, and J. Tschopp. Nanoparticles activate the NLR pyrin domain containing 3 (Nlrp3) inflammasome and cause pulmonary inflammation through release of IL-α and IL-β. *Proceedings of the National Academy of Sciences*, 107 (45):19449–19454, 2010. doi: 10.1073/pnas.1008155107.

[87] Mirco Bundschuh, Frank Seitz, Ricki R. Rosenfeldt, and Ralf Schulz. Titanium dioxide nanoparticles increase sensitivity in the next generation of the water flea daphnia magna. *PLoS ONE*, 7(11):e48956, 2012. doi: 10.1371/journal.pone.0048956.

[88] Pedro A Ruiz, Belen Morón, Helen M Becker, Silvia Lang, Kirstin Atrott, Marianne R Spalinger, Michael Scharl, Kacper A Wojtal, Anne Fischbeck-Terhalle, Isabelle Frey-Wagner, Martin Hausmann, Thomas Kraemer, and Gerhard Rogler. Titanium dioxide nanoparticles exacerbate DSS-induced colitis: role of the NLRP3 inflammasome. *Gut*, 66(7):1216–1224, 2016. doi: 10.1136/gutjnl-2015-310297.

[89] Héloïse Proquin, Carolina Rodríguez-Ibarra, Carolyn G. J. Moonen, Ismael M. Urrutia Ortega, Jacob J. Briedé, Theo M. de Kok, Henk van Loveren, and Yolanda I. Chirino. Titanium dioxide food additive (E171) induces ROS formation and genotoxicity: contribution of micro and nano-sized fractions. *Mutagenesis*, 32(1):139–149, 2016. doi: 10.1093/mutage/gew051.

[90] Sarah Bettini, Elisa Boutet-Robinet, Christel Cartier, Christine Coméra, Eric Gaultier, Jacques Dupuy, Nathalie Naud, Sylviane Taché, Patrick Grysan, Solenn Reguer, Nathalie Thieriet, Matthieu Réfrégiers, Dominique Thiaudière, Jean-Pierre Cravedi, Marie Carrière, Jean-Nicolas Audinot,

Fabrice H. Pierre, Laurence Guzylack-Piriou, and Eric Houdeau. Food-grade TiO_2 impairs intestinal and systemic immune homeostasis, initiates preneoplastic lesions and promotes aberrant crypt development in the rat colon. *Scientific Reports*, 7(1):40373, 2017. doi: 10.1038/srep40373.

[91] Zhongyuan Guo, Nicole J. Martucci, Fabiola Moreno-Olivas, Elad Tako, and Gretchen J. Mahler. Titanium dioxide nanoparticle ingestion alters nutrient absorption in an in vitro model of the small intestine. *NanoImpact*, 5:70–82, 2017. doi: 10.1016/j.impact.2017.01.002.

[92] Gabriela Pinget, Jian Tan, Bartlomiej Janac, Nadeem O. Kaakoush, Alexandra Sophie Angelatos, John O'Sullivan, Yen Chin Koay, Frederic Sierro, Joel Davis, Shiva Kamini Divakarla, Dipesh Khanal, Robert J. Moore, Dragana Stanley, Wojciech Chrzanowski, and Laurence Macia. Impact of the Food Additive Titanium Dioxide (E171) on Gut Microbiota-Host Interaction. *Frontiers in Nutrition*, 6:57, 2019. doi: 10.3389/fnut.2019.00057.

[93] Robert Baan, Kurt Straif, Yann Grosse, Béatrice Secretan, Fatiha El Ghissassi, and Vincent Cogliano. Carcinogenicity of carbon black, titanium dioxide, and talc. *The Lancet Oncology*, 7(4):295–296, 2006. doi: 10.1016/s1470-2045(06)70651-9.

[94] European Chemicals Agency ECHA. Titanium dioxide proposed to be classified as suspected of causing cancer when inhaled. https://www.echa.europa.eu/-/titanium-dioxide-proposed-to-be-classified-as-suspected-of-causing-cancer-when-inhaled, 2017. Accessed: 2020-03-26.

[95] Official Journal of the European Union. Commission Delegated Regulation (EU) 2020/217 of 4 October 2019. http://data.europa.eu/eli/reg_del/2020/217/oj, 2020. Accessed: 2020-03-26.

[96] Official Journal of the European Union. Corrigendum to Commission Delegated Regulation (EU) 2020/217 of 4 October 2019. https://eur-lex.europa.eu/eli/reg_del/2020/217/corrigendum/2020-02-25/oj, 2020. Accessed: 2020-03-26.

[97] A. Guillard, E. Gaultier, C. Cartier, L. Devoille, J. Noireaux, L. Chevalier, M. Morin, F. Grandin, M. Z. Lacroix, C. Coméra, A. Cazanave, A. de Place, V. Gayrard, V. Bach, K. Chardon, N. Bekhti, K. Adel-Patient, C. Vayssière, P. Fisicaro, N. Feltin, F. de la Farge, N. Picard-Hagen, B. Lamas, and E. Houdeau. Basal Ti level in the human placenta and meconium and

evidence of a materno-foetal transfer of food-grade TiO$_2$ nanoparticles in an ex vivo placental perfusion model. *Particle and Fibre Toxicology*, 17(1): 51, 2020. doi: 10.1186/s12989-020-00381-z.

[98] EFSA Panel on Food Additives and Flavourings (FAF). Safety assessment of titanium dioxide (E171) as a food additive. *EFSA Journal*, 19(5):6585, 2021. doi: https://doi.org/10.2903/j.efsa.2021.6585.

[99] J. A. Seiner and H. L. Gerhart. Light scattering from microvoids. applications to polymer coatings. *Industrial & Engineering Chemistry Product Research and Development*, 12(2):98–109, 1973. doi: 10.1021/i360046a002.

[100] D. M. D. Stewart. Opacifiers for latex paints. In *Surface Coatings*, pages 343–355. Springer Netherlands, Dordrecht, 1993. doi: 10.1007/978-94-011-1220-8_23.

[101] Alexander Kowalski, Martin Vogel, and Robert M Blankenship. Sequential heteropolymer dispersion and a particulate material obtainable therefrom, useful in coating compositions as a thickening and/or opacifying agent - US Patent 4,427,836, 1984.

[102] Alexander Kowalski and Martin Vogel. Sequential heteropolymer dispersion and a particulate material obtainable therefrom, useful in coating compositions as an opacifying agent - US Patent 4,469,825, 1984.

[103] Dow. Product information: Ropaque™ hollow-sphere polymeric pigments. https://www.dow.com/en-us/product-technology/pt-additives-modifiers/pg-additives-hollow-sphere-pigments.html, . Accessed: 2021-03-21.

[104] Dow. Technical data sheet: Ropaque™ ULTRA E SLF Opaque Polymer. https://www.dow.com/en-us/pdp.ropaque-ultra-e-slf-opaque-polymer.392452z.html, . Accessed: 2021-03-24.

[105] Charles J McDonald and Michael J Devon. Hollow latex particles: synthesis and applications. *Advances in Colloid and Interface Science*, 99(3): 181–213, 2002. doi: 10.1016/s0001-8686(02)00034-9.

[106] Liwen Zhu, Duc Nguyen, Tim Davey, Matthew Baker, Chris Such, Brian S. Hawkett, and Chiara Neto. Mechanical properties of ropaque hollow nanoparticles. *Polymer*, 131:10–16, 2017. doi: 10.1016/j.polymer.2017.10.030.

[107] R. Lambourne. *Paint and Surface Coatings.* Woodhead Publishing Series in Metals and Surface Engineering. Woodhead Publishing, Cambridge England, second edition edition, 1999. ISBN 978-1-85573-348-0.

[108] Duc Nguyen, Chris Such, and Brian Hawkett. Polymer-TiO$_2$ composite nanorattles via RAFT-mediated emulsion polymerization. *Journal of Polymer Science Part A: Polymer Chemistry*, 50(2):346–352, 2011. doi: 10.1002/pola.25038.

[109] Microbeads AS. Product information: Spheromers®. http://micro-beads.com/Applications.aspx. Accessed: 2021-04-23.

[110] Kyoungmin Min, Meredith Silberstein, and N. R. Aluru. Crosslinking PMMA: Molecular dynamics investigation of the shear response. *Journal of Polymer Science Part B: Polymer Physics*, 52(6):444–449, 2013. doi: 10.1002/polb.23437.

[111] Mahmoud A Hussein. Role of cross-linking process on the performance of PMMA. *International Journal of Biosensors & Bioelectronics*, 3(3):279–284, 2017. doi: 10.15406/ijbsbe.2017.03.00065.

[112] Eric Jungermann and Norman OV Sonntag, editors. *Glycerine: a key cosmetic ingredient*, volume 11. CRC Press, Boca Raton, 1991. ISBN 9780203753071. doi: 10.1201/9780203753071.

[113] T Pun. Entropic thresholding, a new approach. *Computer Graphics and Image Processing*, 16(3):210–239, 1981. doi: 10.1016/0146-664x(81)90038-1.

[114] J.N. Kapur, P.K. Sahoo, and A.K.C. Wong. A new method for gray-level picture thresholding using the entropy of the histogram. *Computer Vision, Graphics, and Image Processing*, 29(3):273–285, 1985. doi: 10.1016/0734-189x(85)90125-2.

[115] William D. Ross. Theoretical Light-Scattering Power of TiO$_2$ Microviods. *Industrial & Engineering Chemistry Product Research and Development*, 13 (1):45–49, 1974. doi: 10.1021/i360049a010.

[116] Jong Myung Park and Seoung Min Hong. Light scattering of model microvoid films. *Journal of Industrial and Engineering Chemistry*, 7(1):23–29, 2001.

[117] J.-C. Auger and D. McLoughlin. Theoretical study and experimental analysis of the scattering efficiency of hollow polymer particles in the dependent light scattering regime. *Journal of Coatings Technology and Research*, 12(4): 693–709, 2015. doi: 10.1007/s11998-015-9677-0.

[118] Julia Syurik, Ruth Schwaiger, Prerna Sudera, Stephan Weyand, Siegbert Johnsen, Gabriele Wiegand, and Hendrik Hölscher. Bio-inspired micro-to-nanoporous polymers with tunable stiffness. *Beilstein Journal of Nanotechnology*, 8:906–914, 2017. doi: 10.3762/bjnano.8.92.

[119] Suset Barroso-Solares, Daniel Cuadra-Rodriguez, Maria Luz Rodriguez-Mendez, Miguel Angel Rodriguez-Perez, and Javier Pinto. A new generation of hollow polymeric microfibers produced by gas dissolution foaming. *Journal of Materials Chemistry B*, 8(38):8820–8829, 2020. doi: 10.1039/d0tb01560a.

[120] D. Cuadra-Rodríguez, S. Barroso-Solares, M.A. Rodríguez-Pérez, and J. Pinto. Production of cellular polymers without solid outer skins by gas dissolution foaming: A long-sought step towards new applications. *Materials & Design*, 217:110648, 2022. doi: 10.1016/j.matdes.2022.110648.

[121] Vincenzo Contaldi, Luigi Imperato, Silvia Orsi, Ernesto Di Maio, Paolo Antonio Netti, and Salvatore Iannace. Morphology modulation of gas-foamed, micrometric, hollow polystyrene particles. *Journal of Applied Polymer Science*, 133(48):44236, 2016. doi: 10.1002/app.44236.

[122] Vincenzo Contaldi, Maria Giovanna Pastore Carbone, Ernesto Di Maio, Anastasios C. Manikas, and Paolo Antonio Netti. Easy-to-fill asymmetric polymeric micro-reservoirs. *RSC Advances*, 6(68):64140–64146, 2016. doi: 10.1039/c6ra04812a.

[123] J. Rault, R. Gref, Z.H. Ping, Q.T. Nguyen, and J. Néel. Glass transition temperature regulation effect in a poly(vinyl alcohol) water system. *Polymer*, 36(8):1655–1661, 1995. doi: 10.1016/0032-3861(95)99011-i.

[124] Frank Fischer and Stephan Bauer. Polyvinylpyrrolidon. Ein Tausendsassa in der Chemie. *Chemie in unserer Zeit*, 43(6):376–383, 2009. doi: 10.1002/ciuz.200900492.

[125] Swapan Kumar Ghosh, editor. *Functional Coatings*. Wiley-VCH, Weinheim, 2006. ISBN 9783527312962. doi: 10.1002/3527608478.

[126] G. Decher, J.D. Hong, and J. Schmitt. Buildup of ultrathin multilayer films by a self-assembly process: III. consecutively alternating adsorption of anionic and cationic polyelectrolytes on charged surfaces. *Thin Solid Films*, 210-211:831–835, 1992. doi: 10.1016/0040-6090(92)90417-a.

[127] International Energy Agency IEA. The future of cooling. https://iea.blob.core.windows.net/assets/0bb45525-277f-4c9c-8d0c-9c0cb5e7d525/The_Future_of_Cooling.pdf, 2018. Accessed: 2022-01-31.

[128] Mat Santamouris. Heat island research in europe: The state of the art. *Advances in Building Energy Research*, 1(1):123–150, 2007. doi: 10.1080/17512549.2007.9687272.

[129] Chua Kian Jon, Md Raisul Islam, and Muhammad Wakil Shahzad. *Advances in Air Conditioning Technologies*. Springer Singapore, Singapore, 2021. ISBN 9811584796. doi: 10.1007/978-981-15-8477-0.

[130] International Energy Agency IEA. Global air conditioner stock, 1990-2050. https://www.iea.org/data-and-statistics/charts/global-air-conditioner-stock-1990-2050, 2022. Licence: CC BY 4.0.

[131] G. J. M. Velders, D. W. Fahey, J. S. Daniel, M. McFarland, and S. O. Andersen. The large contribution of projected HFC emissions to future climate forcing. *Proceedings of the National Academy of Sciences*, 106(27):10949–10954, 2009. doi: 10.1073/pnas.0902817106.

[132] Eric A. Heath. Amendment to the Montreal Protocol on Substances that Deplete the Ozone Layer (Kigali Amendment). *International Legal Materials*, 56(1):193–205, 2017. doi: 10.1017/ilm.2016.2.

[133] Sergio Bobbo, Laura Fedele, Marco Curcio, Anna Bet, Michele De Carli, Giuseppe Emmi, Fabio Poletto, Andrea Tarabotti, Dimitris Mendrinos, Giulia Mezzasalma, and Adriana Bernardi. Energetic and Exergetic Analysis of Low Global Warming Potential Refrigerants as Substitutes for R410A in Ground Source Heat Pumps. *Energies*, 12(18):3538, 2019. doi: 10.3390/en12183538.

[134] Nadja Kabisch, Horst Korn, Jutta Stadler, and Aletta Bonn, editors. *Nature-Based Solutions to Climate Change Adaptation in Urban Areas*. Springer International Publishing, Cham, 2017. ISBN 978-3-319-56091-5. doi: 10.1007/978-3-319-56091-5.

[135] C Cartalis, A Synodinou, M Proedrou, A Tsangrassoulis, and M Santamouris. Modifications in energy demand in urban areas as a result of climate changes: an assessment for the southeast mediterranean region. *Energy Conversion and Management*, 42(14):1647–1656, 2001. doi: 10.1016/s0196-8904(00)00156-4.

[136] Nicole Pfoser, editor. *Gebäude Begrünung Energie : Potenziale und Wechselwirkungen.* FLL-Schriftenreihe Forschungsvorhaben ; FV 2014/01. Forschungsgesellschaft Landschaftsentwicklung Landschaftsbau, Bonn, 2014. ISBN 9783940122469.

[137] Maria Soledad Penaranda Moren and Azra Korjenic. Untersuchungen zum ganzjährigen Wärmeschutz an Varianten eines kombinierten Dachaufbaus mit Photovoltaik und Begrünung. *Bauphysik*, 40(3):131–142, 2018. doi: 10.1002/bapi.201810016.

[138] Thomas A. M. Pugh, A. Robert MacKenzie, J. Duncan Whyatt, and C. Nicholas Hewitt. Effectiveness of green infrastructure for improvement of air quality in urban street canyons. *Environmental Science & Technology*, 46(14):7692–7699, 2012. doi: 10.1021/es300826w.

[139] Paul Berdahl. Retrospective on the resource for radiative cooling. *Journal of Photonics for Energy*, 11(04), 2021. doi: 10.1117/1.jpe.11.042106.

[140] Wei Li and Shanhui Fan. Radiative cooling: Harvesting the coldness of the universe. *Optics and Photonics News*, 30(11):32, 2019. doi: 10.1364/opn.30.11.000032.

[141] Mehdi Zeyghami, D. Yogi Goswami, and Elias Stefanakos. A review of clear sky radiative cooling developments and applications in renewable power systems and passive building cooling. *Solar Energy Materials and Solar Cells*, 178:115–128, 2018. doi: 10.1016/j.solmat.2018.01.015.

[142] The American Society for Testing and Materials (ASTM). ASTM G-173-03 Reference Spectra. https://www.nrel.gov/grid/solar-resource/spectra-am1.5.html. Accessed: 2022-12-21.

[143] SD Lord. Nasa technical memorandum 103957, 1992.

[144] Gemini-Observatory. The infrared spectra of the atmospheric transmission. https://www.gemini.edu/observing/telescopes-and-sites/sites. Accessed: 2022-12-21.

[145] M. Mahdavinejad and Kavan Javanrudi. Assessment of ancient fridges: A sustainable method to storage ice in hot-arid climates. *Asian Culture and History*, 4(2), 2012. doi: 10.5539/ach.v4n2p133.

[146] Eden Rephaeli, Aaswath Raman, and Shanhui Fan. Ultrabroadband photonic structures to achieve high-performance daytime radiative cooling. *Nano Letters*, 13(4):1457–1461, 2013. doi: 10.1021/nl4004283.

[147] Aaswath P. Raman, Marc Abou Anoma, Linxiao Zhu, Eden Rephaeli, and Shanhui Fan. Passive radiative cooling below ambient air temperature under direct sunlight. *Nature*, 515(7528):540–544, 2014. doi: 10.1038/nature13883.

[148] Bin Zhao, Mingke Hu, Xianze Ao, Nuo Chen, and Gang Pei. Radiative cooling: A review of fundamentals, materials, applications, and prospects. *Applied Energy*, 236:489–513, 2019. doi: 10.1016/j.apenergy.2018.12.018.

[149] Yao Zhai, Yaoguang Ma, Sabrina N. David, Dongliang Zhao, Runnan Lou, Gang Tan, Ronggui Yang, and Xiaobo Yin. Scalable-manufactured randomized glass-polymer hybrid metamaterial for daytime radiative cooling. *Science*, 355(6329):1062–1066, 2017. doi: 10.1126/science.aai7899.

[150] Tian Li, Yao Zhai, Shuaiming He, Wentao Gan, Zhiyuan Wei, Mohammad Heidarinejad, Daniel Dalgo, Ruiyu Mi, Xinpeng Zhao, Jianwei Song, Jiaqi Dai, Chaoji Chen, Ablimit Aili, Azhar Vellore, Ashlie Martini, Ronggui Yang, Jelena Srebric, Xiaobo Yin, and Liangbing Hu. A radiative cooling structural material. *Science*, 364(6442):760–763, 2019. doi: 10.1126/science.aau9101.

[151] A. R. Gentle and G. B. Smith. Radiative heat pumping from the earth using surface phonon resonant nanoparticles. *Nano Letters*, 10(2):373–379, 2010. doi: 10.1021/nl903271d.

[152] Joseph Peoples, Xiangyu Li, Yaobing Lv, Jun Qiu, Zhifeng Huang, and Xiulin Ruan. A strategy of hierarchical particle sizes in nanoparticle composite for enhancing solar reflection. *International Journal of Heat and Mass Transfer*, 131:487–494, 2019. doi: 10.1016/j.ijheatmasstransfer.2018.11.059.

[153] Hua Bao, Chen Yan, Boxiang Wang, Xing Fang, C.Y. Zhao, and Xiulin Ruan. Double-layer nanoparticle-based coatings for efficient terrestrial radiative cooling. *Solar Energy Materials and Solar Cells*, 168:78–84, 2017. doi: 10.1016/j.solmat.2017.04.020.

[154] Sarun Atiganyanun, John B. Plumley, Seok Jun Han, Kevin Hsu, Jacob Cytrynbaum, Thomas L. Peng, Sang M. Han, and Sang Eon Han. Effective radiative cooling by paint-format microsphere-based photonic random media. *ACS Photonics*, 5(4):1181–1187, 2018. doi: 10.1021/acsphotonics.7b01492.

[155] Zhifeng Huang and Xiulin Ruan. Nanoparticle embedded double-layer coating for daytime radiative cooling. *International Journal of Heat and*

Mass Transfer, 104:890–896, 2017. doi: 10.1016/j.ijheatmasstransfer.2016.08.009.

[156] A. Aili, Z.Y. Wei, Y.Z. Chen, D.L. Zhao, R.G. Yang, and X.B. Yin. Selection of polymers with functional groups for daytime radiative cooling. *Materials Today Physics*, 10:100127, 2019. doi: 10.1016/j.mtphys.2019.100127.

[157] 3M. Product Information: 3M Passive Radiative Cooling Film. https://www.3m.com/3M/en_US/energy-conservation-us/applications/passive-radiative-cooling/. Accessed: 2022-06-28.

[158] Xia Huang, Na Li, Junfeng Wang, Defang Liu, Jing Xu, Zhijie Zhang, and Mingfeng Zhong. Single nanoporous $MgHPO_4 \cdot 1.2H_2O$ for daytime radiative cooling. *ACS Applied Materials & Interfaces*, 12(2):2252–2258, 2019. doi: 10.1021/acsami.9b14615.

[159] Dasol Lee, Myeongcheol Go, Soomin Son, Minkyung Kim, Trevon Badloe, Heon Lee, Jin Kon Kim, and Junsuk Rho. Sub-ambient daytime radiative cooling by silica-coated porous anodic aluminum oxide. *Nano Energy*, 79:105426, 2021. doi: 10.1016/j.nanoen.2020.105426.

[160] Hongmei Zhong, Peng Zhang, Yanan Li, Xiaochen Yang, Yang Zhao, and Zuankai Wang. Highly solar-reflective structures for daytime radiative cooling under high humidity. *ACS Applied Materials & Interfaces*, 12(46):51409–51417, 2020. doi: 10.1021/acsami.0c14075.

[161] Bo Xiang, Rong Zhang, Yanlong Luo, Sheng Zhang, Lei Xu, Huihua Min, Shaochun Tang, and Xiangkang Meng. 3D porous polymer film with designed pore architecture and auto-deposited SiO_2 for highly efficient passive radiative cooling. *Nano Energy*, 81:105600, 2021. doi: 10.1016/j.nanoen.2020.105600.

[162] Xin Wang, Xianghui Liu, Zhenyang Li, Haiwen Zhang, Zhiwei Yang, Han Zhou, and Tongxiang Fan. Scalable flexible hybrid membranes with photonic structures for daytime radiative cooling. *Advanced Functional Materials*, 30(5):1907562, 2019. doi: 10.1002/adfm.201907562.

[163] Wilhelm Nultsch. *Allgemeine Botanik*. Georg Thieme Verlag, Stuttgart, 11 edition, 2001. ISBN 978-3-13-383311-0.

[164] Monika Österberg, Mika H. Sipponen, Bruno D. Mattos, and Orlando J. Rojas. Spherical lignin particles: a review on their sustainability and applications. *Green Chemistry*, 22(9):2712–2733, 2020. doi: 10.1039/d0gc00096e.

[165] Xiao Nie, Youngjae Yoo, Hasitha Hewakuruppu, Jonathan Sullivan, Anirudh Krishna, and Jaeho Lee. Cool white polymer coatings based on glass bubbles for buildings. *Scientific Reports*, 10(1), 2020. doi: 10.1038/s41598-020-63027-2.

[166] Huaixia Zhao, Qiangqiang Sun, Ji Zhou, Xu Deng, and Jiaxi Cui. Switchable cavitation in silicone coatings for energy-saving cooling and heating. *Advanced Materials*, 32(29):2000870, 2020. doi: 10.1002/adma.202000870.

[167] Duo Li, Xin Liu, Wei Li, Zhenhui Lin, Bin Zhu, Zizhong Li, Jinlei Li, Bo Li, Shanhui Fan, Jiwei Xie, and Jia Zhu. Scalable and hierarchically designed polymer film as a selective thermal emitter for high-performance all-day radiative cooling. *Nature Nanotechnology*, 16(2):153–158, 2020. doi: 10.1038/s41565-020-00800-4.

[168] Röhm GmbH. PLEXIGLAS® und EUROPLEX® Folien. https://www.plexiglas.de/de/produkte/plexiglas/plexiglas-europlex-folien. Accessed: 2022-07-06.

[169] C Joram. Transmission curves of plexiglass (PMMA) and optical grease. Technical Report PH-EP-Tech-Note-2009-003, CERN, Geneva, 2009. URL https://cds.cern.ch/record/1214725. Accessed: 2023-10-25.

[170] A.D. Alobaidani, D. Furniss, M.S. Johnson, A. Endruweit, and A.B Seddon. Optical transmission of PMMA optical fibres exposed to high intensity UVA and visible blue light. *Optics and Lasers in Engineering*, 48(5):575–582, 2010. doi: 10.1016/j.optlaseng.2009.11.012.

[171] Azahara Martínez-García, Isabel Oller, Martin Vincent, Viviana Rubiolo, Jacent K. Asiimwe, Charles Muyanja, Kevin G. McGuigan, Pilar Fernández-Ibáñez, and María Inmaculada Polo-López. Meeting daily drinking water needs for communities in sub-saharan africa using solar reactors for harvested rainwater. *Chemical Engineering Journal*, 428:132494, 2022. doi: 10.1016/j.cej.2021.132494.

[172] Torbjörn M.J. Nilsson, Gunnar A. Niklasson, and Claes G. Granqvist. A solar reflecting material for radiative cooling applications: ZnS pigmented polyethylene. *Solar Energy Materials and Solar Cells*, 28(2):175–193, 1992. doi: 10.1016/0927-0248(92)90010-m.

[173] Eckhard Limpert, Werner A. Stahel, and Markus Abbt. Log-normal distributions across the sciences: Keys and clues. *BioScience*, 51(5):341, 2001. doi: 10.1641/0006-3568(2001)051[0341:lndats]2.0.co;2.

[174] Eric W. Weisstein. Log Normal Distribution. From MathWorld - A Wolfram Web Resource. https://mathworld.wolfram.com/LogNormalDistribution.html. Accessed: 2023-01-11.

[175] Xiang Cheng, Weimin Yang, Chengyou Lin, Yumei Ding, and Zhiwei Jiao. Design of broadband near-infrared reflector using polymer multilayer heterostructure with low-refractive-index contrast. *Applied Physics A*, 123 (10), 2017. doi: 10.1007/s00339-017-1261-2.

[176] Fateme Zeighami and Mohammad Amani Tehran. Developing optically efficient nanofiber coatings inspired by cyphochilus white beetle. *Journal of Industrial Textiles*, 46(2):495–509, 2015. doi: 10.1177/1528083715589751.

[177] S.P. Venkateshan. *Heat Transfer*. Springer International Publishing, Cham, 2021. ISBN 978-981-15-3988-6. doi: 10.1007/978-3-030-58338-5.

[178] J. A. Mäder, J. Staehelin, T. Peter, D. Brunner, H. E. Rieder, and W. A. Stahel. Evidence for the effectiveness of the Montreal Protocol to protect the ozone layer. *Atmospheric Chemistry and Physics*, 10(24):12161–12171, 2010. doi: 10.5194/acp-10-12161-2010.

[179] Rishav Goyal, Matthew H England, Alex Sen Gupta, and Martin Jucker. Reduction in surface climate change achieved by the 1987 Montreal Protocol. *Environmental Research Letters*, 14(12):124041, 2019. doi: 10.1088/1748-9326/ab4874.

[180] Linxiao Zhu, Aaswath Raman, Ken Xingze Wang, Marc Abou Anoma, and Shanhui Fan. Radiative cooling of solar cells. *Optica*, 1(1):32, 2014. doi: 10.1364/optica.1.000032.

[181] Linxiao Zhu, Aaswath P. Raman, and Shanhui Fan. Radiative cooling of solar absorbers using a visibly transparent photonic crystal thermal blackbody. *Proceedings of the National Academy of Sciences*, 112(40):12282–12287, 2015. doi: 10.1073/pnas.1509453112.

[182] Jyotirmoy Mandal, Mingxin Jia, Adam Overvig, Yanke Fu, Eric Che, Nanfang Yu, and Yuan Yang. Porous polymers with switchable optical transmittance for optical and thermal regulation. *Joule*, 3(12):3088–3099, 2019. doi: 10.1016/j.joule.2019.09.016.

[183] Hannah Kim and Andrej Lenert. Optical and thermal filtering nanoporous materials for sub-ambient radiative cooling. *Journal of Optics*, 20(8): 084002, 2018. doi: 10.1088/2040-8986/aacaa1.

[184] C. G. Bernhard and William H. Miller. A corneal nipple pattern in insect compound eyes. *Acta Physiologica Scandinavica*, 56(3-4):385–386, 1962. doi: 10.1111/j.1748-1716.1962.tb02515.x.

[185] Alan B. Harker and Jeffrey F. DeNatale. Diamond gradient index moth-eye antireflection surfaces for LWIR windows. In Paul Klocek, editor, *Window and Dome Technologies and Materials III*. SPIE, 1992. doi: 10.1117/12.130803.

[186] Matthias Worgull. *Hot embossing : theory and technology of microreplication*. William Andrew (Elsevier), Oxford, UK, 1. ed. edition, 2009. ISBN 9780815515791.

[187] Yong Wang, Zhimin Liu, Buxing Han, Ying Huang, Jianling Zhang, Donghai Sun, and Jimin Du. Compressed- CO_2 -Assisted Patterning of Polymers. *The Journal of Physical Chemistry B*, 109(25):12376–12379, 2005. doi: 10.1021/jp050954h.

[188] Shun-suke Nozaki and Masahiro Ohshima. A CO_2 assisted nanoimprinting and cold embossing. volume 5, pages 2551–2555. Annual Technical Conference – ANTEC Conference Proceedings, 2006.

[189] Won Mook Choi, Min Young Song, and O Ok Park. Compressed-carbon dioxide (CO_2) assisted nanoimprint lithography using polymeric mold. *Microelectronic Engineering*, 83(10):1957–1960, 2006. doi: 10.1016/j.mee.2006.02.003.

[190] Sen-Yeu Yang, Tzu-Chien Huang, Jyun-Kai Ciou, Bin-Da Chan, and John G Loeser. CO_2-assisted embossing for the fabrication of PMMA components under low temperature and with low pressure. *Journal of Micromechanics and Microengineering*, 18(2):025024, 2008. doi: 10.1088/0960-1317/18/2/025024.

[191] Andrew M. Farmer. The effects of dust on vegetation—a review. *Environmental Pollution*, 79(1):63–75, 1993. doi: 10.1016/0269-7491(93)90179-r.

[192] W. Barthlott and C. Neinhuis. Purity of the sacred lotus, or escape from contamination in biological surfaces. *Planta*, 202(1):1–8, 1997. doi: 10.1007/s004250050096.

[193] Thomas Wagner, Christoph Neinhuis, and Wilhelm Barthlott. Wettability and contaminability of insect wings as a function of their surface sculptures. *Acta Zoologica*, 77(3):213–225, 1996. doi: 10.1111/j.1463-6395.1996.tb01265.x.

[194] Gregory S. Watson, David W. Green, Bronwen W. Cribb, Christopher L. Brown, Christopher R. Meritt, Mark J. Tobin, Jitraporn Vongsvivut, Mingxia Sun, Ai-Ping Liang, and Jolanta A. Watson. Insect analogue to the lotus leaf: A planthopper wing membrane incorporating a low-adhesion, nonwetting, superhydrophobic, bactericidal, and biocompatible surface. *ACS Applied Materials & Interfaces*, 9(28):24381–24392, 2017. doi: 10.1021/acsami.7b08368.

[195] Stuart A. Boden and Darren M. Bagnall. Nanostructured antireflective surfaces arrays. In Bharat Bhushan, editor, *Encyclopedia of Nanotechnology*, pages 1760–1760. Springer Netherlands, Dordrecht, 2012. ISBN 978-90-481-9751-4. doi: 10.1007/978-90-481-9751-4_100562.

[196] X. Gao, X. Yan, X. Yao, L. Xu, K. Zhang, J. Zhang, B. Yang, and L. Jiang. The dry-style antifogging properties of mosquito compound eyes and artificial analogues prepared by soft lithography. *Advanced Materials*, 19(17):2213–2217, 2007. doi: 10.1002/adma.200601946.

[197] Ziqi Sun, Ting Liao, Kesong Liu, Lei Jiang, Jung Ho Kim, and Shi Xue Dou. Fly-eye inspired superhydrophobic anti-fogging inorganic nanostructures. *Small*, 10(15):3001–3006, 2014. doi: 10.1002/smll.201400516.

[198] Junko Morikawa, Meguya Ryu, Gediminas Seniutinas, Armandas Balčytis, Ksenia Maximova, Xuewen Wang, Massimiliano Zamengo, Elena P. Ivanova, and Saulius Juodkazis. Nanostructured antireflective and thermoisolative cicada wings. *Langmuir*, 32(18):4698–4703, 2016. doi: 10.1021/acs.langmuir.6b00621.

[199] Mingxia Sun, Gregory S. Watson, Yongmei Zheng, Jolanta A. Watson, and Aiping Liang. Wetting properties on nanostructured surfaces of cicada wings. *Journal of Experimental Biology*, 212(19):3148–3155, 2009. doi: 10.1242/jeb.033373.

[200] Mingxia Sun, Aiping Liang, Yongmei Zheng, Gregory S Watson, and Jolanta A Watson. A study of the anti-reflection efficiency of natural nano-arrays of varying sizes. *Bioinspiration & Biomimetics*, 6(2):026003, 2011. doi: 10.1088/1748-3182/6/2/026003.

[201] Louis Dellieu, Michaël Sarrazin, Priscilla Simonis, Olivier Deparis, and Jean Pol Vigneron. A two-in-one superhydrophobic and anti-reflective nanodevice in the grey cicada Cicada orni (Hemiptera). *Journal of Applied Physics*, 116(2):024701, 2014. doi: 10.1063/1.4889849.

[202] temicon GmbH. Product information: High Performance AR Molds HT-AR-02. https://www.temicon.com/technologies/nano-and-micro-structures/anti-reflection-structures. Accessed:2023-02-20.

[203] Michael Nosonovsky and Bharat Bhushan. Hierarchical roughness optimization for biomimetic superhydrophobic surfaces. *Ultramicroscopy*, 107 (10-11):969–979, 2007. doi: 10.1016/j.ultramic.2007.04.011.

[204] Robert N. Wenzel. Resistance of solid surfaces to wetting by water. *Industrial & Engineering Chemistry*, 28(8):988–994, 1936. doi: 10.1021/ie50320a024.

[205] Benjamin Fritz, Markus Guttmann, Pere Casas Soler, Aiman Roslizar, Malte Langenhorst, Marc Schneider, Ulrich W. Paetzold, Bryce S. Richards, Ulrich Lemmer, Ruben Huenig, and Guillaume Gomard. Towards mass fabrication of hot embossed plant surface texture replicas as photovoltaic cover layers. In Balaji Panchapakesan, Anne E. Sakdinawat, André-Jean Attias, and Elizabeth A. Dobisz, editors, *Nanoengineering: Fabrication, Properties, Optics, and Devices XV*, volume 10730, page 107300J. International Society for Optics and Photonics, SPIE, 2018. doi: 10.1117/12.2320555.

[206] Ying Ma, Xinyu Cao, Xinjian Feng, Yongmei Ma, and Hong Zou. Fabrication of super-hydrophobic film from PMMA with intrinsic water contact angle below 90°. *Polymer*, 48(26):7455–7460, 2007. doi: 10.1016/j.polymer.2007.10.038.

[207] Xue-Mei Li, David Reinhoudt, and Mercedes Crego-Calama. What do we need for a superhydrophobic surface? A review on the recent progress in the preparation of superhydrophobic surfaces. *Chemical Society Reviews*, 36(8):1350, 2007. doi: 10.1039/b602486f.

[208] Michael Nosonovsky and Bharat Bhushan. Roughness optimization for biomimetic superhydrophobic surfaces. *Microsystem Technologies*, 11(7): 535–549, 2005. doi: 10.1007/s00542-005-0602-9.

[209] Changchun Zhou, Peng Wang, and Wei Li. Fabrication of functionally graded porous polymer via supercritical CO_2 foaming. *Composites Part B: Engineering*, 42(2):318–325, 2011. doi: 10.1016/j.compositesb.2010.11.001.

[210] Mai T. Ngo, James S. Dickmann, John C. Hassler, and Erdogan Kiran. A new experimental system for combinatorial exploration of foaming of polymers in carbon dioxide: The gradient foaming of PMMA. *The Journal of Supercritical Fluids*, 109:1–19, 2016. doi: 10.1016/j.supflu.2015.09.030.

[211] Elena P. Ivanova, Jafar Hasan, Hayden K. Webb, Vi Khanh Truong, Gregory S. Watson, Jolanta A. Watson, Vladimir A. Baulin, Sergey Pogodin, James Y. Wang, Mark J. Tobin, Christian Löbbe, and Russell J. Crawford. Natural Bactericidal Surfaces: Mechanical Rupture of Pseudomonas aeruginosa Cells by Cicada Wings. *Small*, 8(16):2489–2494, 2012. doi: 10.1002/smll.201200528.

[212] Sergey Pogodin, Jafar Hasan, Vladimir A. Baulin, Hayden K. Webb, Vi Khanh Truong, The Hong Phong Nguyen, Veselin Boshkovikj, Christopher J. Fluke, Gregory S. Watson, Jolanta A. Watson, Russell J. Crawford, and Elena P. Ivanova. Biophysical model of bacterial cell interactions with nanopatterned cicada wing surfaces. *Biophysical Journal*, 104(4):835–840, 2013. doi: 10.1016/j.bpj.2012.12.046.

[213] Satoshi Fujita, Daizaburo Ono, Masahiro Ohshima, and Hiroo Iwata. Supercritical CO_2-assisted embossing for studying cell behaviour on microtextured surfaces. *Biomaterials*, 29(34):4494–4500, 2008. doi: 10.1016/j.biomaterials.2008.08.027.

[214] Ester Priante. Micro-nanostructuring of polymer surfaces via foaming with supercritical CO_2. Masterthesis, 2023.

[215] Winnie W. Y. Lau, Yonathan Shiran, Richard M. Bailey, Ed Cook, Martin R. Stuchtey, Julia Koskella, Costas A. Velis, Linda Godfrey, Julien Boucher, Margaret B. Murphy, Richard C. Thompson, Emilia Jankowska, Arturo Castillo Castillo, Toby D. Pilditch, Ben Dixon, Laura Koerselman, Edward Kosior, Enzo Favoino, Jutta Gutberlet, Sarah Baulch, Meera E. Atreya, David Fischer, Kevin K. He, Milan M. Petit, U. Rashid Sumaila, Emily Neil, Mark V. Bernhofen, Keith Lawrence, and James E. Palardy. Evaluating scenarios toward zero plastic pollution. *Science*, 369(6510): 1455–1461, 2020. doi: 10.1126/science.aba9475.

[216] XiaoZhi Lim. Microplastics are everywhere — but are they harmful? *Nature*, 593(7857):22–25, 2021. doi: 10.1038/d41586-021-01143-3.

[217] A. Dick Vethaak and Juliette Legler. Microplastics and human health. *Science*, 371(6530):672–674, 2021. doi: 10.1126/science.abe5041.

[218] Noreen Khalid, Muhammad Aqeel, Ali Noman, Mohamed Hashem, Yasser S. Mostafa, Haifa Abdulaziz S. Alhaithloul, and Suliman M. Alghanem. Linking effects of microplastics to ecological impacts in marine environments. *Chemosphere*, 264:128541, 2021. doi: 10.1016/j.chemosphere.2020.128541.

[219] Heather A. Leslie, Martin J.M. van Velzen, Sicco H. Brandsma, A. Dick Vethaak, Juan J. Garcia-Vallejo, and Marja H. Lamoree. Discovery and quantification of plastic particle pollution in human blood. *Environment International*, 163:107199, 2022. doi: 10.1016/j.envint.2022.107199.

[220] Lauren C. Jenner, Jeanette M. Rotchell, Robert T. Bennett, Michael Cowen, Vasileios Tentzeris, and Laura R. Sadofsky. Detection of microplastics in human lung tissue using μFTIR spectroscopy. *Science of The Total Environment*, 831:154907, 2022. doi: 10.1016/j.scitotenv.2022.154907.

[221] Antonio Ragusa, Alessandro Svelato, Criselda Santacroce, Piera Catalano, Valentina Notarstefano, Oliana Carnevali, Fabrizio Papa, Mauro Ciro Antonio Rongioletti, Federico Baiocco, Simonetta Draghi, Elisabetta D'Amore, Denise Rinaldo, Maria Matta, and Elisabetta Giorgini. Plasticenta: First evidence of microplastics in human placenta. *Environment International*, 146:106274, 2021. doi: 10.1016/j.envint.2020.106274.

[222] European Chemicals Agency (ECHA). Registry of restriction intentions until outcome. https://echa.europa.eu/registry-of-restriction-intentions/-/dislist/details/0b0236e18244cd73, 2019. Accessed:2023-03-06.

[223] European Food Safety Authority (EFSA). EFSA Scientific Colloquium 25 – A coordinated approach to assess the human health risks of micro- and nanoplastics in food. *EFSA Supporting Publications*, 18(8), 2021. doi: 10.2903/sp.efsa.2021.EN-6815.

[224] Plastic Soup Foundation. Official campaign website. https://www.beatthemicrobead.org/partners/. Accessed: 2023-03-15.

[225] Rethink Plastic. Official website. https://rethinkplasticalliance.eu/. Accessed: 2023-03-15.

[226] Carlo Marrazzo, Ernesto Di Maio, and Salvatore Iannace. Foaming of synthetic and natural biodegradable polymers. *Journal of Cellular Plastics*, 43 (2):123–133, 2007. doi: 10.1177/0021955x06073214.

[227] Sulamith C. Frerich. Biopolymer foaming with supercritical CO_2 - Thermodynamics, foaming behaviour and mechanical characteristics. *The Journal of Supercritical Fluids*, 96:349–358, 2015. doi: 10.1016/j.supflu.2014.09.043.

[228] Leon J. M. Jacobs, Stan A. M. Hurkens, Maartje F. Kemmere, and Jos T. F. Keurentjes. Porous cellulose acetate butyrate foams with a tunable bimodality in foam morphology produced with supercritical carbon dioxide. *Macromolecular Materials and Engineering*, 293(4):298–302, 2008. doi: 10.1002/mame.200700353.

[229] E. Reverchon and S. Cardea. Production of controlled polymeric foams by supercritical CO_2. *The Journal of Supercritical Fluids*, 40(1):144–152, 2007. doi: 10.1016/j.supflu.2006.04.013.

[230] A. Sakka, M. Santamouris, I. Livada, F. Nicol, and M. Wilson. On the thermal performance of low income housing during heat waves. *Energy and Buildings*, 49:69–77, 2012. doi: 10.1016/j.enbuild.2012.01.023.

[231] Weibin Wu, Shudong Yu, Paul Schreiber, Antje Dollmann, Christian Lutz, Guillaume Gomard, Christian Greiner, and Hendrik Hölscher. Variation of the frictional anisotropy on ventral scales of snakes caused by nanoscale steps. *Bioinspiration & Biomimetics*, 15(5):056014, 2020. doi: 10.1088/1748-3190/ab9e51.

[232] Weibin Wu, Markus Guttmann, Marc Schneider, Richard Thelen, Matthias Worgull, Guillaume Gomard, and Hendrik Hölscher. Snake-inspired, nano-stepped surface with tunable frictional anisotropy made from a shape-memory polymer for unidirectional transport of microparticles. *Advanced Functional Materials*, 31(19):2009611, 2021. doi: 10.1002/adfm. 202009611.

[233] S.Y. Jeong, C.Y. Tso, Y.M. Wong, C.Y.H. Chao, and B. Huang. Daytime passive radiative cooling by ultra emissive bio-inspired polymeric surface. *Solar Energy Materials and Solar Cells*, 206:110296, 2020. doi: 10.1016/j.solmat.2019.110296.